

Copyright
by
Zhengyan Li
2014

The Dissertation Committee for Zhengyan Li
certifies that this is the approved version of the following dissertation:

**Single-Shot Visualization of Evolving, Light-Speed
Refractive Index Structures**

Committee:

Michael C. Downer, Supervisor

Michael Becker

Manfred Fink

Xiaoqin (Elaine) Li

Gennady Shvets

**Single-Shot Visualization of Evolving, Light-Speed
Refractive Index Structures**

by

Zhengyan Li, B.S.

DISSERTATION

Presented to the Faculty of the Graduate School of
The University of Texas at Austin
in Partial Fulfillment
of the Requirements
for the Degree of

DOCTOR OF PHILOSOPHY

THE UNIVERSITY OF TEXAS AT AUSTIN

May 2014

Dedicated to my parents, Shuhua Ni and Shumin Li,
and my wife, Ziwei Liu.

Acknowledgments

First and foremost, I am grateful to my PhD supervisor, Dr. Michael Downer, for his everlasting instruction and support for my graduate work. I have learned so much from him, not only the insight of physics and experimental skills, but also the way of working with others and professions in the scientific community. As it said: *When a superior man knows the causes which make instruction successful, and those which make it of no effect, he can become a teacher of others. Thus in his teaching, he leads and does not drag; he strengthens and does not discourage; he opens the way but does not conduct to the end (without the learner's own efforts). Leading and not dragging produces harmony. Strengthening and not discouraging makes attainment easy. Opening the way and not conducting to the end makes (the learner) thoughtful. He who produces such harmony, easy attainment, and thoughtfulness may be pronounced a skilful teacher* (from *Classic of Rites*, a Chinese book written in the period of 475 BC-221 BC).

I sincerely thank all my friends and colleagues in the group, who provide so much help on my research and friendship to get me through these busy but shiny days. They are Dr. Xiaoming Wang, Dr. Rafal Zgadzaaj, Dr. Xiaohui Gao, Dr. Junwei Wei, Dr. Watson Henderson, Hai-En Tsai, Dr. Chih-Hao Pai, JC Sanders, and all others. Especially, I appreciate Dr. Xiaoming Wang

for support in these years, from teaching me to mount the first mirror when I entered the group, to working with me on the most recent experiments.

I also thank all collaborators in my graduate research for their support and insightful discussions. They are Dr. Gennady Shvets and theorists in his group, together with Dr. Todd Ditmire and the Petawatt Laser scientists.

Finally, I appreciate financial support from the Memorial Glen Focht Fellowship and the William H. Hildebrand Graduate Fellowship.

Single-Shot Visualization of Evolving, Light-Speed Refractive Index Structures

Publication No. _____

Zhengyan Li, Ph.D.

The University of Texas at Austin, 2014

Supervisor: Michael C. Downer

An intense laser or charged particle pulse propagating through matter excites light-speed refractive index structures in its wake via Kerr effect, ionization, or displacement of electrons from background ions. Examples include plasma wakes used to accelerate charged particles and self-guided filaments used for atmospheric analysis and micromachining. Such applications constrain the shape, size and evolution of the index structure, yet often these are known in detail only through intensive computer simulations based on estimated initial conditions. Here we develop and demonstrate three methods for visualizing evolving light-speed structures directly in the laboratory in a single shot : (1) frequency-domain streak camera, (2) frequency-domain tomography, and (3) multi-object-plane phase-contrast imaging. All three methods are based on analyzing phase perturbations that an evolving object imprints on one or more probe laser pulses that cross its path obliquely. The methods are tailored to

different propagation lengths, material densities, and dimensionality of imaging. Using these techniques, evolving laser-driven filaments in glass and air and plasma wakes in helium gas driven by laser pulses up to petawatt peak power are visualized in one shot, revealing underlying nonlinear laser-plasma interaction physics that is compared in detail to computer simulations.

Table of Contents

Acknowledgments	v
Abstract	vii
List of Tables	xii
List of Figures	xiii
Chapter 1. Introduction	1
1.1 Nonlinear laser pulse propagation in transparent dielectrics and gases	2
1.2 Laser-plasma electron acceleration	7
1.3 Ultrafast refractive index structures in laser-matter interactions	12
Chapter 2. Prior optical techniques for visualizing light-speed index structures	14
2.1 Frequency–Domain Interferometry	15
2.2 Frequency–Domain Holography	19
2.3 Transverse probing techniques	24
Chapter 3. Frequency–Domain Streak Camera	27
3.1 The oblique-angle pump-probe geometry	28
3.1.1 Frequency–domain streak cameras (FDSC): a time sequence of the index structure’s projections	29
3.1.2 Lab probe angle and effective projection angle	32
3.1.3 z -resolution of frequency–domain streak cameras	34
3.2 Example: FDSC of nonlinear refractive index during megawatt laser propagation in glass	35

Chapter 4. Single-shot visualization of evolving laser wakefields by frequency domain streak camera	42
4.1 Experimental setup and results	44
4.1.1 Terawatt-laser-driven wakefield accelerator	44
4.1.2 The probe pulse for frequency-domain streak camera . .	46
4.2 Analysis of plasma “bubble” induced phase streaks	50
4.2.1 Plasma wakefield “bubble” evolution history under dif-	
ferent density	52
4.2.2 Evolution z -resolution and longitudinal t -resolution . . .	55
4.3 Simulations of laser wakefield excitation and electron acceleration	57
Chapter 5. Frequency–Domain Tomography	63
5.1 Theory of Frequency–Domain Tomography	64
5.1.1 Tomography for light-speed objects	66
5.1.2 Filtered back-projection (FBP) reconstruction	69
5.1.3 Algebraic reconstruction technique (ART)	69
5.1.4 FDT reconstruction quality	73
5.2 Phantom simulations	73
5.3 Experimental FDT setup	77
5.4 Single-shot tomographic movies	83
5.4.1 Laser pulse self-focusing and plasma ionization	83
5.4.2 Comparison of FDT reconstruction with NLSE simulations	88
5.4.3 High-order nonlinear refractive index and electron-hole	
plasma ionization in laser–glass interactions	93
Chapter 6. Multi-object-plane imaging over long interaction dis-	96
tance	
6.1 Probe diffraction and the Rytov approximation	97
6.2 Multi-object-plane imaging (MOPI)	98
6.2.1 Experimental setup	99
6.2.2 Phase retrieval from multi-object-plane images	102
6.3 Nonlinear phase contrast imaging and schlieren for high sensi-	
tivity and robustness	107
6.4 Multi-object-plane phase-contrast imaging of laser filaments in	
air	110

6.4.1	Multi-object-plane imaging resolution	114
6.5	Tilted probe pulse front for pump–probe walk-off compensation	115
Chapter 7.	Petawatt laser driven wakefield acceleration and its optical diagnosis	119
7.1	Petawatt laser driven plasma accelerators for electron and x-ray generation	120
7.1.1	Generation and measurements of 2 GeV electrons	121
7.1.2	Betatron X-ray generation	124
7.2	Multi-object-plane imaging of petawatt-laser-driven plasma wakes	125
7.2.1	Relativistic self-focusing and merging of laser hot-spots .	126
7.2.2	Preliminary multi-object-plane imaging results	128
Chapter 8.	Conclusion and Outlook	132
	Appendices	138
Appendix A.	Laser systems for experiments	139
Appendix B.	The Frequency-Domain Tomography reconstruction algorithm and codes	142
Appendix C.	Publications by the author while at University of Texas	164
	Bibliography	166
	Vita	182

List of Tables

5.1	RMS deviations of FDT reconstructions from NLSE simulations.	91
7.1	Properties of and experimental conditions for producing GeV electron beams	124
8.1	Comparison among single-shot visualization techniques: frequency-domain streak camera (FDSC), frequency-domain tomography (FDT), multi-object-plane imaging (MOPI)	133
A.1	Output specifications of Alpha 10/XS 45 TW	141

List of Figures

2.1	Schematic diagram of frequency-domain interferometry.	16
2.2	Schematic diagram of frequency-domain holography. Here the probe pulse is chirped and temporally broadened to overlap the entire refractive index longitudinal profile.	19
3.1	Schematic probe-reference (P-R) pulse configurations for a. frequency-domain holography (FDH) and b. frequency-domain streak camera (FDSC) at probing angles $\theta < 90^\circ$	28
3.2	Projection angle ϕ vs. probe angle θ . Blue. FDSC with 800 nm pump and 400 nm probe in fused silica, <i>i.e.</i> $v_{pr} = 0.66c$ and $v_{ob} = 0.68c$. Red. FDSC with 800 nm pump and 400 nm probe in $3.5 \times 10^{19} \text{ cm}^{-3}$ plasma where electrons are effectively accelerated, <i>i.e.</i> $v_{pr} = c$ and $v_{ob} = 0.99c$	33
3.3	Spatially multiplexed frequency-domain streak camera (FDSC). Phase shifts on: 0° probe (top row), showing $\Delta\phi_{pr}(r, \zeta)$ integrated over z , as conventional frequency-domain holography (FDH); 14° probe (middle row), showing streaks. r_\perp denotes transverse position of the probe pulse at the interaction region. Bottom row: transmitted pump spectrum and spatial profile (inset), for initial pump intensity (left to right) $I = 0.04, 0.47, 0.93$, and 1.47 TW/cm^2	37
3.4	Measured $\Delta\phi_{pr}$ line-outs along streak axis as shown in Fig. 3.3, showing evolution of peak index shift.	38
3.5	Calculated pump intensity evolution $I(z)$ from NLSE, which is proportional to $\Delta\phi_{pr}$ line-outs.	39
4.1	Schematic experimental setup of frequency-domain streak camera (FDSC) for laser wake field accelerators. The inset plot is a typical frequency-domain hologram taken from the CCD camera detector of the spectrometer.	44
4.2	Schematic diagram of phase shift generation by laser plasma structures.	48

4.3	Reconstructed phase streak imprinted on the probe spatiotemporal profile ($t_{\text{pr}}-x_{\text{pr}}$). The phase shift shown in the left panel has only the plasma channel component ψ_p at plasma density $1.3 \times 10^{19} \text{ cm}^{-3}$, whereas the right panel shows a bubble induced phase dip at plasma density $2.0 \times 10^{19} \text{ cm}^{-3}$	51
4.4	Angular-resolved electron spectrum and probe phase streak line-outs at propagation distances from $z = 1$ to 3 mm with 0.25 mm increment different plasma density: (a) $1.3 \times 10^{19} \text{ cm}^{-3}$; (b) $1.7 \times 10^{19} \text{ cm}^{-3}$; (c) $2.0 \times 10^{19} \text{ cm}^{-3}$; (d) $2.2 \times 10^{19} \text{ cm}^{-3}$. Numbers on each curve denotes the propagation distance z value in unit of millimeter. Dashed lines show the trajectory of the center of the pump pulse.	53
4.5	3D particle-in-cell VLPL simulations of laser wakefield acceleration with optimal $\bar{n}_e = 1.5 \times 10^{19} \text{ cm}^{-3}$. (a-c) Plasma density profiles at $z = 1.6$ mm (a) , 2.0 mm (b) and 2.4 mm (c) , representing bubble formation, electron acceleration, and bubble coalescence respectively. (d) Calculated electron spectrum centered at 100 MeV.	58
4.6	Calculated probe phase shift induced by plasma bubble in 3D PIC simulations (red solid, $\bar{n}_e = 2.0 \times 10^{19} \text{ cm}^{-3}$), convolved with probe longitudinal temporal resolution $\delta t = 50$ fs (blue solid), 19 fs (blue dash), and 5.3 fs (blue dot). (a) Phase shift induced by good-shaped bubble at $z \sim 2.0$ mm. (b) Merged bubble induced phase shift at $z \sim 2.5$ mm.	59
4.7	3D PIC simulations of probe phase shift induced by laser wakefields at density: (a) $1.0 \times 10^{19} \text{ cm}^{-3}$; (b) $1.3 \times 10^{19} \text{ cm}^{-3}$; (c) $1.5 \times 10^{19} \text{ cm}^{-3}$; (d) $2.0 \times 10^{19} \text{ cm}^{-3}$. Actual phase shift profiles (red) are convolved with probe longitudinal temporal resolution $\delta t = 30$ fs (blue), illustrating the longitudinal time-resolution limit of the probe.	61
5.1	Conventional tomography for static objects in space domain (left) and Fourier domain (right).	65
5.2	Principle of tomography for light-speed object. (a) The plane in which the transformed phase streak of a single probe at θ cuts the Fourier space of the object. The normal to the plane makes angle α with the k_z axis; its projection on the (k_x, k_ζ) plane makes angle ϕ with the k_ζ axis. (b) Cones containing the region of the Fourier space which can be sampled by the probe.	67

5.3	<p>FDT Phantom simulations. (a) 2D snapshots (ζ_{ob} vs. x_{ob}) of evolving “phantom” object at seven selected positions z_{ob} after entering a medium as it propagates with velocity $v_{\text{ob}} = 0.68c$. Remaining rows show tomographic reconstructions of the phantom object for three probe configurations: (b) 19 probes at projection angles $-90^\circ < \phi < 90^\circ$ with 10° separation, $v_{\text{pr}} = 0.70c$ (configuration I); (c) 18 probes at $-90^\circ < \phi < 80^\circ$ with 10° separation, $v_{\text{pr}} = 0.681c$ (configuration II); (d) 5 probes at $-70^\circ < \phi < 70^\circ$ with 35° separation, $v_{\text{pr}} = 0.66c$ (configuration III). The color bar shows the dimensionless refractive index change of original and reconstructed objects.</p>	75
5.4	<p>Analysis of phantom simulations. (a) Peak Δn of the Gaussian “dot” vs. evolution time z_{ob}, demonstrating inter-frame resolution; (b)-(c) line-outs at $z_{\text{ob}} = 1.5$ mm of the rectangle along ζ_{ob} (b) and x_{ob} (c), demonstrating intra-frame resolution. Curves in (a)-(c) refer to phantom simulations in Fig. 5.3: original object (black dotted curve) and reconstructions with 19 (red dashed curve), 18 (blue solid curve) and 5 (green dash-dot curve) probes. (d) Normalized root mean square error of the same 3 tomographic reconstructions vs. iteration number. . . .</p>	77
5.5	<p>Schematic set-up for single-shot FDT of evolving laser-generated structures. (a) Experimental setup for probe generation and delivery to the imaging spectrometer. (b) Frequency-domain hologram, or interference pattern, of five probe and reference pulse detected by the CCD camera of the spectrometer. (c) Fourier transformation of the frequency-domain hologram yields a reciprocal hologram, in which peaks P_1 thru P_5 encode the phase modulations of the 5 probes. Phase streaks in Fig. 5.6 are recovered by windowing and inverse Fourier transforming these 5 peaks.</p>	79
5.6	<p>Phase streaks induced by the evolving index profile. $E_{\text{pu}} = 0.7\mu\text{J}$, and projection angles are $\phi = 1.0^\circ, 27^\circ, -25^\circ$ (top row), and -65° and 68° (bottom). Vertical (horizontal) scales denote transverse (longitudinal) position of the pump-induced phase streak within the temporally stretched probe pulse profile. The left-most end of each streak corresponds to the entrance of the medium; $\zeta_{\text{pr}} = x_{\text{pr}} = 0$ is approximately the mid-point of the pump pulse propagation through the Kerr medium. The spectrometer slit was centered on the images that L_2 projected at the spectrometer entrance. Color bars give phase shift in rad.</p>	82

- 5.7 Single-shot tomographic movies of the evolving index profile. **(a)** Selected 2D snapshots $\Delta n(\zeta_{\text{ob}}, x_{\text{ob}})$ of the pump nonlinear index profile at 5 different propagation positions z_{ob} indicated at top, and pump energies indicated at left. The color bar shows the dimensionless refractive index change. **(b)** Spectra of the transmitted pump pulses. The spectrum in the top row is nearly identical to the incident spectrum. **(c)** Near field images of the transmitted pump spatial profiles, with a resolution of $\sim 20 \mu\text{m}$. 84
- 5.8 NLSE-simulated movies of the evolving index profile. **(a)** Selected 2D snapshots $\Delta n(\zeta_{\text{ob}}, x_{\text{ob}})$ of the pump nonlinear index profile from NLSE simulations for the same 4 pump energies and same 5 propagation times as shown in Fig. 5.7a. The color bar indicates the dimensionless refractive index change. **(b)** Spectra of the transmitted pump pulses from NLSE simulations, for direct comparison with measured spectra shown in Fig. 5.7b. **(c)** Solid curves: NLSE-simulated pump transverse spatial profiles at $\zeta_{\text{ob}} = 0$ near the exit plane ($z_{\text{ob}} = 2.5 \text{ mm}$) for pump energy from 0.4 to 0.6 μJ , and at $z_{\text{ob}} = 1.5 \text{ mm}$ for 0.7 μJ . Dashed curves: corresponding line-outs of FDT-reconstructed pump spatial profile from Fig. 5.7a for direct comparison. . . . 85
- 5.9 Comparison of FDT data with NLSE simulations. **(a)** Reconstructed radius Δx_{ob} and **(b)** index shift $\Delta n(\zeta_{\text{ob}} = 0, x_{\text{ob}} = 0)$ at the center of Kerr profiles $\Delta n(\zeta_{\text{ob}}, x_{\text{ob}}, z_{\text{ob}})$ from Fig. 5.7a vs. propagation position z_{ob} . Data points are for various E_{pu} : red squares, 0.4 μJ ; green circles, 0.5 μJ ; blue diamonds, 0.6 μJ ; black triangles, 0.7 μJ . For $E_{\text{pu}} = 0.7 \mu\text{J}$ and $z_{\text{ob}} > 1.6 \text{ mm}$, Δx_{ob} is not well defined because of the complex Kerr profile shape, and thus is not plotted. Solid curves are from NLSE calculations taking only $n_2 I_{\text{pu}}$ into account; the dotted portion of these curves indicates the region after multiple filaments formed. Dashed curves include 4th-order Kerr effect with $n_4 = -3.3 \times 10^{-28} \text{ cm}^4 \text{W}^{-2}$ [20]. **(c)** Results of z-scan measurements of Kerr lensing by the fused silica plate, as illustrated in inset. Solid blue curve is calculated radius based on lowest-order Kerr lensing, dashed curve includes n_4 as above. **(d)** Lineout (solid blue curve) of Δn vs. x_{ob} at $\zeta_{\text{ob}} = 0$, $z_{\text{ob}} = 2.6 \text{ mm}$, showing index hole near center of the Kerr profile, compared to calculated radial distribution of plasma density (dashed curve) at $z_{\text{ob}} = 2.6 \text{ mm}$ due to 6-photon ionization. Dotted blue curve shows suppression of the Kerr profile from 4th-order Kerr effect using n_4 as above. 87

5.10	Direct comparison of measured and calculated longitudinal pulse profiles. (a) FDT reconstruction (solid line) and NLSE simulation (dashed line) of the longitudinal profile. (b) Autocorrelation trace calculated from FDT-reconstructed longitudinal profile (solid line) and direct measurement (dash line). Except for the direct autocorrelation measurement, the curves are lined out from Fig. 5.7 and 5.8 with $z_{\text{ob}} = 1.5$ mm, $x_{\text{ob}} = 0$, $E_{\text{pu}} = 0.6$ μJ	90
6.1	Schematic diagram of Multi-object-plane imaging setup. Here nonlinear phase contrast imaging is applied to resolve small phase shift induced by tenuous plasma in air.	100
6.2	Schematic diagram of small oblique angle probe. Relative positions of pump induced index structure (red) and probe pulse (blue) at different propagation distance: (a) $z = 0$; (b) $z = L/2$; (c) $z = L$	101
6.3	Multi-object-plane imaging raw data. Intensity modulation of a probe at delay $t = 1.7$ ps behind a 3 mJ pump imaged from object planes at $z_i = 3, 5, 7,$ and 9 cm, as captured by four CCD cameras. Color scales indicate probe relative intensity modulation.	103
6.4	Schematic diagram of iteration procedure in the Gerchberg-Saxton algorithm.	105
6.5	Reconstructed phase shift of plasma channel from multi-object-plane amplitude modulation. The color scale denotes the original phase shift.	106
6.6	Calibration of nonlinear phase shift and absorption in the nonlinear Kerr medium using close (left) and open (right) aperture z -scan measurements. The Kerr medium is a 1-mm thick fused silica glass at the focal plane of the 4-f imaging system shown in Fig. 6.1.	108
6.7	Four single-shot measurements of the z -evolution of the transverse index profile behind a 3 mJ pump focused in air, with probe at indicated time delays: (a) pump leading edge, where a positive electronic Kerr effect dominates; (b) pump trailing edge, where a negative plasma contribution is superposed on the electronic Kerr profile; (c) a molecular rotation time behind the pump, where the plasma contributions is superposed on a weaker delayed Kerr profile; (d) further behind the pump, where only plasma contributes. Color scales give probe phase shift in rad.	111

6.8	Probe phase shift at $z = 7.5$ cm versus pump-probe time delay on axis (a) $y = 0$ or off axis (b) $y = 100 \mu\text{m}$. Different probe polarizations are applied. Red: $\mathbf{E}_{\text{pu}}//\mathbf{E}_{\text{pr}}$; blue: $\mathbf{E}_{\text{pu}} \perp \mathbf{E}_{\text{pr}}$. . .	113
6.9	Schematic diagram of probe pulse tilting for pump-probe walk-off compensation. (a) Pump-probe walk-off for probe angle larger than θ_{min} . (b) Walk-off compensation through tilting the pulse front of the probe.	116
6.10	(a) Single-shot phase profiles with different pump-probe delays, showing effect of object-probe walk-off; (b) as in (a), but with optimally tilted probe, showing walk-off compensation, and color scales in (a-b) gives probe phase in rad.	118
7.1	Schematic diagram of PW laser-driven wakefield accelerator. The green area were in a vacuum chamber at 10^{-6} Torr. The linearly polarized PW laser pulse enters the interaction region from left. Inside the gas cell, He plasma was generated and accelerated electrons to 2 GeV which were detected by the magnetic spectrometer with two arrays of $127 \mu\text{m}$ diameter tungsten-wire fiducials 1.256 and 1.764 m after the gas cell exit. Surrounding panels include: (a) transversely scattered light imaged to a CCD camera; (b) trajectories of 2 GeV electrons relative to the fiducial arrays; (c-f) unprocessed data showing electrons up to 2.3 GeV and fiducial shadows using scintillator (c), LANEX (d), IP _{HS} (e) and IP _{HR} ; g He pressure versus time with an acoustic shock wave; h a typical laser focal spot.	122
7.2	Electron spectra and betatron X-ray profiles for three shots (a-c) from the accelerator. Column 1: low energy electrons (< 350 MeV) recorded by another image plate (IP _{LE}). Column 2: GeV electron spectra recorded on IP _{HS} . Column 3: zoom-in of high-energy tails. Column 4: vertically integrated electron energy spectra around each high-energy peak. Column 5: betatron X-ray angular distribution recorded on IP _{HS}	123
7.3	NLSE simulation illustrating topological changes of a relativistically self-focusing laser pulse. The color bars indicate the squared laser strength parameter a^2 . The laser pulse evolves according to the NLSE in a plasma of density $n_e = 5 \times 10^{17} \text{ cm}^{-3}$, through propagation distance at $z = 0$ (a), 1.5 cm (b), 2.0 cm (c), 2.5 cm (d), 3.0 cm (e), and 3.5 cm (f).	127
7.4	Multi-object-plane imaging probe intensity modulation. Three probes images the gas cell at $z = 0.9$ cm (a), 1.8 cm (b), 2.9 cm (c), respectively.	128

7.5 Reconstructed plasma wakefield induced probe phase shift in three different shots, showing spatial profile (x_{\perp}) of wakefields at different propagation distance (z). 129

A.1 Schematic diagram of the UT³ Alpha 10/XS 45 TW laser system. 140

Chapter 1

Introduction

The laser, first demonstrated by Maiman in 1960 [54], continues to transform our world. The intense brightness of laser light enables new types of light-matter interactions, and along with them, new applications. For example, tightly focused laser light cuts, welds and ablates metals and dielectrics, technologies now broadly used in industry [32]. When intense laser pulses propagate through transparent media, their strong electric fields drive electrons nonlinearly, creating nonlinear optical effects such as self-phase modulation, self-focusing, frequency up/down conversion, and parametric amplification that are enumerated in contemporary nonlinear optics textbooks[7], and used routinely in fiber optic communications and laboratory research in many scientific fields.

In the late 1980s, the development of chirped pulse amplification (CPA) paved the way for generating laser light of unprecedented intensity [78]. The CPA technique reduces the intensity of a seed laser pulse of given energy or fluence by intentionally broadening its temporal profile before amplification using dispersive optics. This so-called “chirped” pulse can then be amplified by 6 to 12 orders of magnitude, and compressed into an ultra-short, ultra-intense

laser pulse, without damaging the amplification system. Contemporary CPA laser technology reliably delivers femtosecond laser pulses with hundreds of terawatts [1 terawatt (TW) = 10^{12} watts (W)] peak power — equivalent to the average power of the world-wide electrical grid — a capability now commercialized and implemented in universities and research institutes around the world. Major labs in the United States, Europe, and Asia have built, or are constructing, lasers that generate pulses of petawatt peak power [1 petawatt (PW) = 10^{15} W], with focal peak intensity up to 10^{21} W/cm², sufficient to drive highly relativistic electron motion and open up a new area of relativistic nonlinear optics [61]. Laser-matter interactions at such intensity promise to provide tabletop particle accelerators and coherent x-ray sources for the next generation. The study of ultra-intense laser-matter interaction, and the development of diagnostic tools to visualize and characterize those interactions, are thus new and of great current interest to forefront science and technology.

1.1 Nonlinear laser pulse propagation in transparent dielectrics and gases

Nonlinear propagation of femtosecond laser pulses in transparent media such as dielectrics and gases has been extensively studied since self-channeling, or filament propagation, of a laser pulse through air was observed in the mid-1990s [8]. In filament propagation, a laser pulse self-guides at high intensity over multiple Rayleigh ranges because its nonlinear Kerr lens dynamically balances its lateral spread via diffraction and plasma defocusing [23]. Meanwhile,

self-phase modulation broadens the laser spectral bandwidth, sometimes as widely as the entire visible spectrum [2], while plasma is generated via photoionization [39]. This unique combination of processes enables applications such as white light detection and ranging (LIDAR), atmospheric chemical analysis, lightning protection, and dielectric micro-machining [13], highlighting the importance of observing and understanding the underlying nonlinear dynamics.

Nonlinear filament propagation of femtosecond laser pulses can be modeled by a wave equation — the so-called nonlinear Schrödinger equation (NLSE) — derived from Maxwell’s equations with the assumptions that the field $\mathbf{E} = \Re[E \exp(ik_0z - i\omega_0t)]$ of the laser pulse (i) is linearly polarized, (ii) propagates paraxially, and (iii) has a scalar envelope E that varies slowly [13]:

$$\begin{aligned}
\frac{\partial E}{\partial z} &= \frac{i\hat{T}^{-1}}{2k_0} \nabla_{\perp}^2 E - \frac{ik''}{2} \frac{\partial^2 E}{\partial \tau^2} + N_{Kerr} + N_{plasma} + N_{PI} \\
N_{Kerr} &= ik_0 n_2 \hat{T} \left[(1 - f_R) |E|^2 + f_R \int_{-\infty}^{\tau} R(\tau - \tau') |E(\tau')| d\tau' \right] E \\
N_{plasma} &= -\frac{ik_0}{2n_0^2 \rho_c} \hat{T}^{-1} \rho E - \frac{\sigma}{2} \rho E \\
N_{PI} &= -\frac{W_{PI} E_g}{2|E|^2} E.
\end{aligned} \tag{1.1}$$

The first line is the NLSE, while the remaining lines define the last three terms on its right-hand side. The time variable is $\tau = t - z/v_g$, so the wave equation is written in the co-moving frame of the laser pulse. The first and second terms on the right-hand side of the wave equation denote, respectively, linear diffraction in the transverse plane and group velocity dispersion (GVD) in the longitudinal direction. The nonlinear Kerr term N_{Kerr} , defined in the second

equation, includes an instantaneous and a time-delayed component, the latter related to activation of low energy transitions between molecular ro-vibrational states. The plasma term N_{plasma} , defined in the third equation, describes defocusing and absorption of the laser pulse by the plasma that it generates at high-intensity. The last term N_{PI} , defined in the fourth equation, describes loss of laser energy by photo-ionization. The operator $\hat{T} = 1 + (i/\omega_0)(\partial/\partial\tau)$ is an adjustment to the slow-variation assumption that acts on the diffraction term to account for time-space focusing, and on the Kerr term to account for self-steepening.

Generation and recombination of plasma is described by a second equation that is coupled to the NLSE (1.1). If the peak intensity of the femtosecond laser pulse exceeds $\sim 10^{13}$ W/cm², it generates plasma efficiently via photo-ionization and collisional avalanche ionization:

$$\frac{\partial\rho}{\partial\tau} = W_{PI}(|E|^2) + \frac{\sigma}{E_g}\rho|E|^2 - \frac{\rho}{\tau_{rec}}. \quad (1.2)$$

Here W_{PI} represents the photo-ionization rate, which can be obtained from the formulation of Keldysh [39] and Perelmov, Popov and Terent'ev (PPT) [63], which generalized two different photo-ionization mechanisms: multi-photon ionization at lower laser intensity and tunneling ionization at higher intensity. Another mechanism is avalanche ionization, the rate of which is proportional to the existing plasma density ρ , as shown in the second term of Eq. (1.2). Recombination is described by a plasma life time τ_{rec} in the third term.

Couairon *et al.* [13] have reviewed the mechanisms of laser filamenta-

tion. In gases, filaments form in two stages: (i) the pure Kerr compression stage in which the laser pulse keeps self-focusing till it reaches the ionization threshold of the medium, and (ii) the balancing stage in which the intense part of the pulse loses energy through photo-ionization, clamping its peak intensity near 10^{13} W/cm², while the trailing part of the pulse balances between self-focusing and plasma defocusing. In solids, collapse of the self-focusing laser pulse is generally arrested by longitudinal pulse splitting, although details vary depending on initial conditions. For pulses focused into the Kerr medium with beam radius $w_0 \sim 20$ to 30 μm with peak power above the critical power for self-focusing, photo-ionization and plasma defocusing are the main mechanisms that drive pulse splitting [87]. For more loosely focused incident laser pulses ($w_0 \geq 100$ μm) near the critical power, the large dispersion of solids compared to gases becomes important. The first pure Kerr compression stage is gradual and slow, so accumulated dispersion due to GVD splits the pulse and arrests beam collapse before significant ionization and plasma generation [68]. At the opposite extreme of a tightly focused incident laser ($w_0 \leq 5$ μm), the incident intensity is already so large that plasma density can reach 10^{20} cm⁻³ [79]. In this case, avalanche ionization is as important as photo-ionization, and the medium is altered permanently, as occurs e.g. in laser micro-machining, due to the lower damage threshold of solids compared to gases.

The established filamentation mechanism in gases summarized above was recently challenged, based on new measurements of high-order Kerr effect

(HOKE) indices in nitrogen, oxygen, and argon [52]. In HOKE, the lowest order Kerr index n_2I is augmented by high-order terms of the form $n_4I^2 + n_6I^3 + n_8I^4 + \dots$, which measurements suggested could be opposite in sign, and comparable in magnitude, to n_2I in some gases. The proposed new mechanism suggested that instead of plasma generation, the saturation of the lowest-order nonlinear Kerr index by HOKE terms was responsible for the arrest of beam collapse [4]. The significance of HOKE in gases is still under investigation, whereas this effect in condensed matter, e.g. glass, has not been discussed, although a measurement of n_4 in fused silica has been reported [20]. This issue will be discussed further in Chapter 5.

The complex dynamics of laser pulse filamentation described above provide the subject of study for our development of several single-shot visualization techniques: the frequency-domain streak camera (FDSC, Chapter 3), frequency-domain tomography (FDT, Chapter 5), and multi-object-plane phase-contrast imaging (MOP-PCI, Chapter 6). The FDSC provides a time sequence of projections of the growing filament. FDT combines several FDSC projections to reconstruct a complete single-shot “movie” of the filament’s refractive index dynamics, albeit over a short (\sim mm) propagation length. MOP-PCI visualizes the filament structure and dynamics over meter-scale propagation lengths.

1.2 Laser-plasma electron acceleration

Ultrafast, ultra-intense laser pulses propagating with terawatt or petawatt peak power in underdense plasma can capture and accelerate electrons to MeV or GeV energy, promising a new generation of compact, inexpensive accelerators [47]. Compared to conventional linear GeV electron accelerators, which accelerate electrons using fields of ~ 100 kV/cm relayed over kilometers via cryo-cooled metal accelerating structures, laser wake field accelerators (LWFAs) sustain accelerating fields of ~ 1 GeV/cm, implying that electrons could be accelerated up to tens of GeV on a table-top. As a result, GeV electron beams and bright coherent x-ray radiation could become affordable to university-based labs for a broad range of research in biology, medicine, and materials science.

Tajima and Dawson [82] proposed the LWFA concept in 1979. Esarey et al. [21] recently reviewed the history and principles of LWFA. Early experimental demonstrations of laser-plasma acceleration were based on beat-wave acceleration, in which two laser beams with frequencies ω_1 and ω_2 such that $\omega_1 - \omega_2 = \omega_p$ (the plasma oscillation frequency), usually provided by two lines of a CO₂ laser, excited and resonantly drove a plasma beat wave at ω_p that captured and accelerated plasma electrons [11, 41]. After the invention of solid-state CPA laser systems, single intense laser pulses proved to be more efficient, and widely available, drivers of plasma waves for electron acceleration. Early CPA drivers, however, produced pulses that were significantly longer than the plasma wavelength in plasmas for which the peak power exceeded

the critical power ($P_c = 17(\omega/\omega_p)^2$ GW) for relativistic self-guiding, a necessary condition for efficient electron capture and acceleration. Under these conditions, the pulse generated a plasma wave by a Raman forward scattering (RFS) instability [60]: *i.e.* the initially excited plasma wave modulated the drive pulse, causing it to evolve into a train of shorter pulses, each of duration $\sim \omega_p^{-1}$. These pulses then resonantly (and more strongly) drove the plasma wave, which in turn more strongly modulated the drive pulse amplitude, etc. In the frequency domain, this modulated pulse developed Stokes and anti-Stokes sidebands separated from the original center frequency by ω_p . The modulated pulse interacting with the plasma was thus similar to the beat-wave accelerator, except that the sidebands developed during the interaction rather than being input from the laser. In the self-modulated LWFA, the plasma wave grew quickly, until it trapped electrons, and accelerated them to multi-MeV energy [15]. The electron energy spectrum, however, resembled a Boltzmann distribution with most electrons at low energy (~ 1 MeV), and only an exponential tail extending up to the maximum energy (typically tens of MeV). These accelerators were thus useful only for niche applications, such as nuclear activation of short-lived isotopes [46], that did not require narrow energy spread. Le Blanc *et al.* measured the growth and decay dynamics of the self-modulation instability directly by Thomson-scattering a time-delayed probe pulse from the plasma wave over multiple shots [45]. This experiment demonstrated that the plasma wave amplitude grew via the RFS instability [60] and decayed within ~ 1 ps because of beam loading [91]. It was one of the

first experiments to detect laser-driven plasma waves directly via the modulation they imposed on probe pulses, and thereby to elucidate underlying LWFA physics. It is therefore an important precursor of the work presented in this dissertation.

Further advances in CPA technology enabled generation of shorter, more powerful laser pulses. It thus became possible to excite plasma wakes with laser pulses of duration close to ω_p^{-1} that were powerful enough to self-guide [55]. This development culminated in 2004, when three groups simultaneously and independently demonstrated that LWFA could produce nearly monoenergetic electron spectra [22, 28, 56]. In these experiments, ultrashort laser pulses drove plasma waves resonantly (laser pulse duration equal to the plasma wavelength). The ponderomotive force of the laser pulse ejected electrons strongly in all directions from its envelope, creating the so-called “blow-out” or “bubble” regime. Simulations [66], and shortly afterward experiments, demonstrated that in the bubble regime electrons could be accelerated to 60 to 170 MeV with a nearly monoenergetic spectrum. This feature is critical for most applications of relativistic electron beams. In 2006, a pre-formed capillary waveguide was applied to guide laser propagation, thereby increasing acceleration length beyond what relativistic self-guiding allowed. As a result, 1 GeV electrons with $\sim 5\%$ energy spread were obtained from laser wake field accelerators for the first time [48]. Recently, our group generated 2 GeV quasi-monoenergetic electron beams by driving the laser wake field accelerator with a petawatt laser [89]. Chapter 7 discusses this last experiment in more detail.

The mechanisms of electron injection and acceleration in the blow-out regime, and efforts to optimize and scale them, are ongoing subjects of forefront theoretical and simulation research [53, 66]. Unlike the self-modulated LWFA, the blow-out regime allows an approximately “non-evolving” laser spatiotemporal profile to drive a highly nonlinear plasma wave in which electrons are ejected completely from an approximately spherical volume, leaving a positively charged bubble trailing the laser pulse. Ambient plasma electrons can inject spontaneously, or with prompting by an auxiliary laser pulse [22], into the rear of the bubble. They then accelerate in the strong longitudinal electrical field inside the cavity to MeV or GeV level over a distance that is limited by pump depletion and/or by de-phasing between the accelerating electrons propagating at $\sim c$ and the bubble propagating at the drive pulse group velocity. A unique advantage of this bubble regime is the existence of an efficient injection termination mechanism, which prevents electrons from injected constantly into the bubble and forming a low-energy tail in the spectrum. Nevertheless, the dynamics of injection and the early stages of acceleration remain one of the most elusive aspects of the physics of plasma acceleration in the bubble regime. At low plasma density ($n_e \sim 10^{17} \text{ cm}^{-3}$) required for GeV acceleration, injection into static bubbles becomes inefficient unless the bubble is exceptionally large. Kalmykov *et al.* have proposed through simulations that in this regime self-focusing and defocusing of the drive laser pulse in the plasma, and the resulting elongation and contraction of the bubble, can effectively turn injection on and off [38]. The possibility of observing this elongation and contraction

dynamics of the plasma bubble directly in the laboratory, as an aide to understanding and controlling electron injection, is one of the important motivations behind the work of this dissertation.

Laser wake field accelerators are potential tabletop femtosecond hard x-ray sources [12]. X-ray production requires transverse modulation of the electron trajectories. There are three ways of doing this. First, the *transverse* electric field of the plasma bubble provides a restoring force for transverse oscillations of electrons that are injected off-axis, even while they are accelerating in the bubble’s longitudinal field. This so-called “betatron” motion produces bright, directional keV x-ray synchrotron radiation [72]. Second, accelerated free electrons emerging from the accelerator can be transversely modulated by a counter-propagating laser field, yielding gamma ray radiation of hundreds of keV photon energy [81]. Finally, coupling of a LWFA electron beam into a conventional magnetic undulator has produced efficient synchrotron radiation at visible [73] or soft x-ray [25] wavelengths. Further optimization and scaling of LWFA beams may enable tabletop x-ray free electron lasers [62] that could rival the Linac Coherent Light Source (LCLS) or the Free-Electron Laser at Hamburg (FLASH) in peak brightness. The possibility of such transformative advances in experimental science further motivates our development of visualization techniques that support the needed optimization and scaling of LWFAs.

1.3 Ultrafast refractive index structures in laser-matter interactions

The processes of laser filamentation and laser wakefield acceleration discussed in the previous sections (1.1) and (1.2) create complex, evolving refractive index structures of micron size and femtosecond time scale that co-propagate at light speed with the laser. They present a daunting, new challenge to laboratory visualization. We will show that visualization of such index structures and their evolution reveals key underlying physics of these processes. Designing and interpreting any visualization method requires an understanding of the physical origin of the refractive index modulation.

For laser filament propagation in gases or condensed media, the nonlinear refractive index $\Delta n = n_2 I$ is a significant contribution to the index shift. The near-instantaneous electronic component of the nonlinear index directly characterizes the laser pulse amplitude or intensity profile. However, as we shall see in Chapter 6, the nonlinear refractive index can also have a time-delayed component if the laser pulse propagates in molecular gases with rotational degrees of freedom. The possible importance of high-order Kerr effect (HOKE) can be tested by measuring laser-induced refractive index variations. The relativistic nonlinear index that ultra-intense laser pulses produce in fully-ionized plasma can provide a unique way of measuring their intensity during nonlinear propagation.

Plasma generated during laser-matter interaction also contributes a

negative index shift η given by

$$\eta = \sqrt{1 - \frac{\omega_p^2}{\omega^2}} = \sqrt{1 - \frac{n_e}{n_c}} \quad (1.3)$$

where $\omega_p = \sqrt{4\pi e^2 n_e / m_e}$ is the plasma frequency and $n_c = m_e \omega_p^2 / (4\pi e^2)$ is the critical density — *i.e.* the density at which $\omega_p = \omega$. Plasma generation plays a key role in arresting the collapse of self-focusing pulses in both condensed media (Chapter 5) and gases (Chapter 6). Thus the direct detection of plasma generation plays a key role in characterizing self-guided filament formation. In laser wakefields, the complex plasma density profile created by ionization and nonlinear plasma wave excitation can be reconstructed from measurements of the transient refractive index. At ultra-high light intensity ($\sim 10^{18}$ W/cm²), the index given by Eq. (1.3) is modified by the relativistic effect

$$\eta = \sqrt{1 - \frac{n_e}{n_c \gamma}}, \quad (1.4)$$

where $\gamma = \sqrt{1 + a_0^2/2}$ is the relativistic Lorentz factor, and $a_0 = 0.85\sqrt{I[10^{18} \text{ W/cm}^2]\lambda^2[\mu\text{m}]}$ is the normalized vector potential. The measured index structure not only provides a detailed and unprecedented diagnosis of plasma density, but also indirectly derives the longitudinal and transverse electrical fields inside the bubble, helping determine the optimal operation regime for electron acceleration and x-ray generation.

Chapter 2

Prior optical techniques for visualizing light-speed index structures

The transient refractive index structures studied in this work travel with a driving laser pulse at its group velocity $v_g = \partial\omega/\partial k$ along the z -direction. Thus the longitudinal profile of the index structures can be described with a local time variable $\zeta = t - z/v_g$. Incorporating transverse coordinates x and y , a full four-dimensional (4D) history of the index structure profile can therefore be expressed mathematically as $\Delta n(\zeta, x, y, z)$. The typical scale of ζ variations is femtoseconds; the typical scale of x, y variations is microns; the propagation distance z ranges from ~ 1 mm to several meters for experiments reported in this dissertation.

The central topic here is optical visualization of the complete evolving optical index structure $\Delta n(\zeta, x, y, z)$ in a single shot. Prior to the work of this dissertation, however, some techniques had already been developed to visualize such light-speed index structures partially. In fact, three previous Ph.D. dissertations from our group have been devoted to this task: Craig Siders (1996), Nicholas Matlis (2006) and Peng Dong (2010). In this chapter, we review the relevant prior art developed by our group as well as outside

researchers, and point out the limitations of previous visualization techniques. Section 2.1 discusses frequency-domain interferometry (FDI), used by Siders to measure laser-driven plasma wakes. FDI usually measures the ζ structure of the object only, averaging over x , y and z . However, it requires multiple shots to measure ζ structure, and thus relies on repeatability of the object’s structure, to build up an image. Section 2.2 discusses frequency-domain holography (FDH), used by Matlis to visualize laser-driven quasi-linear plasma wakes, and (with modifications) by Dong to measure highly nonlinear laser wakes in the bubble regime. FDH records an ζ - x slice of the object’s structure in a single shot, but averages over z variations. Section 2.3 discusses transverse probe techniques developed by outside researchers to measure z evolution of light-speed objects. However, these methods require multiple shots, and average over the object’s transverse (x , y) structure. Subsequent chapters will then describe three techniques developed in this work to visualize the z -variation of a light-speed object in a *single* shot, while simultaneously recording one or more dimensions of its ζ - x - y structure with high fidelity. We call these new techniques the frequency domain streak camera (FDSC, Chapter 3), frequency domain tomography (FDT, Chapter 4), and multi-object-plane phase-contrast imaging (MOP-PCI, Chapter 5).

2.1 Frequency–Domain Interferometry

Frequency-Domain Interferometry (FDI), also known as Fourier-domain interferometry or spectral interferometry, is a linear technique to measure the

phase and amplitude of an unknown optical electrical field $E(\zeta)$ by interfering it with a well-characterized reference pulse in a spectrometer [30, 83]. In this technique (Fig. 2.1), the ultrashort probe pulse is altered in phase and amplitude as a result of co-propagating with a light-speed index structure at a specific time delay ζ , which is controlled by adjusting the delay between the probe and the pump pulse that produces the structure. Compared to the twin reference pulse propagating ahead of the pump, the probe pulse acquires an extra phase shift $\Delta(x, y, \zeta)$ due to its interaction with the index structure. After being filtered (*e.g.* spectrally) from the co-propagating pump pulse, the probe and reference, separated in time by T_0 , are sent to a spectrometer.

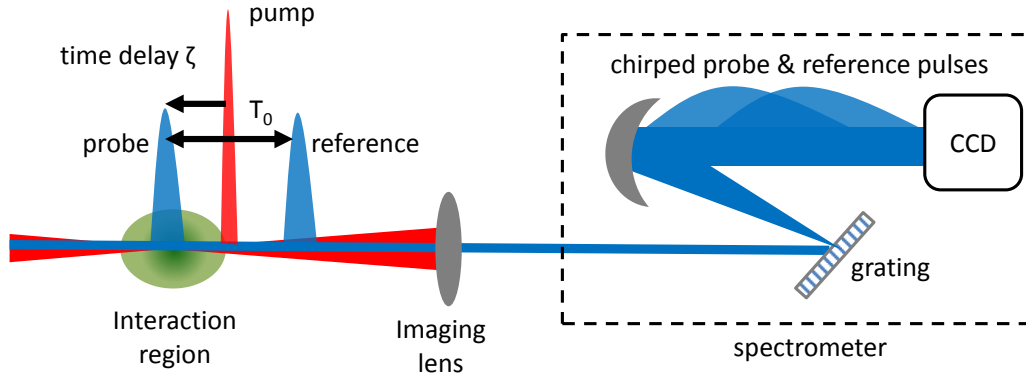


Figure 2.1: Schematic diagram of frequency-domain interferometry.

Unlike conventional (*e.g.* Young's double-slit) interferometry, in which two beams impinge simultaneously at different incident angles onto a detector, FDI utilizes a spectrometer to collect co-propagating pulses arriving at different times. The interference pattern then forms at a charge-couple device

(CCD) camera in the spectrometer’s detection plane after a grating spectrally disperses the probe and reference pulses. Even though these pulses are temporally separated as they enter the spectrometer, they overlap and interfere at the spectrometer’s detection plane. This happens because the dispersive grating separates frequency component of the pulses at different angles. Thus a single pixel detects only a small fraction of the dispersed angular range, and thus nearly monochromatic light, which is “infinite” in duration. Consequently probe and reference pulses overlap temporally, and interfere, at the detector.

Stated mathematically, the spectrometer Fourier transforms the reference pulse $E(\zeta)$ to $\tilde{E}(\omega)$, and the delayed probe $E(\zeta + T_0 + \Delta(x, \zeta))$, with object-induced phase shift $\Delta(x, \zeta)$, to $\tilde{E}(\omega) \exp(-i\omega(T_0 + \Delta))$. Here x represents transverse distance along the direction of the spectrometer’s slit, which selects a line of constant $y = y_0$ from the incoming light. The spectrometer’s CCD thus records a signal

$$I(\omega) = \left| \tilde{E}(\omega) + \tilde{E}(\omega)e^{-i\omega T_0} \right|^2 = 2 \left| \tilde{E}(\omega) \right|^2 [1 + \cos(\omega(T_0 + \Delta(x, \zeta)))] . \quad (2.1)$$

The cosine term is responsible for a set of frequency-domain fringes recorded on the CCD camera. In the absence of an object (*i.e.* $\Delta(x, \zeta) = 0$), straight parallel fringes are observed. In the presence of $\Delta(x, \zeta)$, the fringes distort along x , and shift in frequency compared to the straight unperturbed fringes. Thus the phase shift experienced by the probe can be extracted by measuring the fringe shifts in the frequency domain, analogous to conventional interferometry. To measure x -dependent fringe distortion, and thus a transverse (x)

profile of the object at time delay ζ , accurately, the probe and reference pulses must be imaged from the exit plane of the interaction region to the entrance slit of the spectrometer (see the imaging lens in Fig. 2.1), which selects a line of constant $y = y_0$ in the imaged reference-probe x - y profile. The spectrometer's internal optics then images the slit to the detector. Many applications of FDI, however, did not use such relay imaging, or used imaging optics of insufficient quality to resolve transverse variations of index objects created by pump pulses focused tightly to micrometer-scale transverse size. In these cases, FDI yields only a transverse-space-averaged phase shift $\Delta(\zeta)$. To measure $\Delta(\zeta)$ as a function of time delay ζ , frequency-domain interferograms must be recorded over multiple shots with different pump-probe delays.

In the 1990s, FDI was widely used to measure femtosecond dynamics of various laser-matter interactions [17, 30, 83]. One example is the first direct observation of a laser-driven plasma wake by Siders *et al.* [75]. By varying pump-probe delay at fixed helium gas density or helium gas density at fixed delay over multiple shots, phase shift oscillations $\Delta(\zeta)$ consistent with plasma wake excitation were observed. The oscillation period was consistent with the corresponding plasma density. Moreover, this experiment demonstrated a large electron density modulation ($\delta n_e/n_e \sim 1$) and a corresponding longitudinal accelerating field up to 10 GV/m. However, transverse structure of the plasma wave was not resolved.

2.2 Frequency–Domain Holography

FDI measures the index shift at the specific ζ position with which the fully compressed ultrashort probe pulse overlaps. Frequency-Domain Holography (FDH) uses the same pump-probe geometry as FDI, except that the probe pulse is broadened, or chirped, to cover a wide range of ζ positions at once (Fig. 2.2), enabling measurement of an object’s ζ structure in a single shot. In 2000, Le Blanc *et al.* measured the temporal profile of the nonlinear refractive index of a laser pulse in glass and of an ionization front in air in a single shot by spectrally interfering a chirped probe with an un-chirped reference [5]. However, the frequency domain hologram showed low interference fringe contrast due to different chirp phase between the probe and the reference. Improved fringe contrast was achieved by equivalently chirping the probe and reference [29].

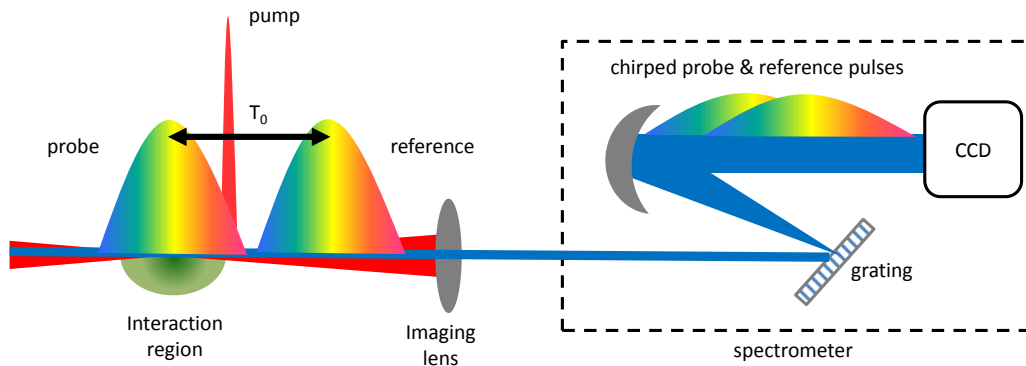


Figure 2.2: Schematic diagram of frequency-domain holography. Here the probe pulse is chirped and temporally broadened to overlap the entire refractive index longitudinal profile.

The amplitude and phase of the field of a laser pulse can be expressed either in the time $E(\zeta) \exp i\Phi(\zeta)$ or frequency $\tilde{E}(\omega) \exp i\phi(\omega)$ domain; the descriptions are connected through Fourier transformation. FDH obtains frequency domain phase shift $\phi(\omega)$, and needs to convert it to temporal phase shift $\Phi(\zeta)$ to recover the index structure's longitudinal profile. Kim *et al.* suggested two methods of conversion: direct frequency-to-time mapping and full Fourier transformation [40]. Direct mapping uses the fact that red spectral components travel ahead of blue components in a normally chirped pulse; thus phase shifts induced on red components occur at earlier time delay ζ . Assuming only linear GVD, the frequency-to-time mapping relation is

$$\Phi(t) = \phi(\omega(t)) = \phi\left(\omega_0 + \frac{t}{2\beta_2[1 + \beta_2^{-2}\Delta\omega^{-4}]}\right). \quad (2.2)$$

where β_2 is GVD as defined in Chapter 1 and $\Delta\omega$ is the bandwidth. Tokunaga *et al.* [84] showed that the temporal resolution of direct frequency-to-time mapping is

$$t_{\text{res}} = \Delta\omega^{-1} \sqrt{1 + 2\beta_2^2 \Delta\omega^4}, \quad (2.3)$$

implying that excessive chirp degrades temporal resolution.

Most contemporary applications of FDH adopt full Fourier transformation to extract $\Phi(\zeta)$ from measured $\phi(\omega)$. Matlis reviewed this procedure in detail in his Ph.D. dissertation [58]. Unlike direct mapping, temporal resolution in Fourier transform mode is unaffected by chirp, once it is reliably measured. Temporal resolution is determined only by probe bandwidth. As an example, consider a Gaussian pulse in the frequency domain

$\tilde{E}_0(\omega) = \exp \left[-(\omega^2/\Delta\omega)^2 + i\beta_2\omega^2 \right]$. Its temporal profile is

$$E_0(\zeta) = \int_{-\infty}^{\infty} \tilde{E}_0(\omega) \exp(-i\omega\zeta) d\omega = \left(\frac{\pi}{1/\Delta\omega^2 - i\beta_2} \right)^{1/2} \exp \left[\frac{\zeta^2}{4(1/\Delta\omega^2 - i\beta_2)} \right], \quad (2.4)$$

which is also Gaussian. For simplicity, we define coherence time $t_c \equiv 1/\Delta\omega$ and dispersion time $t_b \equiv \sqrt{\beta_2}$, and introduce a Gaussian-shaped index shift in the time domain $\Phi(\zeta) = \delta \exp(-\zeta^2/t_0^2)$ where $\delta \ll 1$. The disturbed probe becomes $E(\zeta) = E_0(\zeta) \exp i\Phi(\zeta)$, and its Fourier transform is

$$\tilde{E}(\omega) = \tilde{E}_0(\omega) + i\delta \left[1 + \frac{4(t_c^2 - it_b^2)}{t_0^2} \right]^{-1/2} \exp \left[-\frac{\omega^2}{(t_c^2 - it_b^2)^{-1} + 4t_0^{-2}} \right]. \quad (2.5)$$

The phase shift in the frequency domain is thus

$$\begin{aligned} \phi(\omega) &= \arg \left(\frac{\tilde{E}(\omega)}{\tilde{E}_0(\omega)} \right) \approx \arg \left[\exp \left(\frac{\tilde{E}(\omega) - \tilde{E}_0(\omega)}{\tilde{E}_0(\omega)} \right) \right] \\ &= \delta \left[\left(1 + \frac{4t_c^2}{t_0^2} \right)^2 + \left(\frac{4t_b^2}{t_0^2} \right)^2 \right]^{-1/4} \exp \left(\frac{4A\omega^2/t_0^2}{A^2 + B^2} \right) \cos \left(\frac{4B\omega^2/t_0^2}{A^2 + B^2} - \psi \right) \end{aligned} \quad (2.6)$$

where

$$A = \left(\frac{t_c^2}{t_c^4 + t_b^4} + \frac{4}{t_0^2} \right) \frac{t_c^2}{t_c^4 + t_b^4} - \frac{t_b^4}{(t_c^4 + t_b^4)^2}, \quad (2.7)$$

$$B = \frac{4t_b^2/t_0^2}{t_c^4 + t_b^4} + \frac{2t_c^2 t_b^2}{(t_c^4 + t_b^4)^2}, \quad (2.8)$$

$$\psi = \frac{1}{2} \arctan \left(\frac{t_b^2}{t_c^2 + t_0^2/4} \right). \quad (2.9)$$

The result (2.6) – (2.9) shows that the Gaussian-shaped perturbation in the time-domain becomes a Gaussian multiplied by an oscillatory term in the frequency domain. If $A > 0$, $\phi(\omega)$ diverges as $|\omega| \rightarrow \infty$. In this case, $\Phi(\zeta)$

cannot be reconstructed. Thus the condition $A < 0$ defines the temporal resolution of FDH using full Fourier transformation:

$$t_{\text{res}} = \min(t_0) = 2t_c \sqrt{\frac{t_b^4 + t_c^4}{t_b^4 - t_c^4}}. \quad (2.10)$$

For ordinary chirped pulse, $t_b \gg t_c$ is easily satisfied. The resolution limit is then of order t_c , implying that the temporal resolution of FDH is only determined by the bandwidth of the probe laser pulse.

We can also re-visit the resolution limit of the direct frequency-to-time mapping approach in light of Eqs. (2.6) – (2.9). In Eq. (2.6), the Gaussian component showed that the width of the frequency domain phase shift $\phi(\omega)$ is $t_0\sqrt{(A^2 + B^2)}/A/2$, thus the linear mapping relation maintains if A and B are independent on t_0 . This requires that $t_0^2 \gg t_c^2 + t_b^4/t_c^2$, or $t_0 \gg (1/\Delta\omega)\sqrt{1 + \beta_2^2\Delta\omega^4}$, similar to Eq. (2.3). If $t_0 \approx t_{\text{res}}$ breaks this limit and chirp is applied (*i.e.* $t_b \gg t_c$), the oscillation term is proportional to $\cos(\omega^2 t_b^2)$ and strongly modulate the probe spectral profile with a period of $t_b^{-1} \ll \Delta\omega$, as discussed in reference [40].

FDH has been applied widely to laser–matter interactions, such as laser filamentation in air [88] and laser wake field acceleration [57]. The LWFA experiment not only recovered the longitudinal temporal profile of the plasma wake in a single shot, but also recovered its transverse profile by carefully imaging the exit plane of the interaction region to the incident slit of the spectrometer [57]. The reconstructed time-domain phase shift is related to

the quasi-static wakefield index structure by

$$\phi(\zeta, x) = \frac{2\pi}{\lambda_{pr}} \int_0^L \Delta n(\zeta, x, y_{\text{slit}}, z) dz \approx \frac{2\pi L}{\lambda_{pr}} \langle \Delta n(\zeta, x, y_{\text{slit}}, z) \rangle_z. \quad (2.11)$$

Eq. (2.11) represents a 2D snapshot of the plasma wakefield since refractive index profile is equivalent to an electron density profile. The added transverse dimension enabled the observation of relativistically curved plasma wavefronts in the plasma wake. The wavefronts curve because that electron effective mass on axis increases relativistically due to strong electron quiver motion. Consequently plasma frequency decreases compared to off-axis areas based on Eq. 1.4. Such wavefront curvature had never previously been observed in the laboratory. This observation demonstrated the physical significance of measuring index profiles $\Delta n(\zeta, x)$ in the laboratory.

However, FDH cannot resolve z -variation of the index structure because the collinear pump–probe geometry (Fig. 2.2) averages the phase shift imprinted on the probe profile at different z positions. Matlis *et al.* obtained physically insightful FDH snapshots of laser-driven wakes in a weakly nonlinear regime of laser-plasma interaction in which the plasma structure evolved minimally during its transit through interaction region [57]. Later, Peng Dong *et al.* applied FDH to the highly nonlinear “bubble” regime of laser-plasma acceleration, in which the bubble shape varied significantly during its light speed propagation through the interaction region [18]. This work reconstructed optical signatures of the bubble in both the amplitude and phase of the co-propagating probe pulse. Moreover, FDH proved a sensitive probe of

the presence of a bubble and of its shape near the end of the interaction region. However, FDH could not observe bubble formation and dynamics that plays a critical role in modern laser wakefield accelerators. In Chapters 4 and 7, we will present results of new optical visualization methods that reveal bubble formation and dynamics in a single shot, and correlate them quantitatively with computer simulations and electron beam properties.

2.3 Transverse probing techniques

Besides FDI and FDH, which can be classified into a big family of spectral interferometry techniques, another class of established techniques for visualizing light-speed index objects uses an ultrashort probe that crosses the interaction regime at approximately right angles, which we call “transverse probing” techniques. In these techniques, a probe propagating along the y -direction can take a snapshot of the index structure’s longitudinal ζ -profile and transverse x -profile in one shot at a specific z -position when the probe crosses the interaction region, much as we would take a snapshot of a horse galloping by in front of us. Thus transverse probing capture a “moment” of the object’s history at a specific z . The transverse probe can then resolve the index structure’s evolution along z in multiple shots by varying the arriving time of the probe. This is analogous to taking a snapshot of the horse at a slightly different phase of its gallop cycle each time it circles the race track, in order to build up a motion picture.

One example of transverse probing of a light-speed object is visual-

ization of a laser wakefield and its accelerated electron beam by Buck *et al.* [9]. To visualize the plasma wake of period ≤ 100 fs, a 6 fs long probe pulse crossed its path at right angles; density maxima in the plasma wake then refracted the probe, producing a shadowgraph in the far field that accurately registered the plasma period. In addition, accelerating electrons within the wake were detected by observing their magnetic fields pervading surrounding plasma via Faraday rotation of the transverse probe. Faraday rotation was used (instead of shadowgraphy) to observe these highly relativistic electrons because they contribute very little to the refractive index due to their high relativistic masses. A similar multi-shot transverse probing technique, albeit with longer pulses, was used for visualizing the propagation of a laser filament in air [1]. Here the authors used a standard in-line holography method in which the object plane of the imaging system was shifted from shot to shot. The phase shift of the probe wave front was then calculated from its measured far-field diffraction pattern with standard phase-retrieval algorithms.

Although they resolve z -variation, existing transverse probing techniques have intrinsic limitations for single-shot imaging. First of all, the z -dependent information is related to the arrival time of the probe, which has to be adjusted from shot to shot. Thus (like FDI) these techniques are not viable for visualizing non-repetitive or stochastic events typical of highly nonlinear interactions, propagation in turbulent media, or interactions driven by sources with low repetition rate, unstable pointing or other shot-to-shot fluctuations. Secondly, the resolution of each transverse ‘snapshot’ is limited by probe tran-

sit time across the object. Thus the transverse size of the index structure must be less than longitudinal structures of interest (*e.g.* a plasma wavelength), typically micrometers, and vulnerably ultrashort, un-chirped probe pulses must be used. Finally, transverse probing technique is practically limited to ≤ 1 cm propagation distance. Beyond this distance, extremely large aperture optics and detectors are required, making the cost of optical diagnosis prohibitive.

Chapter 3

Frequency–Domain Streak Camera

This chapter presents the first, and simplest, of three new techniques developed in this dissertation work for visualizing evolving light-speed objects in a single shot. The so-called Frequency-Domain Streak Camera (FDSC) borrows from Frequency-Domain Holography (FDH) the use of a temporally-stretched, chirped probe pulse and spectral interferometry phase recovery methods, as described in the previous chapter. FDSC differs from FDH in using a probe pulse that propagates at a small oblique angle to the object’s path, instead of co-propagating with the object. As a result, the object imprints a “phase streak” on the probe pulse profile that is recovered by spectral interferometry methods, and yields a temporal sequence of the object’s projections. Section 3.1 presents the theory of FDSC, including the relationship between laboratory probe angle and effective projection angle, and an analysis of z -resolution. Section 3.2 then presents a simple laboratory demonstration of FDSC, in which the phase streak of a ~ 100 fs, megawatt-peak-power laser pulse propagating for ~ 10 ps through a glass Kerr medium several millimeters thick is recovered and analyzed in the light of prior knowledge of nonlinear pulse propagation in Kerr media. Chapter 4 will then present a more challenging laboratory application of FDSC to laser wakefield acceleration in the bubble regime.

3.1 The oblique-angle pump-probe geometry

As described in the previous chapter, FDI [30] and FDH [5] average over the evolution of a light-speed index structure because they use a collinear pump-probe geometry (see Fig. 3.1a). To overcome this limit, the FDSC uses an “oblique angle” pump-probe geometry, as shown in Fig. 3.1b. As in FDH, a temporally-advanced chirped reference pulse co-propagates ahead of the probe, without experiencing the pump-induced index alteration.

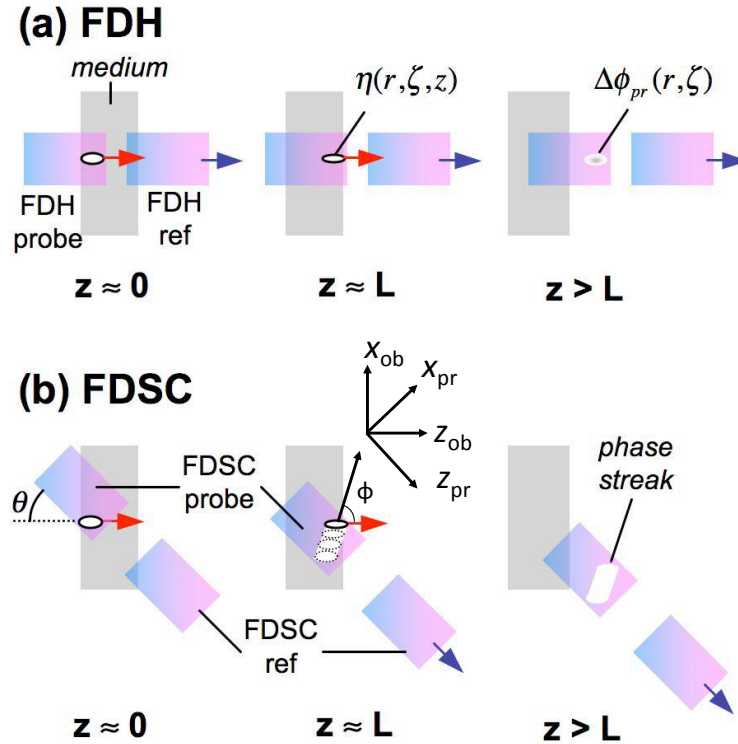


Figure 3.1: Schematic probe-reference (P-R) pulse configurations for **a.** frequency-domain holography (FDH) and **b.** frequency-domain streak camera (FDSC) at probing angles $\theta < 90^\circ$.

3.1.1 Frequency–domain streak cameras (FDSC): a time sequence of the index structure’s projections

In the FDSC, as the probe-reference (P-R) pair propagates at laboratory angle θ to the pump (see Fig. 3.1b), the pump-generated object imprints a phase shift “streak” that records information about the object’s z -evolution. The axis of the streak makes an angle ϕ — hereafter the “projection” angle — with the pump propagation direction. For example, in the geometry of Fig. 3.1b, as the P-R pair crosses the pump path at $\theta \sim 30^\circ$, the object sweeps along a streak axis that makes angle $\phi \sim 100^\circ$ with the propagation direction of the pump and its index structure $\Delta n(\zeta_{ob}, x_{ob}, y_{ob}, z_{ob})$. The quantitative relation between θ and ϕ depends on the velocities v_{ob} and v_{pr} of object and probe, as will be discussed later. If we imagine a single arbitrary line-out perpendicular to the streak axis, the phase shift that accumulates along this line as the index structure passes through it is proportional to the object’s projection $\psi(\zeta_{ob}) \propto \int \Delta n(\zeta_{ob}, x_{ob}, y_0, z_{ob}) d\xi_{ob}$, where $d\xi_{ob}$ denotes an infinitesimal path element along the streak axis. In general, ξ_{ob} is a linear combination of x_{ob} and z_{ob} . Here the transverse position y_0 is selected by the spectrometer slit, and the propagation distance z_{ob} is determined by where the transverse line-out is taken. In a single-shot measurement of the phase streak, a series of such transverse line-outs can be taken at different positions along the streak axis, corresponding to different propagation positions z_{ob} , thus providing a time (or z_{ob}) sequence of the index structure’s projections. By varying θ , or using additional probes propagating at different θ , projections of the index structure

from different directions are obtained. Configurations (such as Fig. 3.1b) for which $\phi \sim 90^\circ$ yield a sequence of *transverse* projections of the object's *longitudinal* profile — *i.e.* $\psi(\zeta_{ob}) \propto \int \Delta n(\zeta_{ob}, x_{ob}, y_0, z_{ob}) dx_{ob}$. Conversely, configurations for which $\phi \sim 0^\circ$ yield a sequence of *longitudinal* projections of the object's *transverse* profile — *i.e.* $\psi(x_{ob}) \propto \int \Delta n(\zeta_{ob}, x_{ob}, y_0, z_0) d\zeta_{ob}$.

Formally, the phase streak $\psi^{(\theta)}(\zeta_{pr}, x_{pr}, y_{pr})$ that an evolving pump-generated object $\Delta n(\zeta_{ob}, x_{ob}, y_{ob}, z_{ob})$ imprints on a probe pulse of center wavelength λ_{pr} that it crosses at laboratory angle θ can be expressed as an integral

$$\psi^{(\theta)}(\zeta_{pr}, x_{pr}, y_{pr}) = \frac{2\pi}{\lambda_{pr}} \int_0^L \Delta n^{(\theta)}(\zeta_{ob}, x_{ob}, y_{ob}, z_{ob}) dz_{pr}, \quad (3.1)$$

where the index object Δn is expressed in the coordinates of the probe (pr) co-moving frame. In writing Eq. (3.1), we have assumed that the effective propagation length L_{eff} over which any region of the probe profile overlaps the object is shorter than a probe diffraction length $L_{\text{diff}}^{(\text{pr})} = \pi(\Delta x_{ob}^2 + \Delta y_{ob}^2)/\lambda_{pr}n(\lambda_{pr})$, which is valid for the experiments presented in this and the next two chapters. Here $\Delta x_{ob}, \Delta y_{ob}$ are the object's transverse radii, and L_{eff} is less than the medium length L because the object drifts across the probe as they propagate at different angles and/or velocities. In this limit, a point of the probe pulse accumulates phase shift only when a linear chord of the object sweeps through it. Eq. (3.1) is a 4D generalization of the Radon transform widely used in conventional tomography [34]. If the path length L is long enough that diffraction is important, then Eq. (3.1) could be replaced with a Fresnel diffraction integral. Alternatively, the phase streak can be imaged from mul-

multiple object planes along the streak axis that are separated by a distance less than $L_{diff}^{(pr)}$. This last approach will be discussed in Chapter 6.

To use Eq. (3.1), $\Delta n(\zeta_{ob}, x_{ob}, y_{ob}, z_{ob})$ must be transformed from the coordinates of its own co-moving frame to those of the probe frame. The first step is to define stationary lab frame coordinates (t, x'_i, y'_i, z'_i) , where $i = (ob, pr)$ and the z'_i axis is parallel to the propagation direction of the object or probe pulse. For pulses propagating in the x - z plane, these coordinates are related by: $z'_{ob} = z'_{pr} \cos \theta + x'_{pr} \sin \theta$ and $x'_{ob} = -z'_{pr} \sin \theta + x'_{pr} \cos \theta$. We then apply canonical transformations $(\zeta_i, x_i, y_i, z_i) = (t - z'_i/v_i, x'_i, y'_i, z'_i)$ between lab and pump/probe co-moving frames, where v_i is the velocity of the object or probe pulse, to obtain

$$\begin{cases} v_{ob}\zeta_{ob} = v_{pr}\zeta_{pr} \cos \theta - x_{pr} \sin \theta + (v_{ob} - v_{pr} \cos \theta) t \\ x_{ob} = v_{pr}\zeta_{pr} \sin \theta + x_{pr} \cos \theta - v_{pr}t \sin \theta \\ y_{ob} = y_{pr}, \end{cases} \quad (3.2)$$

and the inverse relations

$$\begin{cases} v_{pr}\zeta_{pr} = v_{ob}\zeta_{ob} \cos \theta + x_{ob} \sin \theta + (v_{pr} - v_{ob} \cos \theta) t \\ x_{pr} = -v_{ob}\zeta_{ob} \sin \theta + x_{ob} \cos \theta + v_{ob}t \sin \theta \\ y_{pr} = y_{ob}. \end{cases} \quad (3.3)$$

Eq. (3.3) immediately replaces the arguments of the integrand in Eq. (3.1) which becomes:

$$\begin{aligned} \psi^{(\theta)}(\zeta_{pr}, x_{pr}, y_{pr}) &= \frac{2\pi}{\lambda_{pr}} \frac{v_{pr}}{v_{ob}} \int_0^L \Delta n [(v_{pr}/v_{ob})\zeta_{pr} \cos \theta - x_{pr} \sin \theta / v_{ob} \\ &- (1 - v_{pr} \cos \theta / v_{ob})(z_{ob}/v_{ob}), v_{pr}\zeta_{pr} \sin \theta + x_{pr} \cos \theta - (v_{pr}/v_{ob})z_{ob} \sin \theta, \\ &y_{pr}, z_{ob}] dz_{ob}. \end{aligned} \quad (3.4)$$

The phase streak (3.4) represents a projection of the index object in 4D space $(\zeta_{ob}, x_{ob}, y_{ob}, z_{ob})$ onto the 3D probe profile space $(\zeta_{pr}, x_{pr}, y_{pr})$.

3.1.2 Lab probe angle and effective projection angle

For stationary objects, the projection view angle is simply the laboratory angle θ at which probe light intersects the object. In the FDSC, the projection angle $\phi(\theta)$ (defined in the previous sub-section and in Fig. 3.1b) differs from, but depends on, θ . To derive the relation between ϕ and θ , define the starting point of the streak axis as the common origin of $\zeta_{\text{pr}} - x_{\text{pr}}$ and $\zeta_{\text{ob}} - x_{\text{ob}}$ coordinate systems at $t = 0$. The former origin moves to $(v_{\text{ob}}\zeta_{\text{ob}}, x_{\text{ob}})$ in the latter system at $t > 0$, thereby defining the streak axis. Once the phase-modulated probe propagates into free space, where it is detected, these coordinates become $(c\zeta_{\text{ob}}, x_{\text{ob}})$, yielding

$$\phi = \arg[c\zeta_{\text{ob}} + ix_{\text{ob}}], \quad (3.5)$$

which becomes

$$\phi = \arg [(v_{\text{ob}} - v_{\text{pr}} \cos \theta) + i(v_{\text{pr}}v_{\text{ob}}/c) \sin \theta], \quad (3.6)$$

upon substituting Eqs. (3.2) with $\zeta_{\text{pr}} = 0$ and $x_{\text{pr}} = 0$. Here the argument in brackets is a complex number of the form $x + iy$ corresponding to angle $\phi = \tan^{-1}(y/x)$ with the real axis. Fig. 3.2 plots θ vs. ϕ for two different pairs of $(v_{\text{pr}}, v_{\text{ob}})$ values. Both examples illustrate an important general feature of FDSC: a relatively narrow range of θ , which is convenient for laboratory set-up, can yield a broad range of ϕ , which is important for visualizing an object's evolving shape comprehensively. In Chapter 5, we shall see that this feature is important for assembling multiple projections tomographically to generate a single-shot “movie” of an evolving light-speed object. For $v_{\text{ob}} = 0.68c$ and

$v_{\text{pr}} = 0.66c$, typical of the experiment with an 800 nm pump and 400 nm probe in glass discussed later in this chapter, Eq. (3.6) yields projection angle range $-70^\circ < \phi < 70^\circ$ for $-12^\circ < \theta < 12^\circ$ (see Fig. 3.2, blue curve). For $v_{\text{ob}} \approx \sqrt{1 - n/n_c} = 0.99c$ (see Eq. (1.4)) and $v_{\text{pr}} \approx c$, typical of the LWFA experiment with plasma density $n_e \sim 3.5 \times 10^{19} \text{ cm}^{-3}$ described in Chapter 4, a larger projection range $-90^\circ < \phi < 90^\circ$ can be obtained with $-6^\circ < \theta < 6^\circ$ (see Fig. 3.2, red curve). Moreover, the comparison between the glass and LWFA cases showed that FDSC experiments with $v_{\text{ob}} < v_{\text{pr}}$ can cover a broader range of projection angles than that with $v_{\text{ob}} > v_{\text{pr}}$.

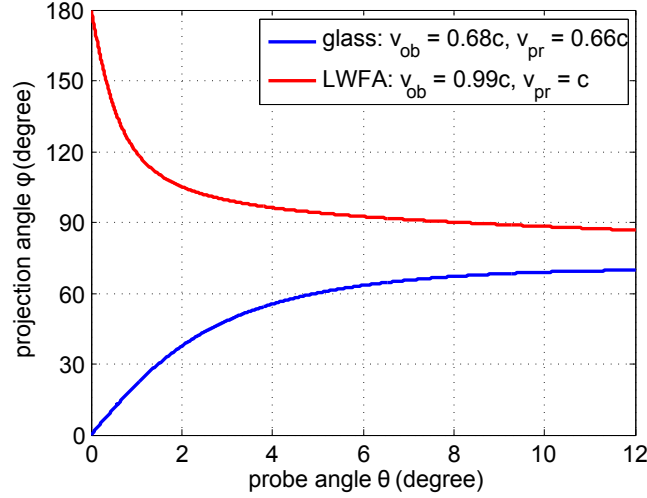


Figure 3.2: Projection angle ϕ vs. probe angle θ . **Blue.** FDSC with 800 nm pump and 400 nm probe in fused silica, *i.e.* $v_{\text{pr}} = 0.66c$ and $v_{\text{ob}} = 0.68c$. **Red.** FDSC with 800 nm pump and 400 nm probe in $3.5 \times 10^{19} \text{ cm}^{-3}$ plasma where electrons are effectively accelerated, *i.e.* $v_{\text{pr}} = c$ and $v_{\text{ob}} = 0.99c$.

Eq. 3.6 shows how the special projection angles $\phi \sim 0$ or π and $\phi \sim \pi/2$ discussed in Sec. 3.1.1 are obtained. A phase streak with $\phi = 0$ is obtained

with $\theta = 0$ (co-propagating object and probe) and $v_{\text{ob}} > v_{\text{pr}}$ (equivalently, $\phi = \pi$ corresponds to $\theta = 0$, $v_{\text{ob}} < v_{\text{pr}}$). Streaks at $\phi \sim 0$ (or π) are valuable because they reveal evolution of the transverse (x_{ob}) profile of the object as it drifts longitudinally along the probe profile. In contrast to FDH where velocity walk-off between co-propagating object and probe is a disadvantage because it blurs the image, in the FDSC (and later in FDT, see Chapter 5) it becomes an advantage because it creates a phase streak at $\phi = 0$ that is formally equivalent to streaks created by angular walk-off. Streaks at $\phi \sim \pi/2$ reveal evolution of the longitudinal (ζ) profile of the object as it drifts sideways across the probe profile.

3.1.3 z -resolution of frequency–domain streak cameras

FDSC is capable of fully resolving objects that satisfy the paraxial approximation – *i.e.* the drive pulse and its index object evolve slowly over distances z_{ob} of the order of the object’s dimensions. However, more rapid z_{ob} evolution is observed with limited resolution. This z -resolution depends on the length of the phase streak relative to the object’s dimensions. FDSC can resolve $\sim N$ stages of the object’s z_{ob} evolution, where N is the number of separated objects of dimensions $(\Delta\zeta_{\text{ob}}, \Delta x_{\text{ob}})$ that can be lined up along the streak axis. Similar to the derivation of projection angles, the starting and end points of the streak axis have coordinates $(0, 0)$ and $(c\zeta_{\text{pr}}, x_{\text{pr}})$, respectively, in $\zeta_{\text{pr}} - x_{\text{pr}}$ coordinates. The components of the streak length vector are thus $c\Delta\zeta_{\text{pr}} = c\zeta_{\text{pr}}$

and $\Delta x_{\text{pr}} = x_{\text{pr}}$, yielding

$$\begin{aligned}\Delta\zeta_{\text{pr}} &= L(1/v_{\text{ob}} - \cos\theta/v_{\text{pr}}), \\ \Delta x_{\text{pr}} &= L \sin\theta\end{aligned}\tag{3.7}$$

upon substituting Eqs. (3.3) with $\zeta_{\text{ob}} = 0$ and $x_{\text{ob}} = 0$ for a medium of length $L = v_{\text{ob}}t$. The length of a phase streak at probe angle θ is then $\sqrt{c^2(\Delta\zeta_{\text{pr}})^2 + (\Delta x_{\text{pr}})^2}$. Thus transverse profile evolution, measured using small θ probes, is best resolved when $\Delta\zeta_{\text{pr}} \gg \Delta\zeta_{\text{ob}}$. Since $\Delta\zeta_{\text{pr}} \propto |v_{\text{pr}} - v_{\text{ob}}|$ at small θ , using pump and probe pulses with a large velocity mismatch optimizes transverse z_{ob} resolution. Longitudinal profile evolution, measured using large θ probes, is best resolved when $\Delta x_{\text{pr}} \gg \Delta x_{\text{ob}}$. Since $\Delta x_{\text{pr}} \propto \sin\theta$, using probes near $\theta(\phi \approx \pi/2)$ optimizes longitudinal z_{ob} resolution. As a numerical example relevant to the experiments described in the next section, for which $v_{\text{ob}} = 0.68c$, $v_{\text{pr}} = 0.66c$, $\Delta\zeta_{\text{ob}} = 100$ fs, $\Delta x_{\text{ob}} = 50\mu\text{m}$ and $\theta_{\text{max}} = \theta(\phi = 70^\circ) = 14^\circ$ the z_{ob} -resolution is $\delta z_{\text{ob}}^{(\text{t})} \sim v_{\text{ob}}v_{\text{pr}}\Delta\zeta_{\text{ob}}/|v_{\text{ob}} - v_{\text{pr}}| = 670 \mu\text{m}$ and $\delta z_{\text{ob}}^{(\text{l})} \sim \Delta x_{\text{ob}}/\sin\theta_{\text{max}} = 210 \mu\text{m}$ for transverse (t) and longitudinal (l) profile evolution, respectively.

3.2 Example: FDSC of nonlinear refractive index during megawatt laser propagation in glass

As a proof of concept, we demonstrated the FDSC technique by conducting an experiment to visualize the nonlinear propagation of a femtosecond laser pulse in glass [49]. The evolving refractive index structure is created by

focusing a pump pulse (wavelength $\lambda_{pu} = 800$ nm, bandwidth $\Delta\lambda = 30$ nm FWHM, energy 0.15 - 6 μJ) of 600 fs duration inside a fused silica plate of thickness $L = 3$ mm. The pump induces refractive index $\eta(r, \zeta, z) = n_2 I(r, \zeta, z)$, where $n_2 \sim 3 \times 10^{-16} \text{cm}^2/\text{W}$ is the nonlinear index of glass [69], and $I(r, \zeta, z)$ is the pump intensity profile. Thus $\eta(r, \zeta, z)$ evolves as the pump pulse diffracts, self-focuses, etc. Two linearly chirped, 1 ps, second harmonic ($\lambda_{pr} = 400$ nm) pulse pairs P1-R1 and P2-R2 probed $\eta(r, \zeta, z)$ simultaneously at $\theta = 0^\circ$ (FDH) and 14° (FDSC), respectively. At 14° , the streak sweeps nearly transversely across the probe profile.

The two P-R pairs, each with separation $\Delta t_{PR} = 3.3$ ps, were imaged from the sample exit plane ($z = L$) to the entrance slit of a single spectrometer. The first pair (P1-R1) was imaged with magnification 12 in order to resolve the micron-size nonlinear index envelope of the pump pulse. The second pair (P2-R2) was imaged with magnification 2.3 to fit the entire millimeter-long streak on the detector. A 50/50 beam splitter behind the imaging lenses combined P1-R1 and P2-R2 into parallel beams that were imaged to spatially offset locations along the slit, the length of which limited us to two probe-reference pairs. Hereafter we refer to the procedure of imaging two (or more) P-R pairs to different image locations along the slit of a single spectrometer as “spatial multiplexing”. Multiplexing is important because spectrometers are expensive; thus it is desirable to process all data with one spectrometer.

Figure 3.3 shows reconstructed images from the spatially multiplexed FDH (top row) and FDSC (2nd row) probes, and the spectrum (3rd row)

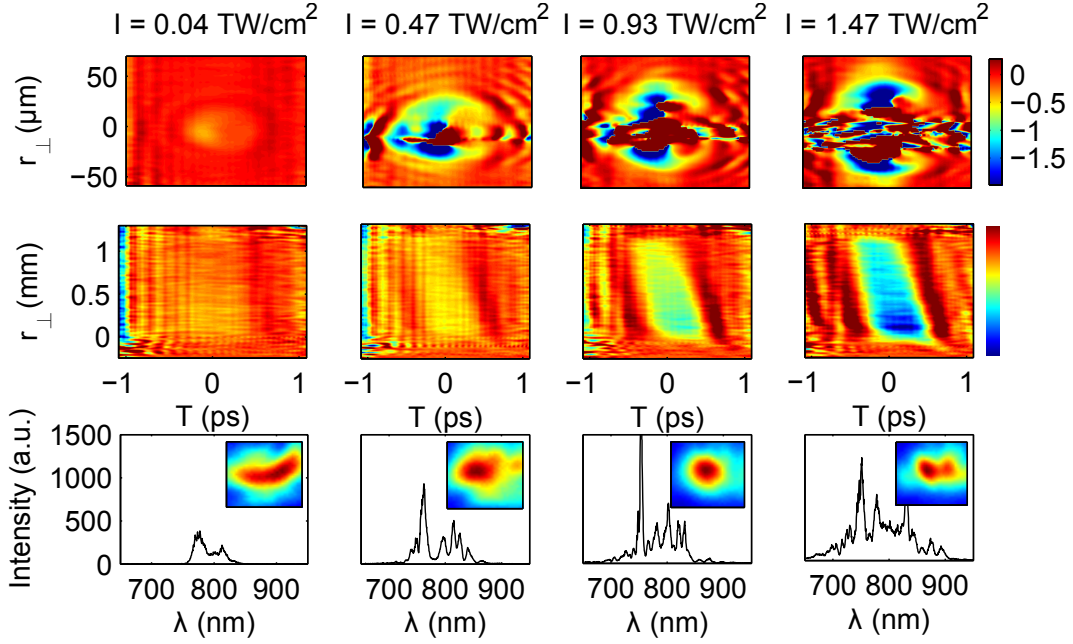


Figure 3.3: Spatially multiplexed frequency-domain streak camera (FDSC). Phase shifts on: 0° probe (top row), showing $\Delta\phi_{pr}(r, \zeta)$ integrated over z , as conventional frequency-domain holography (FDH); 14° probe (middle row), showing streaks. r_\perp denotes transverse position of the probe pulse at the interaction region. Bottom row: transmitted pump spectrum and spatial profile (inset), for initial pump intensity (left to right) $I = 0.04, 0.47, 0.93,$ and 1.47 TW/cm^2 .

and spatial profile (3rd row inset) of the pump at $z = L$, as initial peak I of the pump (focused here to spot radius $w_0 \sim 20 \mu\text{m}$ at $z = 0$) increased from 0.04 (left) to 1.5 (right) TW/cm^2 . In the upper end of this intensity range, $n_2 I L > \lambda_{pu}$, so pump propagation becomes nonlinear. The FDH images show $\Delta\phi_{pr}(r, \zeta, L)$ integrated over z . Indirect signs of evolution are evident. For example at larger I , $\Delta\phi_{pr}$ exceeds 2π near $r_\perp = 0$ (creating complicated phase wrapping artifacts), indicating that self-focusing occurred. Moreover,

the longitudinal extent (~ 1 ps) of the index “bubble” exceeds the pump pulse duration (~ 600 fs) measured from a transverse line-out of the FDSC streak. This is explained by group velocity walk-off between 800 nm pump and 400 nm probe, which elongates the $\Delta\phi_{pr}$ profile into a longitudinal phase streak even in the FDH line. These complications in interpreting FDH data underscore the importance of FDSC.

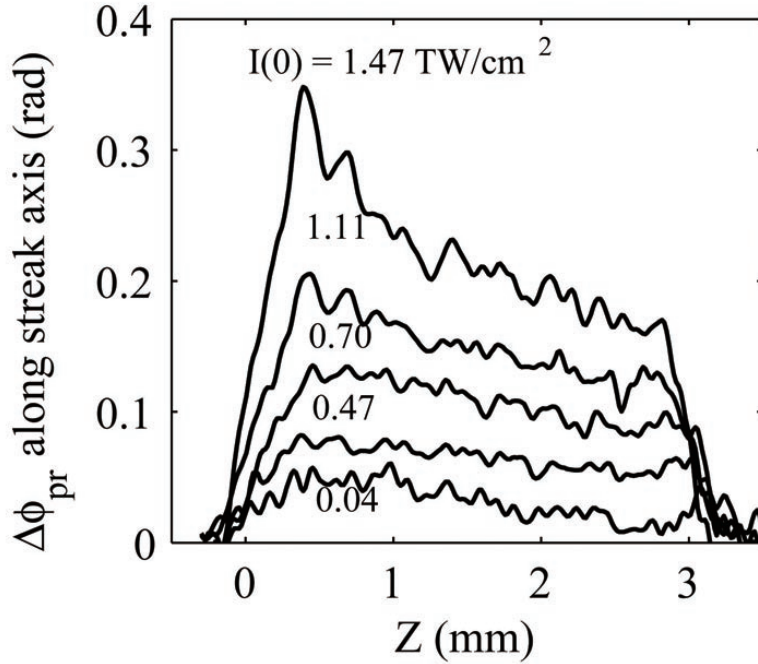


Figure 3.4: Measured $\Delta\phi_{pr}$ line-outs along streak axis as shown in Fig. 3.3, showing evolution of peak index shift.

The FDSC images (Fig.3.3, middle row) show phase streaks that increase in amplitude with I . Line-outs along the streak axis, plotted in Fig.3.4, reveal I -dependent evolution of the axial phase shift. To help interpret this

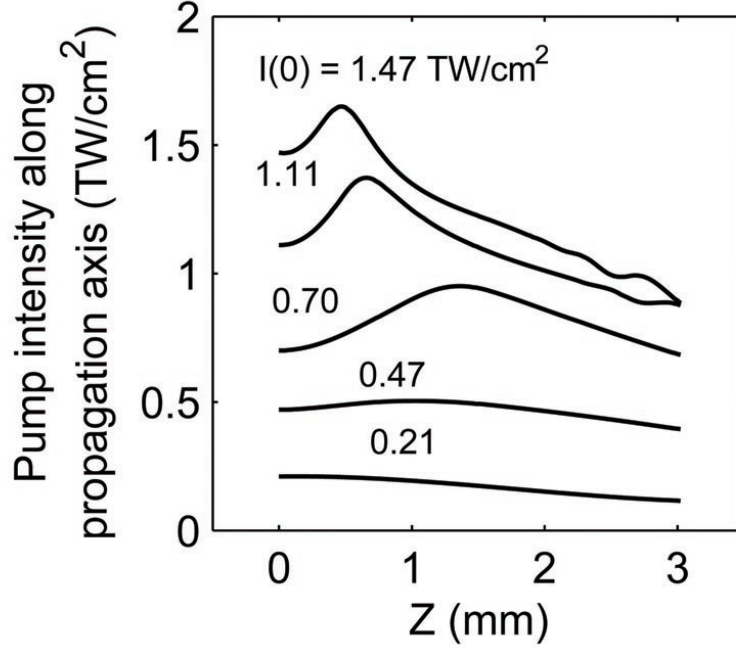


Figure 3.5: Calculated pump intensity evolution $I(z)$ from NLSE, which is proportional to $\Delta\phi_{pr}$ line-outs.

evolution, we modeled propagation of Gaussian pump pulses using the Non-linear Schrödinger Equation (NLSE, see Eq. (1.1)), including multi-photon absorption (MPA) and plasma formation [26]. Fig. 3.5 shows the calculated peak $I(z)$ for various initial I . For $I = 0.04$ TW/cm², nonlinearities are negligible, $I(z)$ decreases monotonically by linear diffraction over Rayleigh range $z_R = \pi n_0 w_0^2 / \lambda_{pu} \approx L$, and the transmitted pump spectrum is barely perturbed from the incident spectrum (Fig. 3.3, 3rd row, left). For $I = 0.47$ TW/cm², peak pump power (3 MW) reaches critical power $P_{cr} = \pi(0.61)^2 \lambda_{pu}^2 / 8n_0 n_2 = 2.15$ MW, and the pump propagates with nearly constant intensity as self-

focusing and diffraction balance with MPA still weak. Simultaneously, the pump spectrum broadens to $\Delta\lambda \sim 50$ nm (Fig. 3.3, 3rd row, 2nd panel), a signature of self-phase modulation. As I increases further ($I = 0.70$ to 1.47 TW/cm²), NLSE calculations show: (i) pump self-focusing moves the point of maximum I closer and closer to the glass entrance (see Fig. 3.5); (ii) the subsequent monotonic decrease of I is caused primarily by direct MPA; (iii) the pump converges to a nearly I -independent transverse profile (FWHM $16 \mu\text{m}$) that agrees well with measured exit profiles (Fig. 3.3, 3rd row, insets of last two panels). Meanwhile the pump spectrum further broadens (Fig. 3.3, 3rd row, last 2 panels). The transverse FWHM of FDH phase profiles (Fig. 3.3, top row, last 2 panels) agree well with exit pump profiles and NLSE calculations (their apparent broadening with increasing I results from increased visibility of the wings as total $\Delta\phi_{pr}$ increases). Self-focusing accounts for large $\Delta\phi_{pr}$ near the center of the FDH images at high I . The example illustrates how combining FDH and FDSC improves accuracy of interpretation.

In summary, here FDSC and FDH were combined to observe evolution and longitudinally-averaged structure of a microscopic light-speed object in one shot. This prototype experiment demonstrated the feasibility of visualizing the evolution of laser-induced index structure for a broad range of transparent media. For example, LWFAs driven by terawatt laser pulses in $\sim 10^{19}$ cm⁻³ plasma over several millimeters exhibit interesting plasma structure dynamics. FDSC is promising for observing the generation and evolution of plasma “bubbles” that accelerate electrons to relativistic energy. Details

will be discussed in Chapter 4.

Another research track beyond FDSC is to apply *multiple* probe laser pulses simultaneously at different angles. Time sequences of projections of the index structure at different θ , ϕ can potentially be converted into a “movie” using a tomographic reconstruction algorithms, leading to full spatiotemporal visualization of the index structure at different propagation distance z . However, the technical implementation is challenging since multiple probes have to be generated, then detected with a single spectrometer in a single shot. In addition, conventional tomography reconstruction algorithms must be modified and generalized to reconstruct a “movie” of a light-velocity index object from a group of phase streaks. Detailed solutions to these issues led us to develop a technique called frequency-domain tomography (FDT) [51], which will be discussed in Chapter 5.

Chapter 4

Single-shot visualization of evolving laser wakefields by frequency domain streak camera

As discussed in Sec. 1.2, the development of laser wakefield accelerators (LWFAs) has led to tabletop sources of collimated, femtosecond duration, quasi-monoenergetic electron bunches up to GeV energy that can generate bright coherent x-rays for applications in biology, materials science and medicine. The small size and luminal velocity of LWFAs, however, makes observation and control of their evolving structure — the main determinant of LWFA performance [38] — exceptionally challenging. Consequently, LWFA science has relied on intensive computer simulations with estimated initial conditions for visualizing the dynamic microstructure of laser-driven plasma waves. Nevertheless direct laboratory visualization is essential when initial conditions are imprecisely known, as they usually are. This is particularly true for the highest-performing LWFAs, which operate in the strongly nonlinear “bubble” regime, that favors efficient injection of surrounding plasma electrons and quasi-monoenergetic acceleration. As mentioned in previous chapters, Matlis *et al.* used frequency-domain holography (FDH) to record snapshots of laser wakes in a quasi-linear regime, in which the plasma wave evolved negligibly [57]. FDH snapshots in the nonlinear bubble regime yielded

so-called “optical bullets” in the reconstructed probe amplitude profile that were related to bubble formation, and effectively characterized its size and shape near the end of the interaction region. However, they averaged over key bubble dynamics that underlie LWFA physics [18]. *Dynamic* nonlinear wakes have been visualized only by probing them transversely at different time delays over *multiple* shots [9]. However, this method requires extremely short (6 fs) probe pulses, and is impractical for LWFA experiments with longer pulses, shot-to-shot variations, or low repetition rates.

In this chapter, we describe single-shot diagnosis of evolving laser-driven plasma bubbles using an optical frequency-domain streak camera (FDSC), the principle and prototype demonstration of which was discussed in the previous chapter. In Section 4.1, a terawatt-laser-driven wakefield accelerator yielding ~ 100 MeV monoenergetic electrons, and the set-up of the FDSC for LWFA diagnosis, are described. In Section 4.2, FDSC observations of bubble dynamics for various experimental conditions are presented. They reveal bubble formation, propagation and lengthening that is correlated with electron acceleration. In Section 4.3, we compare the bubble dynamics measured by FDSC with the results of first-principles particle-in-cell (PIC) simulations. The results show that the point at which a bubble forms, and the distance it propagates before coalescing with later plasma wave “buckets”, depend sensitively on n_e , and in turn dictate electron energy and beam quality.

4.1 Experimental setup and results

4.1.1 Terawatt-laser-driven wakefield accelerator

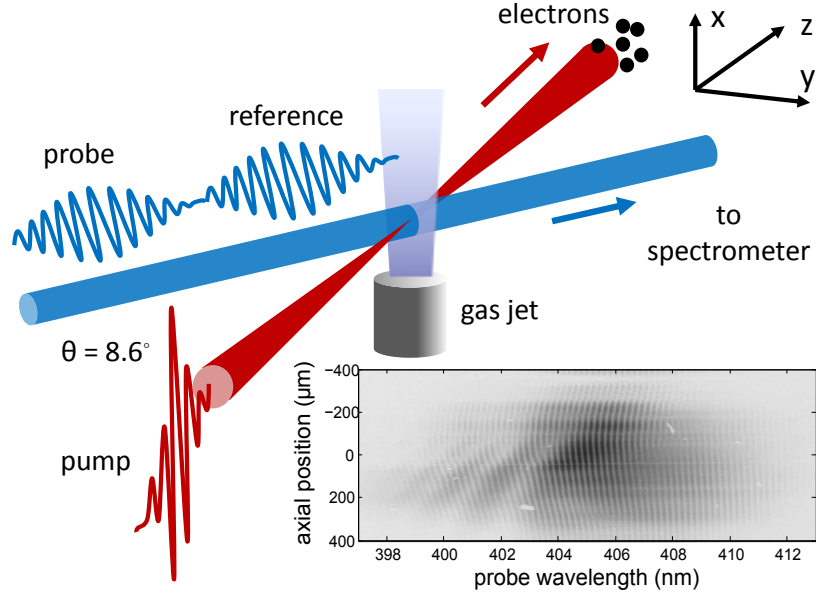


Figure 4.1: Schematic experimental setup of frequency-domain streak camera (FDSC) for laser wake field accelerators. The inset plot is a typical frequency-domain hologram taken from the CCD camera detector of the spectrometer.

The experimental setup for the LWFA and FDSC is shown in Fig. 4.1. To generate plasma wakes, 800 nm, ~ 30 fs, ~ 0.8 J linearly polarized laser pulses from a 30 TW chirped-pulse amplification (CPA) Ti: sapphire laser system manufactured by Thales Laser were focused by an off-axis parabolic mirror with f -number 12 to spot radius is $\sim 10 \mu\text{m}$ and normalized laser vector potential $a_0 = eA/m_e c^2 \approx 1.5$ at the entrance of a supersonic helium gas jet of thickness $L = 3$ mm. A transverse interferometer (not shown) determined the laser-ionized plasma density profile $\bar{n}_e(r, z)$ on each shot, averaged over

plasma oscillations. The density profile was reconstructed from the phase shift using Abel-inversion, assuming that the laser ionized plasma channel is cylindrically symmetric. A magnetic electron spectrometer downstream from the gas jet (also not shown) measured the electron energy spectrum. Energy-dispersed electrons were detected by imaging the fluorescence they induced on a scintillating (KODAK Lanex) screen onto a charge coupled device (CCD) camera. When the plasma density was optimized at $2.0 \times 10^{19} \text{ cm}^{-3}$, quasi-monoenergetic electron beams with $\sim 100 \text{ MeV}$ energy, $\sim 100 \text{ pC}$ charge, and only 4 mrad divergence were generated.

The experimental conditions for electron acceleration were scanned over a broad range of parameters including plasma density, focal spot position, and pump laser pulse duration in order to optimize the electron beam quality globally [85]. Pump pulse duration was adjusted by varying the grating separation of the compressor of our CPA system and measured by a single-shot autocorrelator. Optimal electron beam quality is achieved with the shortest achievable pump duration ($\sim 30 \text{ fs}$) for two reasons: (i) plasma “bubbles” are excited most efficiently at maximum intensity, which is achieved with the shortest pulse duration; (ii) at $\bar{n}_e \sim 10^{19} \text{ cm}^{-3}$, the plasma period $\sqrt{\pi m_e / n_e e^2} \sim 35 \text{ fs}$, so pump pulses compressed to $\sim 30 \text{ fs}$ excite laser wakefields resonantly. Another significant control parameter for electron quality is the position of the pump laser focal plane. Though the vacuum Rayleigh range of the pump pulse ($2\pi w_0^2 / \lambda \approx 0.8 \text{ mm}$) is much smaller than the 3-mm gas jet length, the pump pulse self-focuses in the plasma, enhancing its intensity until it blows

out a “bubble”. The bubble then acts as a waveguide that maintains pump laser pulse intensity over roughly the last half of the whole 3-mm propagation distance, thus optimizing electron acceleration. This process works best when the pump is focused at the gas jet entrance.

Accelerated electron energy and beam quality also depend strongly on the ambient plasma density \bar{n}_e , but the mechanism underlying this dependence is subtle, and requires the FDSC results and analysis of this chapter for its full explication. Plasma density is adjusted by changing the backing pressure of the helium gas jet from 60 psi to 80 psi, corresponding to plasma density from $1.3 \times 10^{19} \text{ cm}^{-3}$ to $2.2 \times 10^{19} \text{ cm}^{-3}$, as measured by transverse interferometry. As discussed in reference [85], for the pump laser conditions described above, accelerated electrons are observed only within this narrow density range. Optimal monoenergetic electron beams centered at 100 MeV are achieved at $\bar{n}_e = 2.0 \pm 0.1 \times 10^{19} \text{ cm}^{-3}$. At lower or higher densities, at best electrons with a broad energy spread (40 MeV – 70 MeV) are observed, and at worst no electrons are produced. In addition, electron beam quality — beam divergence, pointing stability, reproducibility — degrades significantly at those sub-optimal plasma density regimes. The underlying physics, as revealed by FDSC results, is discussed further below.

4.1.2 The probe pulse for frequency-domain streak camera

To record phase streaks, a chirped ($\text{GDD} \approx 2.7 \times 10^3 \text{ fs}^2$) collimated probe-reference (P-R) pulse pair (center wavelength $\lambda_{pr} = 400 \text{ nm}$, bandwidth

$\Delta\lambda_{pr} \sim 10$ nm, duration ~ 500 fs, beam radius 1 mm) split from the drive pulse, then frequency-doubled to facilitate discrimination of probe light from scattered, frequency-broadened pump light [67], propagated at oblique angle $\theta = 8.6^\circ$ across the pump laser path through the gas jet (Fig. 4.1). The reference preceded by ~ 2 ps, and the probe overlapped, the pump and its immediate wake. The P-R bandwidth and resolves longitudinal phase structure $\Delta\zeta$ as small as 30 fs. Chirping is accomplished entirely by the P-R transit through the vacuum chamber window and the dichroic mirror combining probe and pump beams, without an extra intentional dispersive medium, and the ~ 500 fs probe duration illuminates the ionization front in the leading edge of the pump and multiple periods of its plasma wake. The transverse beam size (~ 1 mm) is chosen to image the whole 3-mm propagation distance. The lab angle $\theta = 8.6^\circ$ was chosen to achieve projection angle $\phi \approx 90^\circ$ (see Eq. (3.6)), so that the plasma structures drifted across the probe profile at right angles to their propagation direction. The streak thus became a time sequence of transverse projections of the evolving longitudinal profiles of the plasma structures, the optimum geometry for observing bubble formation and lengthening. To record the phase streak, the P-R pair was imaged from the gas jet exit to the spectrometer entrance slit. Interference of the reference with the phase-modulated probe inside the spectrometer yielded a frequency-domain hologram, shown in Fig. 4.1, which a charge-coupled device (CCD) camera recorded. Fourier transformation of the hologram [57] reconstructed the probe phase shift map $\psi(t_{pr}, x_{pr})$, where t_{pr} denotes time delay in the probe co-moving frame, x_{pr}

transverse position in the probe profile. Since $\max(\psi)$ usually exceed 2π , a 2D phase unwrapping procedure based on the weighted minimum norm algorithm [31] was applied.

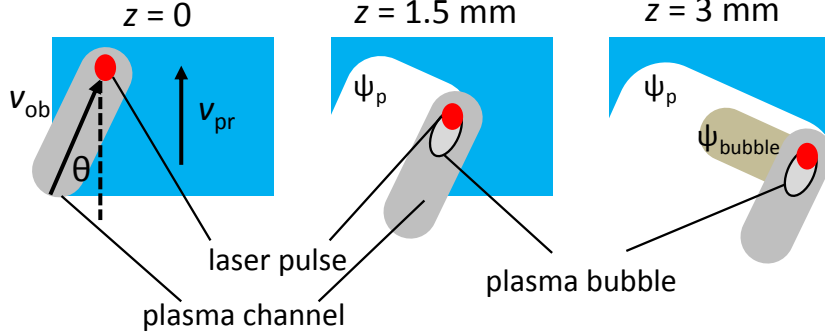


Figure 4.2: Schematic diagram of phase shift generation by laser plasma structures.

Figure 4.2 illustrates the process of phase streak formation on the probe spatiotemporal profile, induced by both plasma channel and laser wakefields. At the entrance of the gas jet ($z = 0$, left panel of Fig. 4.2), the pump laser pulse ionizes the helium gas and leaves a $d_{\text{channel}} \sim 200 \mu\text{m}$ thick photo-ionized plasma channel trailing the pump laser pulse. The plasma channel sweeps through the pump profile and contributes phase shift at the order of $\psi_p \simeq (2\pi/\lambda_{\text{pr}})(\bar{n}_e/4n_c)(d_{\text{channel}}/\sin\theta) = 15 \text{ rad}$, where probe wavelength $\lambda_{\text{pr}} = 0.4 \mu\text{m}$, critical density for 400 nm probe $n_c = 7.0 \times 10^{21} \text{ cm}^{-3}$, and plasma density $\bar{n}_e \sim 2 \times 10^{19} \text{ cm}^{-3}$. Small amplitude linear wakefield is exited, but contributes negligible phase shift measurement in the probe. As the laser pulse propagates inside the gas jet (*e.g.* $z = 1.5 \text{ mm}$, middle panel of Fig. 4.2), the pump pulse experience nonlinear relativistic self-focusing and plasma wave

induced self-focusing, thus the laser plasma acceleration enters the nonlinear “bubble” regime that laser field is enhanced to $a_0 \sim 10$. The plasma bubble with a dynamic width of $d_b \approx \lambda_p \sqrt{a_0} / \pi \sim 10$ starts to contribute to probe phase shift $\psi_{\text{bubble}} \simeq (2\pi/\lambda_{\text{pr}})(\bar{n}_e/4n_c)(d_b/\sin\theta) \approx 1$ rad. Unlike ψ_p that is from plasma refractive index smaller than 1, ψ_{bubble} comes from positively charged helium-ion filled blow-out bubble area with refractive index 1, thus it has an opposite sign to ψ_p . The net observable effect of these two phase shift components in FDSC measurements is an index dip representing ψ_{bubble} sitting on top of ionization front induced ψ_p , as shown in Fig. 4.2 right panel.

The projection angle ϕ is derived and introduced in Eq. (3.6). Here the probe pulse velocity is c and the pump-induced plasma structures propagating at $v_{\text{pu}} = 0.99c$, equal to pump pulse group velocity in $\bar{n}_e \sim 10^{19} \text{ cm}^{-3}$ plasma, the projection angle is $\phi = \arg[(v_{\text{pu}} - v_{\text{pr}} \cos\theta) + i(v_{\text{pu}}v_{\text{pr}}/c) \sin\theta] \approx 89.5^\circ$ — *i.e.* at right angle— to the pump propagation direction. Thus phase “streaks” represent a time sequence of the laser wakefields’ transversely accumulated projections. For laser wakefield in the nonlinear “bubble” regime, the bubble is stretched longitudinally for electron self-injection [38]. After sufficient electrons are injected, the beam loading effect [91] leads to the coalescence of the first and second buckets of plasma waves. Thus the oblique probe angle at $\theta = 8.6^\circ$ provides an optimum geometry to observe bubble formation and dynamics behind the pump pulse.

4.2 Analysis of plasma “bubble” induced phase streaks

Measured phase streaks are shown in Fig. 4.3. At low plasma density ($1.3 \times 10^{19} \text{ cm}^{-3}$, left panel), only the plasma channel contributed phase shift component is observed because the low amplitude plasma wakes in the linear regime contributes negligible phase shift. However at high density ($2.0 \times 10^{19} \text{ cm}^{-3}$, right panel), the plasma “bubble” induced phase shift ψ_{bubble} is observed since high plasma density enhances self-focusing of the pump laser pulse to a high intensity for nonlinear bubble excitation. Here the transverse size of the phase shift profile is around $450 \mu\text{m}$, consistent with the transversely shifted distance of the plasma channel $L \sin \theta = 448 \mu\text{m}$. The phase streaks show a significantly tilted edge because of the pump-probe group velocity walk-off and the oblique probe angle. As the pump induced index structure propagates at speed v_{pu} , its temporal position in the probe spatiotemporal profile moves backward as a function of propagation distance

$$\frac{dt_{\text{pr}}}{dz} = \frac{1}{v_{\text{pu}}} - \frac{\cos \theta}{v_{\text{pr}}}. \quad (4.1)$$

Meanwhile, the transverse motion direction within the probe profile is defined by $dx_{\text{pu}}/dz = \sin \theta$, the slope of the phase streak edge $dt_{\text{pu}}/dx_{\text{pu}}$ can be determined, which is critical to trace the trajectory of the pump pulse.

To determine the pump pulse trajectory, the initial position of the pump laser should be determined by the shape of the ionization channel induced phase shift profile. The tip point “A” in Fig. 4.3 left panel is featured with the earliest t_{pr} time delay, implying the initial position of the pump laser

center along x_{pr} direction since the highest pump intensity in the center ionizes plasma at the earliest time. Meanwhile, the second tip point “B” (Fig. 4.3 left panel) denotes the initial longitudinal position of pump pulse center assuming that the pump pulse front is not tilted. Thus combining the initial position of pulse pulse together with its moving direction based on calculated $dt_{\text{pu}}/dx_{\text{pu}}$, the pump pulse trajectories are determined for different plasma densities. Moreover, the phase shift dips are always just behind the driving pump pulse.

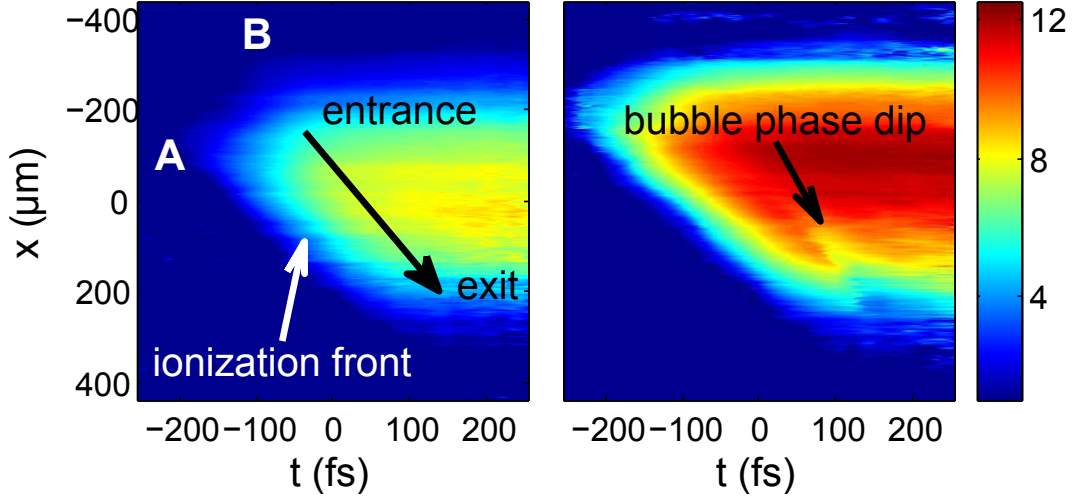


Figure 4.3: Reconstructed phase streak imprinted on the probe spatiotemporal profile ($t_{\text{pr}}-x_{\text{pr}}$). The phase shift shown in the left panel has only the plasma channel component ψ_{p} at plasma density $1.3 \times 10^{19} \text{ cm}^{-3}$, whereas the right panel shows a bubble induced phase dip at plasma density $2.0 \times 10^{19} \text{ cm}^{-3}$.

4.2.1 Plasma wakefield “bubble” evolution history under different density

Transverse line-outs of phase streak in Fig. 4.3 crossing the pump trajectories are taken to illustrate the bubble evolution history at different propagation distances. Thus the dip area, or ψ_{bubble} , at different propagation distance z are highlighted by taking line-outs from $\psi [t, x = (z - z_0) \sin \theta]$ where z_0 is the corresponding propagation distance for a line-out of the phase streak at $x = 0$. In Fig. 4.4, phase shift line-outs at $z = 1$ to 3 mm with 0.25 mm increment are taken (numbers on line-outs denote propagation distance z value in unit of millimeter) at density $1.3 \times 10^{19} \text{ cm}^{-3}$ (a), $1.7 \times 10^{19} \text{ cm}^{-3}$ (b), $2.0 \times 10^{19} \text{ cm}^{-3}$ (c), and $2.2 \times 10^{19} \text{ cm}^{-3}$ (d). For all cases, no dip is shown at $z < 1$ mm where the pump pulse slowly self-focused before efficient excitation of bubble. However when $z > 1$ mm, phase streaks at different plasma density (Fig. 4.4a-d) show different evolution dynamics regarding the dip.

Bubble induced phase shift dips are negligible for low plasma density at $\bar{n}_e \sim 1.3 \times 10^{19} \text{ cm}^{-3}$ (Fig. 4.4a). The pump laser pulse enters the gas jet with initial $a_0 \approx 1.5$ that is only able to drive laser wakefields in the linear regime. The density perturbation δn_e in the linear wakefield regime is small compare to the ambient plasma density \bar{n}_e , and contributes little phase shift imprinted onto the probe. The pump laser pulse also experiences relativistic self-focusing while propagating in plasma. However, the transverse refractive index difference linearly depends on the ambient plasma density, thus the distance of pump self-focusing is well beyond the length of gas jet

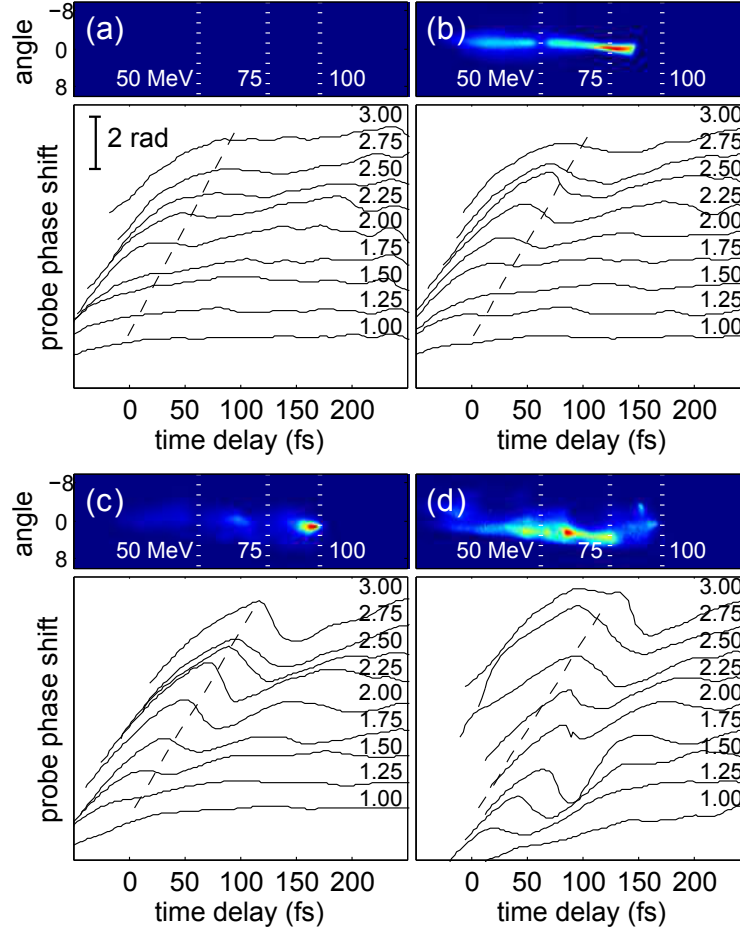


Figure 4.4: Angular-resolved electron spectrum and probe phase streak line-outs at propagation distances from $z = 1$ to 3 mm with 0.25 mm increment different plasma density: **(a)** $1.3 \times 10^{19} \text{ cm}^{-3}$; **(b)** $1.7 \times 10^{19} \text{ cm}^{-3}$; **(c)** $2.0 \times 10^{19} \text{ cm}^{-3}$; **(d)** $2.2 \times 10^{19} \text{ cm}^{-3}$. Numbers on each curve denotes the propagation distance z value in unit of millimeter. Dashed lines show the trajectory of the center of the pump pulse.

and no plasma bubble is formed. Correspondingly, no electron is trapped or accelerated in the linear wakefields.

An increase of plasma density to $\bar{n}_e \sim 1.7 \times 10^{19} \text{ cm}^{-3}$ enhances pump laser self-focusing as well as the laser intensity from $a_0 = 1.5$ to ~ 10 , enabling excitation of laser wakefields in the nonlinear bubble regime before leaving the gas jet (Fig. 4.4b). The phase dips start to emerge at $z = 2.5$ mm, where the bubble formation happens. From $z = 2.5$ to 3 mm, electrons are constantly injected into the bubble and get accelerated by the longitudinal electrical field. The maximum acceleration length is around 0.5 mm, smaller than the dephasing length $L_d = (2\lambda_p^3 \sqrt{a_0}) / (3\pi\lambda^2) \approx 0.6$ mm [53], yielding broad-band electron beams peaked at ~ 70 MeV.

Optimal electron acceleration is achieved at plasma density $\bar{n}_e \sim 2.0 \times 10^{19} \text{ cm}^{-3}$ (Fig. 4.4c). In this case, pump laser self-focusing becomes even stronger than the previous case and plasma bubble formation starts at $z \sim 2.0$ mm. After propagation for the dephasing length $L_d \approx 0.5$ mm, early injected fast electrons enter the front half of the bubble and de-accelerate, while lately injected slow electrons keep accelerating and catch up. This process happening after $z = 2.5$ mm is called phase space rotation [92] that directly compresses the electron distribution in momentum space and results in mono-energetic electron bunches peaked at the optimal energy ~ 100 MeV, as shown in Fig. 4.4c top row. Moreover, for $z \geq 2.5$ mm in Fig. 4.4c, the phase dips suddenly shift backwards to larger time delay t . As discussed later, this is a signature of bubble coalescence and longitudinal merging induced by beam

loading.

Finally the plasma density is further increased to $2.2 \times 10^{19} \text{ cm}^{-3}$ and degraded electron quality is obtained (Fig. 4.4d). A FDSC measured phase dip forms at around $z = 1.3 \text{ mm}$, implying bubble formation, electron injection and acceleration. When the laser propagates to $z = 1.75 \text{ mm}$, the shifted phase dip is directly correlated to bubble coalescence and beam loading at this position. Thus after $z \sim 2 \text{ mm}$, electrons propagate in a merged bubble which is not able to efficiently provide acceleration field, and show low energy and broad spectrum consistent with independently measured result (Fig. 4.4d, top row).

4.2.2 Evolution z -resolution and longitudinal t -resolution

FDSC measured phase streaks $\psi(t, z)$ represent the projection of the bubble longitudinal profiles at different propagation z -positions, thus the limits of resolving fast evolution events (*i.e.* evolution z -resolution δz) and fine longitudinal structures (*i.e.* longitudinal t -resolution δt) should be determined. For the evolution z -resolution, the two phase shift components from plasma bubble and laser wakefields are different. The plasma channel $d_{\text{channel}} \sim 200 \mu\text{m}$ is thick, so the $\Delta x \sim 500 \mu\text{m}$ long phase streak can resolve $N_{\text{channel}} = \Delta x / d_{\text{channel}} \leq 3$ frames of the evolution history, or $\delta z_{\text{channel}} = L / N_{\text{channel}} \geq 1 \text{ mm}$. However, the thickness of plasma bubble is smaller than $20 \mu\text{m}$, thus the number of independently resolvable evolution events is $N_{\text{bubble}} = \Delta x / d_{\text{bubble}} > 25$ and the z -resolution is $\delta z_{\text{bubble}} = L / N_{\text{bubble}} < 0.12$

mm. Given the experimental parameters, FDSC is sufficient to resolve dynamics of plasma bubble evolution during a propagation distance beyond 0.12 mm, and in Fig. 4.4, phase shift curves representing longitudinal profiles of the plasma bubble are lined-out every 0.25 mm which is $2\delta z_{\text{bubble}}$.

The other limit δt of resolving fine structures on the femtosecond longitudinal profile is denoted as longitudinal t -resolution, which is governed mainly by the probe bandwidth [40]. In our experiment, the bandwidth of probe $\Delta\lambda_{\text{pr}} \sim 10$ nm determined the optimal longitudinal resolution $\delta t \sim 0.44\lambda^2/c\Delta\lambda_{\text{pr}} \approx 30$ fs, which is comparable to the plasma wave period $2\pi/\omega_p \approx 30$ fs given the plasma density. It may be insufficient to resolve the fine longitudinal structures within a single plasma wave bucket whose, for example the high density, thin sheath layer between nonlinear plasma bubbles. However, the phase dips in Fig. 4.4 clearly reveal dynamics of bubble formation and coalescence, though they represent actual probe phase shift convolved with a 30-fs wide blurring function. The solution to further improve the longitudinal t -resolution is to broaden the probe pulse bandwidth to, for example, 100 nm based on super-continuum generation in gases or hollow fibers [40]. In this case, the longitudinal resolution is expected to be improved to as accurate as sub-10 fs. Meanwhile, the probe signal should be separated from pump induced plasma emission and scattering.

4.3 Simulations of laser wakefield excitation and electron acceleration

To verify the evolution dynamics of FDSC measured plasma bubble, a 30 fs Gaussian pump laser pulse with $a_0 = 1.2$ and $w_0 = 10 \mu\text{m}$ propagating in plasma with different density is simulated using 3D particle-in-cell code VLPL [65]. Similar to measured optimal electron beam and corresponding FDSC phase shift at a specific plasma density, simulations also found a optimal density at $\bar{n}_e = 1.5 \times 10^{19} \text{ cm}^{-3}$ that plasma bubble experienced dynamic evolution from $z = 1.6$ to 2.4 mm (Fig. 4.5a-c), and a quasi-mono-energetic electron spectral peak centered at 100 MeV was obtained (Fig. 4.5d). At $z = 1.6$ mm, plasma bubble was formed and excited by relativistically self-focused pump pulse since entering the gas jet (Fig. 4.5a), consistent with slight phase shift dips, < 0.5 rad, at $z = 1.50$ and 1.75 mm in Fig. 4.4c. Electrons are injected into and accelerated by the bubble at $z = 2.0$ mm (Fig. 4.5b), corresponding to phase shift dips 50–70 fs wide and > 1 rad deep at $z = 2.0$ to 2.5 mm (Fig. 4.4c). Electrons keep accelerated and gain energy until $z = 2.4$ mm where the first two plasma bubbles merge into a long blow-out channel (Fig. 4.5c). This beam loading induced coalescence of plasma bubble can be correlated to 100 fs wide and 2 rad deep phase shift dips in Fig. 4.4c and d after $z \sim 2.5$ cm. Slight dephasing of electrons and the plasma wakefields de-accelerates fast electrons injected earlier and further accelerates slow electrons injected later, yielding mono-energetic electron bunches as shown in Fig. 4.5d.

Simulations at density ($\bar{n}_e = 1.0 \times 10^{19} \text{ cm}^{-3}$) lower than optimal

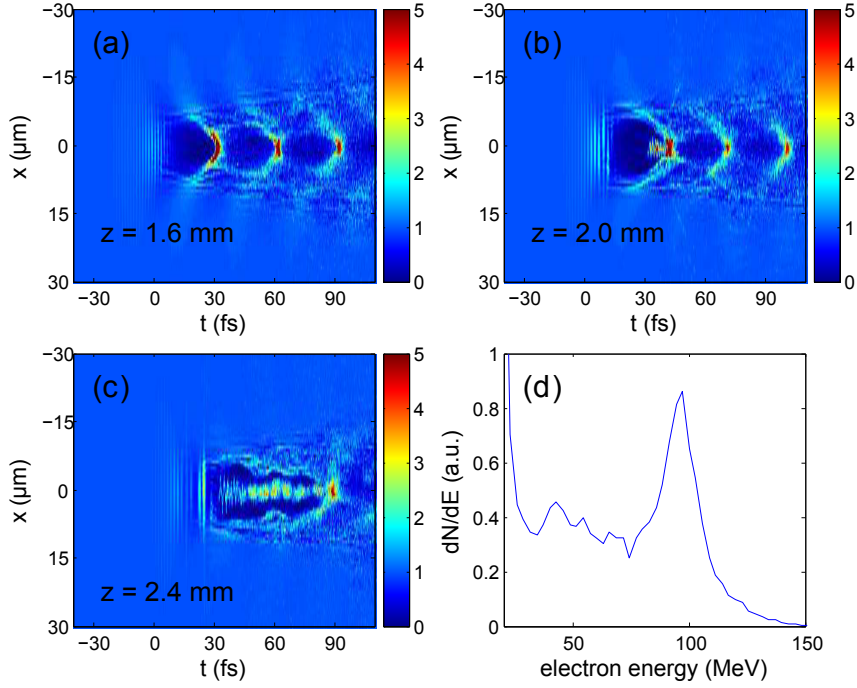


Figure 4.5: 3D particle-in-cell VLPL simulations of laser wakefield acceleration with optimal $\bar{n}_e = 1.5 \times 10^{19} \text{ cm}^{-3}$. **(a-c)** Plasma density profiles at $z = 1.6$ mm **(a)**, 2.0 mm **(b)** and 2.4 mm **(c)**, representing bubble formation, electron acceleration, and bubble coalescence respectively. **(d)** Calculated electron spectrum centered at 100 MeV.

showed, despite excitation of some quasi-linear plasma waves, no bubble formation, electron injection or acceleration, consistent with measurements at $\bar{n}_e = 1.3 \times 10^{19} \text{ cm}^{-3}$ (Fig. 4.4a). For a suboptimal density $\bar{n}_e = 1.3 \times 10^{19} \text{ cm}^{-3}$ corresponding to $\bar{n}_e = 1.5 \times 10^{19} \text{ cm}^{-3}$ in experiments, low energy, continuous spectrum electrons are observed in simulations. Basically, the acceleration process is limited by the gas jet length at this density, denoting an insufficient acceleration regime. For density ($\bar{n}_e = 2.0 \times 10^{19} \text{ cm}^{-3}$) higher than the optimum, simulations showed bubble formation and electron injection at $z \geq 1.5$

mm. Thus electrons accelerated up to the dephasing limit by $z \approx 2.0$ mm. Subsequent dephasing and beam loading induced bubble coalescence limited maximum electron energy to ~ 40 MeV, consistent with measurements for $\bar{n}_e = 2.2 \times 10^{19} \text{ cm}^{-3}$ (Fig. 4.4d). Thus simulations at various \bar{n}_e closely mirrored observed bubble dynamic trends, except for a somewhat lower value of the optimal \bar{n}_e . This discrepancy can be attributed to the higher quality and more effective self-focusing, of the simulated focused drive pulse, and highlights the need for laboratory visualization to supplement simulations.

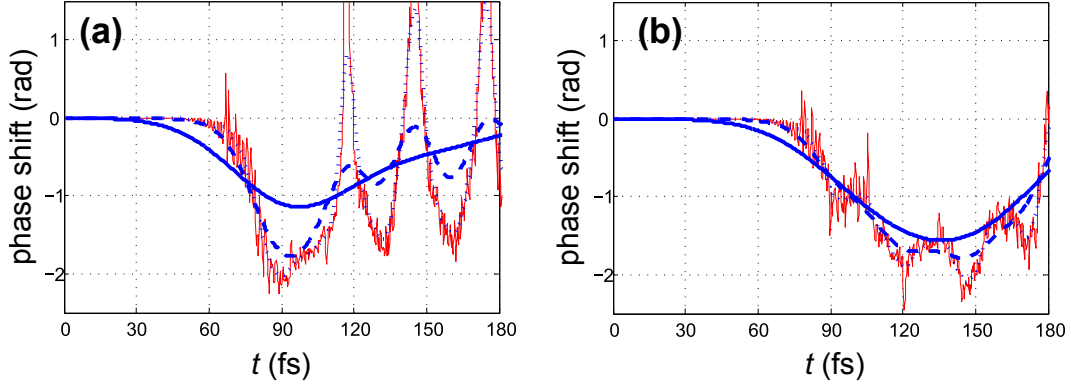


Figure 4.6: Calculated probe phase shift induced by plasma bubble in 3D PIC simulations (red solid, $\bar{n}_e = 2.0 \times 10^{19} \text{ cm}^{-3}$), convolved with probe longitudinal temporal resolution $\delta t = 50$ fs (blue solid), 19 fs (blue dash), and 5.3 fs (blue dot). **(a)** Phase shift induced by good-shaped bubble at $z \sim 2.0$ mm. **(b)** Merged bubble induced phase shift at $z \sim 2.5$ mm.

To correlate simulated plasma density profiles $n_e(t, x, y, z)$ directly to FDSC phase shifts, we calculated the phase shift $\psi(t, z)$ at selected z that the plasma refractive index profile $\eta(t, x, y, z)$ induced on the probe. Here t denotes time behind the center of the pump, and x, y transverse coordinates, in the

pump co-moving frame. $\eta(t, x, y, z)$ is sliced at a specific $y = y_0$, the central slice of the index object selected by the spectrometer slit, and is integrated over x , describing the drift of the index object across the probe profile transversely to the pump propagation direction. The red curves in Fig. 4.6 show line-outs of phase shift profiles $\psi(t, z)$ at $z = 2.0$ mm (a) and $z = 2.5$ mm (b) calculated for a probe of unlimited bandwidth, and thus arbitrary time resolution ($\delta t = 0$) in the pump co-moving frame, at density $\bar{n}_e = 2.0 \times 10^{19}$ cm⁻³. In practice, finite $\Delta\lambda_{\text{pr}}$ limits temporal resolution to δt . This limit was taken into account by convolving $\psi(t, z)$ with a Gaussian function with FWHM $\delta t = 50, 20, 5$ fs, yielding the blue curves respectively. For $\delta t = 50$ fs (solid blue lines in Fig. 4.6a), considerable longitudinal structure is lost because the duration $2\pi/\omega_p \approx 30$ fs of a single plasma period is less than δt at $z = 2.0$ mm (Fig. 4.6a, blue solid curves). Nevertheless the resulting 60 fs wide, 1 rad deep phase profile agrees well with the measured profile at $z \approx 2.0$ mm for these conditions. The dashed blue curve shows that some of the lost longitudinal structure could be recovered with a wider bandwidth probe equivalent to $\delta t = 19$ fs. At $z = 2.5$ mm (Fig. 4.6b), merging of adjacent buckets yields a broader phase profile without sharp boundaries that even the 10 nm bandwidth probe resolves well. The phase dip of duration 90 fs, depth 2 rad (Fig. 4.6, solid blue curve) reproduces the broadening and deepening observed for $z \geq 2.5$ mm. In this case, a broader bandwidth probe offers little improvement in longitudinal resolution (Fig. 4.6, dashed blue curve). Thus 3D PIC simulations corroborate the z -varying shape of the phase dip observed in the critical region $2 \geq z \geq$

2.5 mm (see Fig. 4.4c, d) where the fully formed bubble finishes accelerating electrons, then merges with the second bucket due to beam loading. A perfect probe with $\delta t = 5$ fs potentially can resolve extremely fine structures of bubbles as accurate as transverse techniques [9], however this requires sophisticated upgrade of the laser system.

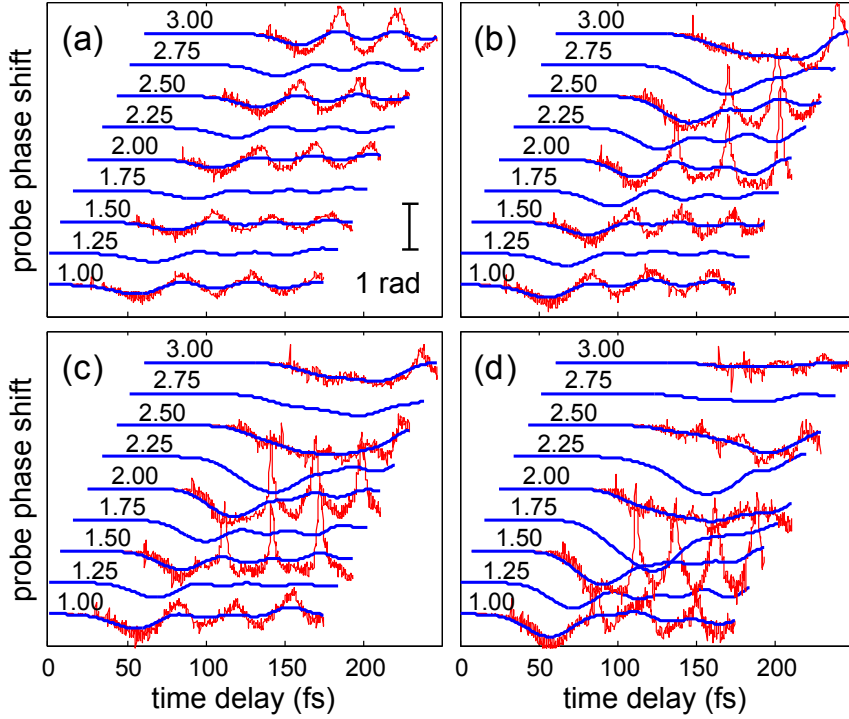


Figure 4.7: 3D PIC simulations of probe phase shift induced by laser wakefields at density: **(a)** $1.0 \times 10^{19} \text{ cm}^{-3}$; **(b)** $1.3 \times 10^{19} \text{ cm}^{-3}$; **(c)** $1.5 \times 10^{19} \text{ cm}^{-3}$; **(d)** $2.0 \times 10^{19} \text{ cm}^{-3}$. Actual phase shift profiles (red) are convolved with probe longitudinal temporal resolution $\delta t = 30$ fs (blue), illustrating the longitudinal time-resolution limit of the probe.

At different plasma density, simulated probe phase shift $\psi(t, z)$ is convolved with a $\delta t = 30$ fs wide (FWHM) Gaussian function, as shown in Fig. 4.7,

to be directly compared with Fig. 4.4. In the low density ($\bar{n}_e = 1.0 \times 10^{19} \text{ cm}^{-3}$) case in Fig. 4.7a, convolved line-outs show no phase dips since only low-amplitude linear plasma wave was excited through the 3 mm propagation distance. For higher density ($\bar{n}_e = 1.3 \times 10^{19} \text{ cm}^{-3}$, Fig. 4.7b), phase dips became visible until $z = 2$ to 2.5 mm, where nonlinear bubble regime was reached. At the optimal density ($\bar{n}_e = 1.5 \times 10^{19} \text{ cm}^{-3}$, Fig. 4.7c), bubble formation happened at $z \sim 2.0$ mm, consistent with Fig. 4.4c. In the over-acceleration regime ($\bar{n}_e = 2.0 \times 10^{19} \text{ cm}^{-3}$, Fig. 4.7d), fully developed bubble was observed at $z = 1.5$ mm and bubble coalescence happened after $z = 2$ mm to de-accelerate electrons. Moreover, the sudden longitudinal or temporal shift of phase dip minima (*e.g.* $z \sim 2.25$ mm (c) and $z \sim 1.75$ mm for (d) in both Fig. 4.4 and Fig. 4.7 consistently) presents a signature of multi-bubble merging into a single one.

In conclusion, frequency-domain streak camera has been successfully applied to visualize plasma bubble evolution in a single shot. Using this technique, major stages of bubble evolution — formation, stable propagation, broadening and coalescence — over a 10 ps interval with < 0.5 ps resolution are determined. Optimum accelerated electron energy (100 MeV) and pointing stability was observed for plasma density at which a bubble fully formed at dephasing length L_d before the gas jet exit. 3D PIC simulations reproduced the FDSC and electron acceleration results, and correlated them with underlying physics: relativistic self-focusing, electron injection into a fully formed bubble, dephasing, and bubble coalescence due to beam loading.

Chapter 5

Frequency–Domain Tomography

The previous two chapters demonstrated how the frequency–domain streak camera (FDSC) uses phase modulations imprinted on a single probe crossing the path of an evolving light-velocity object at angle θ to record a single-shot time sequence of the object’s projections at viewing angle $\phi(\theta)$, which is related to θ by Eq. (3.6). This chapter generalizes FDSC by employing *multiple* probes at different angles simultaneously [] to generate a single-shot “movie” — *i.e.* a time sequence of snapshots, each a 2-dimensional (2-D) slice of the object’s complete instantaneous spatiotemporal structure. Reconstructing a movie from phase streaks imprinted on multiple probes requires the methods of computerized tomography (CT). In conventional CT imaging of *static* objects, light or x-ray beams transmit through the object at different angles, encoding a projection of the object via absorption or phase shift onto each beam. Tomographic reconstruction algorithms then reconstruct the three-dimensional original object (or a 2-D slice) from these two-dimensional projections [34]. Here we employ a generalized version of these same tomographic reconstruction algorithms to reconstruct a 3-D movie (two spatiotemporal dimensions plus evolution) from several 2-D phase streaks. We call this method “Frequency–Domain Tomography” (FDT).

As in FDH, FDSC and conventional CT, we assume in this chapter that the phase-modulated region of each probe does not diffract significantly within the interaction region, but rather accumulates in the manner of geometric optics. This assumption sets an upper limit $L < L_{\text{diff}} \approx \pi(\Delta x^2 + \Delta y^2)/\lambda_{\text{pr}}$ on propagation distance L , where Δx and Δy are the transverse dimensions of the index structure, and λ_{pr} is the probe wavelength. Typically for micrometer-size objects probed at visible wavelengths, the FDT method is viable for propagation lengths up to several millimeters. For longer propagation lengths, it becomes necessary to image the probes to the detector from multiple object planes within the interaction region. Such multi-object plane imaging techniques are the subject of the next chapter.

5.1 Theory of Frequency–Domain Tomography

Here we briefly review the principles of conventional tomography for static objects before introducing tomography for ultrafast evolving, light-speed objects. To simplify the discussion, we consider the probing and reconstruction of a 2-D slice $f(x, y)$ of a static object at fixed z . To reconstruct the 3-D structure $f(x, y, z)$, the procedures described here are repeated at different z . One projection is formed by parallel light beams propagating through the object along a direction at angle θ to the x axis, as shown in Fig. 5.1. The projection variable along this direction is $u = x \cos \theta + y \sin \theta$; the variable along the orthogonal axis is $v = -x \sin \theta + y \cos \theta$. Thus the projection is $p(v, \theta) = \int f(u \cos \theta - v \sin \theta, u \sin \theta + v \cos \theta) du$. The Fourier transform of the

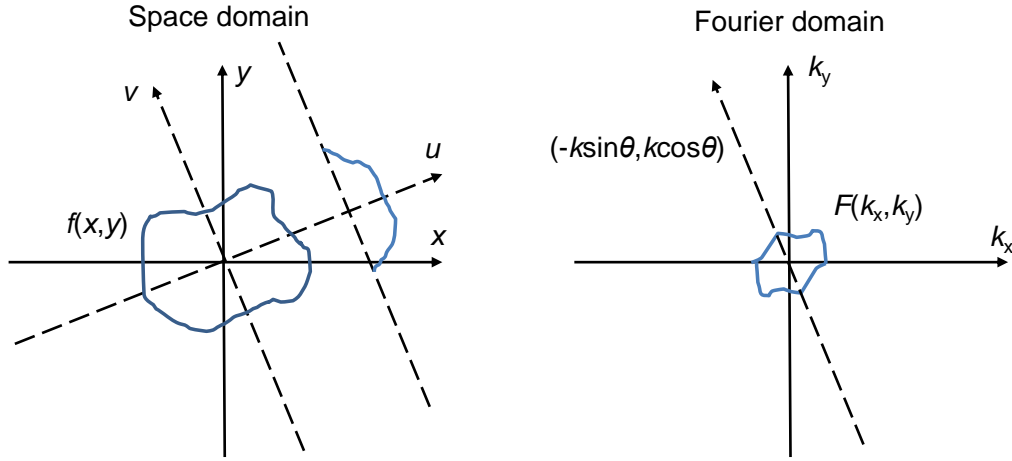


Figure 5.1: Conventional tomography for static objects in space domain (left) and Fourier domain (right).

projection is

$$\begin{aligned}
 P(k, \theta) &= \frac{1}{2\pi} \int p(v, \theta) e^{-ikv} dv \\
 &= \frac{1}{2\pi} \int f(u \cos \theta - v \sin \theta, u \sin \theta + v \cos \theta) e^{-ikv} du dv \\
 &= \frac{1}{2\pi} \int f(x, y) e^{-ik(-x \sin \theta + y \cos \theta)} dx dy \\
 &= 2\pi F(-k \sin \theta, k \cos \theta).
 \end{aligned} \tag{5.1}$$

Thus the 1D projection in the Fourier domain equals the line-out of the 2D object's Fourier transform along the direction at angle $\pi/2 + \theta$ to the k_x axis. This is the **Fourier slice theorem** [34]. If multiple probes are applied, the entire 2D profile of the object in the Fourier domain is known. Thus the object can be reconstructed in the space domain.

5.1.1 Tomography for light-speed objects

Frequency-domain tomography uses a generalized version of the Fourier slice theorem. Eq. (3.4) gives the 3D projection $\psi^{(\theta)}(\zeta_{\text{pr}}, x_{\text{pr}}, y_{\text{pr}})$ of a 4D light-speed object $\Delta n(\zeta, x, y, z)$ from a probe that crossed its path at lab angle θ . The Fourier transform of a 2D (constant $y = y_{\text{pr}}$) section of this projection is

$$\begin{aligned}
\Psi^{(\theta)}(k_1, k_2) &= \frac{1}{(2\pi)^2} \int \psi^{(\theta)}(\zeta_{\text{pr}}, x_{\text{pr}}) e^{-ik_1 v_{\text{pr}} \zeta_{\text{pr}} - ik_2 x_{\text{pr}}} d\zeta_{\text{pr}} dx_{\text{pr}} \\
&= \frac{v_{\text{pr}}^2}{2\pi \lambda_{\text{pr}} v_{\text{ob}}} \int \Delta n(\zeta_{\text{ob}}, x_{\text{ob}}, z_{\text{ob}}) e^{-ik_1 v_{\text{pr}} \zeta_{\text{pr}} - ik_2 x_{\text{pr}}} d\zeta_{\text{ob}} dx_{\text{ob}} dz_{\text{ob}} \\
&= \frac{4\pi^2 v_{\text{pr}}^2}{\lambda_{\text{pr}} v_{\text{ob}}} \Delta \tilde{n} \left[k_1 \cos \theta + k_2 \sin \theta, -k_1 \sin \theta + k_2 \cos \theta, k_1 \left(\cos \theta - \frac{v_{\text{pr}}}{v_{\text{ob}}} \right) + k_2 \sin \theta \right] \\
&= \frac{4\pi^2 v_{\text{pr}}}{\lambda_{\text{pr}} v_{\text{ob}}} \Delta \tilde{n} \left[k_{\zeta}, k_x, k_{\zeta} \left(1 - \frac{v_{\text{pr}}}{v_{\text{ob}}} \cos \theta \right) + \frac{v_{\text{pr}}}{v_{\text{ob}}} k_x \sin \theta \right], \tag{5.2}
\end{aligned}$$

where the coordinates $(\zeta_{\text{pr}}, x_{\text{pr}})$ and $(\zeta_{\text{ob}}, x_{\text{ob}})$ are related by the transformations (3.2) and (3.3). Thus the 2D Fourier transform of a phase streak $\psi^{(\theta)}(\zeta_{\text{pr}}, x_{\text{pr}})$ represents the Fourier transform of the original object's evolution history in the plane $k_z = k_{\zeta} \left(1 - \frac{v_{\text{pr}}}{v_{\text{ob}}} \cos \theta \right) + \frac{v_{\text{pr}}}{v_{\text{ob}}} k_x \sin \theta$ in (k_{ζ}, k_x, k_z) space (Fig. 5.2a). This is a generalized version of the Fourier Slice theorem for light-speed object tomography. The direction of the norm vector of this plane can be described by the azimuthal angle

$$\phi = \arctan \left(\frac{v_{\text{pr}} \sin \theta}{v_{\text{ob}} - v_{\text{pr}} \cos \theta} \right) \tag{5.3}$$

and the polar angle

$$\alpha = \arctan \sqrt{1 + \left(\frac{v_{\text{pr}}}{v_{\text{ob}}} \right)^2 - 2 \left(\frac{v_{\text{pr}}}{v_{\text{ob}}} \right) \cos \theta}. \tag{5.4}$$

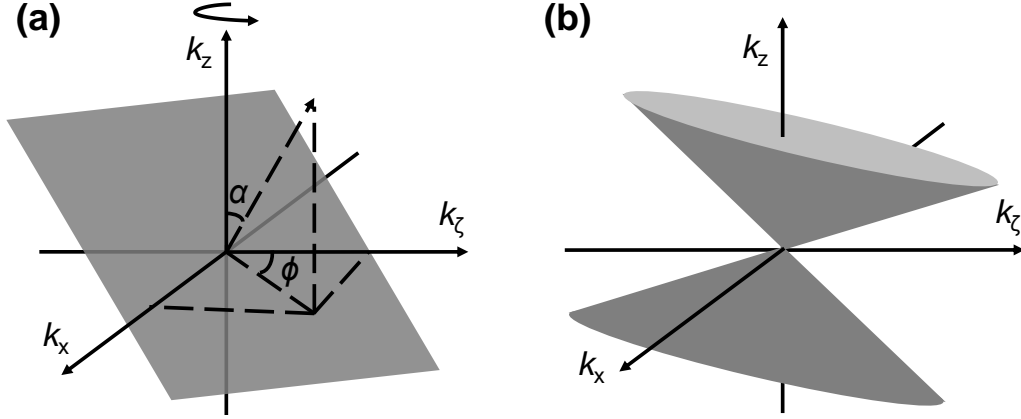


Figure 5.2: Principle of tomography for light-speed object. **(a)** The plane in which the transformed phase streak of a single probe at θ cuts the Fourier space of the object. The normal to the plane makes angle α with the k_z axis; its projection on the (k_x, k_ζ) plane makes angle ϕ with the k_ζ axis. **(b)** Cones containing the region of the Fourier space which can be sampled by the probe.

The azimuthal angle ϕ defines the projection direction of the object from the probe at lab angle θ , and is the same as the projection angle ϕ derived in Eq. 3.6. Consider an evolving object with characteristic size δr in this projection direction. The extent of $\Delta\tilde{n}$ in (k_ζ, k_x, k_z) space along this direction is $\sim 2\pi/\delta r$, so the maximum k_z that can be sampled is $\sim 2\pi/\delta r \tan \alpha = 2\pi/\delta r \sqrt{1 + \left(\frac{v_{\text{pr}}}{v_{\text{ob}}}\right)^2} - 2\left(\frac{v_{\text{pr}}}{v_{\text{ob}}}\right) \cos \theta$. This limited k_z bandwidth implies a maximum resolution of fast evolution along the propagation (z) direction of $\delta z = \delta r \sqrt{1 + \left(\frac{v_{\text{pr}}}{v_{\text{ob}}}\right)^2} - 2\left(\frac{v_{\text{pr}}}{v_{\text{ob}}}\right) \cos \theta$, which, not surprisingly, is equivalent to z resolution obtained in Eq. 3.7.

Additional probes at different lab angles θ correspond to planes cutting the object's Fourier space like the one shown in Fig. 5.2, but at different polar

angles $\alpha(\theta)$. Thus multiple probes applied simultaneously at densely-sampled angles define a sub-space in the 3D Fourier domain (k_ζ, k_x, k_z) equivalent to rotating a single plane around the k_z axis by changing its polar angle $\alpha(\theta)$ continuously. The result is a pair of cones as shown in Fig. 5.2b. The sub-space that can be sampled by oblique angle probes is the region *between* the pair of cones. The points, or (k_ζ, k_x, k_z) values, *inside* the cones are never sampled for any probe angle θ . Thus unlike conventional tomography for which information for complete reconstruction can be obtained in principle, tomography for light-speed objects is inherently limited in its sampling range. It is thus an inverse problem with limited data, so complete reconstruction of the original object from multiple probes is impossible. Nevertheless, with the help of additional *a priori* information, reconstruction errors can be minimized, analogous to the limit-angle theorem for conventional tomography of static objects [34].

An index object that varies slowly with z is an example of one that can be reconstructed faithfully by FDT. Most of its Fourier components are confined near the k_ζ - k_x plane, so no significant information is lost by the inability to sample the volume inside the cones in Fig. 5.2. In this case, as the index object passes through a plane transverse to the phase streak axis (corresponding to a specific propagation distance z), it evolves negligibly. Thus its projection and tomographic reconstruction in that portion of the streak are similar to those of a stationary object probed by conventional CT. Movie frames of the object's slowly-evolving spatiotemporal profile are then obtained by recording a sequence of projections at planes separated by the object's

dimension along each of several phase streak axes at different lab angles.

5.1.2 Filtered back-projection (FBP) reconstruction

Filtered back-projection (FBP) is a fundamental technique for tomographic reconstruction. It can be applied straightforwardly to reconstruct movies of slow-varying objects. In this case, the original slowly-varying 2D object $f(x, y)$ is reconstructed using Eq. (5.1):

$$\begin{aligned}
 f(x, y) &= \int \int f(k_x, k_y) dx dy \\
 &= \int \int f(-k \sin \theta, k \cos \theta) |k| dk d\theta \\
 &= \frac{1}{2\pi} \int \int P(k, \theta) |k| dk d\theta,
 \end{aligned} \tag{5.5}$$

where $P(k, \theta)$ is defined in Eq. (5.1). FBP reconstruction involves three steps: (i) Fourier transformation of the projections, (ii) application of a filter $|k|$ on the transformed projections, and (iii) back-projection of the original object. Once projections of phase streaks at different angles are lined-out at a specific propagation distance z , FBP yields the spatiotemporal index profile at z . However, if the slow-variation approximation is not strictly satisfied, a more general algorithm based on the generalized projection shown in Fig. 5.2 should be developed.

5.1.3 Algebraic reconstruction technique (ART)

Although filtered back-projection (FBP) method provides a conceptually simple reconstruction algorithm that is directly related to the Fourier Slice

theorem, we have found that an alternative approach known in tomography literature as the algebraic reconstruction technique (ART) [33] is more practical for FDT. ART is an iterative algorithm in which one guesses the object’s shape at each step, compares with measured projections, then modifies the guess until residuals are minimized. It thus resembles iterative techniques such as frequency-resolved optical gating (FROG) that are widely used to reconstruct the spatiotemporal profile of an ultrashort optical pulse. ART has two advantages over FBP for our application. First, for practical FDT, the number of probes is limited to ~ 15 by the probe generation and detection methods (discussed below) and by crowding of imaging optics, especially for single-shot imaging. Thus the projection angle cannot be sampled as densely as in conventional tomography of stationary objects, where beam sources and detectors rotate around the target. ART avoids “streak artifacts” typical of FBP reconstructions from sparsely sampled angular projections. Second, ART can conveniently incorporate prior information about the object (*e.g.* the sign of the refractive index change, the spatiotemporal profile of the drive pulse) in each iteration, whereas this is difficult for FBP. Thus ART deals more effectively with the limited-data inverse problem nature of FDT.

ART discretizes Eq. (3.4) by mapping the evolving 3D index structure $\Delta n(\zeta_{\text{ob}}, x_{\text{ob}}, z_{\text{ob}})$ for fixed y_{pr} onto a 3D grid in $(\zeta_{\text{ob}}, x_{\text{ob}}, z_{\text{ob}})$ space. Each pixel value ψ_i of a 2D phase streak in (ζ_{pr}, x_{pr}) space was obtained by applying a linear projection operator \mathbf{P} to the 3D tomographic movie Δn_j in $(\zeta_{\text{ob}}, x_{\text{ob}}, z_{\text{ob}})$

space,

$$\psi_i = \sum_j P_{ij} \Delta n_j, \quad (5.6)$$

where i spans indices of all pixels of 2D phase streaks at all angles and j labels all points of the index structure. Following the standard ART procedure [33, 34], we solved Eq. (5.6) iteratively by setting initial solution $\Delta n_j^{(0)} = 0$, then updating the solution to fit the measured phase streak ψ_i . Thus in the k th iteration, the solution is

$$\Delta n_j^{(k)} = \Delta n_j^{(k-1)} + \lambda \sum_i \frac{\psi_i - \sum_m P_{im} \Delta n_m^{(k-1)}}{\sum_m P_{im}^2} P_{ij}. \quad (5.7)$$

Here λ is the relaxation parameter for ART iterations, which we set to 0.1 to boost the convergence rate of the iteration. Additional prior information is usually incorporated in each step. For example, if the index structure Δn_j is excited by a laser pulse propagating in a positive Kerr medium (or plasma), the restriction $\Delta n_j \geq 0$ (or $\Delta n_j \leq 0$) is enforced by directly setting $\Delta n_j = 0$ for all calculated $\Delta n_j < 0$ (or $\Delta n_j > 0$) in Eq. (5.7). This guarantees that physical constraints are maintained during the reconstruction. No prior assumptions are made, however, about the symmetry of the evolving object, in contrast to *e.g.* Abel inversions that assume cylindrical symmetry. When the 2D projections $\psi^{(\theta)}(z_{\text{pr}}^{(\text{loc})}, x_{\text{pr}}, y_0)$ contained 2π jumps, a 2D phase unwrapping pre-processing procedure was applied to the measured phase ψ_i through the weighted minimum norm algorithm [31].

Computerized implementation of the ART algorithm for FDT requires careful evaluation of the size of the \mathbf{P} matrix. Assume the pixel number of the

3D evolving object is $N_{\text{movie}} = N_{\zeta} \times N_x \times N_z$, and the measured phase streaks at N_{ang} different angles, each with N_{pix} pixels, have total projection data number $N_{\text{proj}} = N_{\text{ang}} \times N_{\text{pix}}$. The size of the matrix \mathbf{P} should then be $N_{\text{movie}} \times N_{\text{proj}}$, which takes up to 700G Bytes memory if all matrix elements are saved in double-precision floating numbers. This is too large to be handled by current computers. However, as a huge, sparse matrix, non-zero elements of \mathbf{P} can be stored more efficiently. First of all, the rows of the matrix corresponding to zero-valued pixels of 2D phase streaks can be directly set to zero, and only the remaining rows calculated. The total effective projection data number is thereby reduced by an order of magnitude, *i.e.* $N'_{\text{proj}} = 10^{-1} N_{\text{proj}}$. In addition, for a single projection with fixed angle θ and probe coordinate $(\zeta_{\text{pr}}, x_{\text{pr}})$, the integral path is linear. Thus the non-zero elements in each row of matrix \mathbf{P} is no larger than $N_{\zeta} + N_x + N_z$, rather than $N_{\zeta} \times N_x \times N_z$. These at most $N_{\zeta} + N_x + N_z$ non-zero elements in each row of \mathbf{P} can be found by calculating the crossing points between the projection integral path and the walls of non-zero voxels. Thus the effective movie voxel number is $N'_{\text{movie}} = N_{\zeta} + N_x + N_z \approx 10^{-4} N_{\text{movie}}$. Taking advantage of these efficiencies, my C++ code “FDT3D” constructed the matrix \mathbf{P} by only storing non-zero elements whose number is no larger than $N'_{\text{movie}} \times N'_{\text{proj}} \sim 50\text{M Bytes}$ (see Appendix B). This size can be easily handled by an ordinary personal computer with Windows 7 operation system and Microsoft VC++ integrated development environment (IDE).

5.1.4 FDT reconstruction quality

FDT reconstruction quality depends on the number and distribution of probes, and is quantified via the normalized root mean squared (RMS) deviation d (or “error”) of a reconstruction $\Delta n(\zeta, x, z)$ from the evolving object $\Delta n_0(\zeta, x, z)$. We define d by generalizing its conventional 2D expression [34, 37] to 3D:

$$d = \sqrt{\sum_{\zeta, x, z} [\Delta n(\zeta, x, z) - \Delta n_0(\zeta, x, z)]^2 / \sum_{\zeta, x, z} [\Delta n(\zeta, x, z) - \Delta \bar{n}_0]^2}. \quad (5.8)$$

The ζ, x sums run over intra-frame pixels, the z sums over frames, and $\Delta \bar{n}_0$ is the object’s average index. The actual object $\Delta n_0(\zeta, x, z)$ is, of course, not directly accessible in a real tomographic reconstruction. Direct comparison of the reconstructed object with physical simulations and independent measurements are thus important for validating FDT reconstructions. In addition, d can be determined for a given probe configuration by simulating the reconstruction of a “phantom” object that is known exactly.

5.2 Phantom simulations

We tested the ART-based FDT reconstruction code by carrying out a set of “phantom” simulations, a common method of evaluating computerized tomography codes [34]. Fig. 5.3a shows selected 2D (x_{ob} vs. ζ_{ob}) snapshots of an artificial phantom index object at seven different propagation distances z_{ob} (listed along the top) ranging from entrance ($z_{\text{ob}} = 0$) to exit ($z_{\text{ob}} = 3$ mm) of the medium. The horizontal temporal scale of each snapshot de-

notes ζ_{ob} , with the object’s leading edge to the left. The phantom does not evolve by a real physical process, although some of its general features (*e.g.* propagation length, x_{ob} and ζ_{ob} dimensions, evolution speed) were chosen to resemble those that occur in experiments described in the next section. The phantom’s detailed features were chosen to illustrate resolution limits, and to evaluate reconstruction artifacts, more effectively than a real physical process. Specifically, the object starts as a hollow rectangle with thin boundaries of widths $\Delta\zeta_0 = 10$ fs (left and right) and $\Delta x_0 = 5$ μm (top and bottom), as shown by dotted curves in Fig. 5.4b and c, respectively. Such a thin rectangle separately and stringently tests transverse and longitudinal resolution limits. As it propagates at $v_{\text{ob}} = 0.68c$, chosen to equal pump group velocity in experiments discussed in the next section, the rectangle narrows along x_{ob} over $0 < z_{\text{ob}} < 1.5$ mm, thus mimicking self-focusing observed in those experiments. During a short transition period ($z_{\text{ob}} \sim 1.5 \pm 0.2$ mm), a “dot” of Gaussian profile appears to the lower right of the rectangle, quickly grows to Δn_{max} and falls to $0.2\Delta n_{\text{max}}$ (Fig. 5.4a, dotted curve), mimicking the time scale of plasma generation and partial recombination in the experiments. Since the dot grows within an interval (~ 100 fs) comparable to the object’s duration $\Delta\zeta_{\text{ob}}$, it tests inter-frame resolution. By breaking axial symmetry, it also tests the algorithm’s ability to reconstruct objects without prior assumptions about symmetry. The narrowed rectangle then expands longitudinally over $1.5 \text{ mm} < z_{\text{ob}} < 3$ mm, mimicking group-velocity stretching of a laser pulse.

Fig. 5.3b-d shows tomographic reconstructions of the phantom from

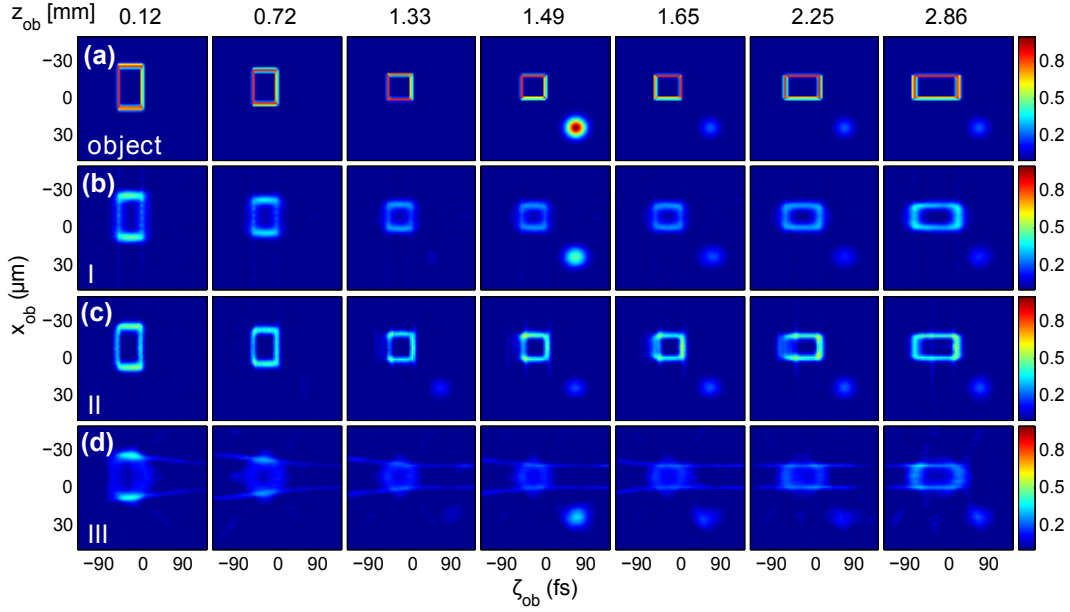


Figure 5.3: FDTD Phantom simulations. **(a)** 2D snapshots (ζ_{ob} vs. x_{ob}) of evolving “phantom” object at seven selected positions z_{ob} after entering a medium as it propagates with velocity $v_{\text{ob}} = 0.68c$. Remaining rows show tomographic reconstructions of the phantom object for three probe configurations: **(b)** 19 probes at projection angles $-90^\circ < \phi < 90^\circ$ with 10° separation, $v_{\text{pr}} = 0.70c$ (configuration I); **(c)** 18 probes at $-90^\circ < \phi < 80^\circ$ with 10° separation, $v_{\text{pr}} = 0.681c$ (configuration II); **(d)** 5 probes at $-70^\circ < \phi < 70^\circ$ with 35° separation, $v_{\text{pr}} = 0.66c$ (configuration III). The color bar shows the dimensionless refractive index change of original and reconstructed objects.

3 probe configurations I through III. Fig. 5.4a-c compares selected line-outs of the reconstructed images, with those of the object (dotted curves), while Fig. 5.4d plots RMS errors vs. iteration number. In all cases, the probe bandwidth and imaging optics fully resolved the object’s intra-frame ($\zeta_{\text{ob}}, x_{\text{ob}}$) features. Variations among reconstructions I–III thus arose solely from different probe number, angular distribution and velocity as follows: (I) 19 probes each with $v_{\text{pr}} = 0.70c$ distributed equally over projection angles $-90^\circ < \phi < 90^\circ$;

(II) 18 probes each with $v_{\text{pr}} = 0.681c$ distributed equally over $-90^\circ < \phi < 80^\circ$;
 (III) 5 probes each with $v_{\text{pr}} = 0.66c$ distributed equally over $-70^\circ < \phi < 70^\circ$.
 As expected, configurations I, II with 18-19 probes yielded sharper frame images of the slowly evolving rectangle (Fig. 5.3b,c) and sharper line-outs of its edges (blue and red curves, respectively, in Fig. 5.4b,c), than 5-probe configuration III, which yielded more blurred images with reconstruction artifacts (Fig. 5.3d) and less distinct edge line-outs (dashed green curves, Fig. 5.4b,c). Reconstructions I and II also converged more rapidly toward smaller steady-state RMS error than configuration III (Fig. 5.4d). Thus large probe number is one factor that promotes high-fidelity reconstruction of slowly evolving objects. On the other hand, all three configurations resolved the rectangle’s slow narrowing and lengthening equally well (see Fig. 5.3b-d).

Reconstructions of the “dot” reveal more subtle comparisons. Configuration I, having the widest ϕ range and largest $|v_{\text{pr}} - v_{\text{ob}}| = 0.02c$, best resolved the dot’s ultrafast evolution (Fig. 5.4a, blue curve), consistent with the discussion of FDT resolution in Sec. 3.1.3. Configuration III, having the same $|v_{\text{pr}} - v_{\text{ob}}|$ and similar ϕ range, resolved this feature nearly as well (Fig. 5.4a, dashed green curve), despite only 5 probes. Configuration II, in contrast, failed completely to resolve it (Fig. 5.4a, red curve), a consequence of its small $|v_{\text{pr}} - v_{\text{ob}}| = 0.001c$. Nevertheless, configuration II yielded sharper images of the rectangle (Fig. 5.3c) and smaller RMS error (Fig. 5.4d) than configuration I, despite one less probe. Evidently reduced blurring of slowly evolving objects is a compensating advantage of small $|v_{\text{pr}} - v_{\text{ob}}|$. Thus in choosing $|v_{\text{pr}} - v_{\text{ob}}|$

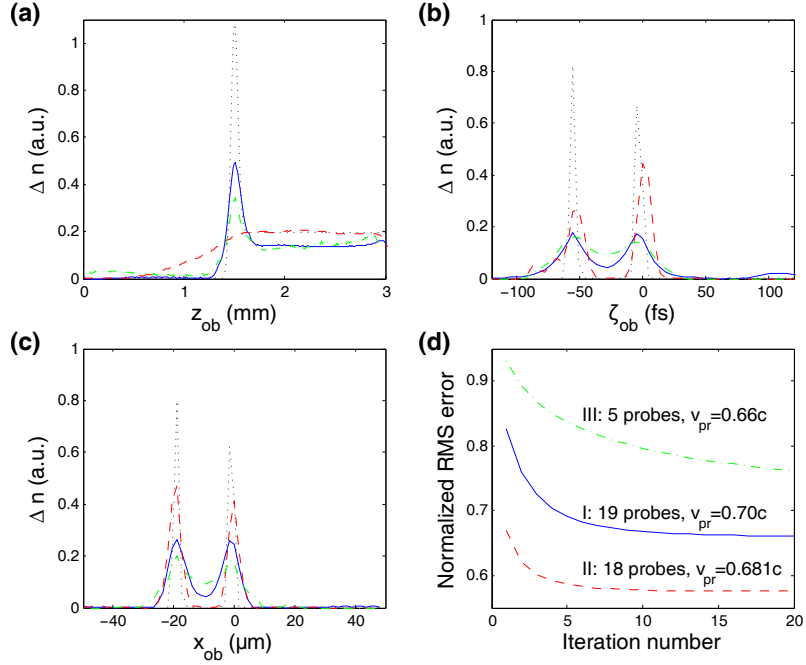


Figure 5.4: Analysis of phantom simulations. **(a)** Peak Δn of the Gaussian “dot” vs. evolution time z_{ob} , demonstrating inter-frame resolution; **(b)-(c)** line-outs at $z_{ob} = 1.5$ mm of the rectangle along ζ_{ob} **(b)** and x_{ob} **(c)**, demonstrating intra-frame resolution. Curves in **(a)-(c)** refer to phantom simulations in Fig. 5.3: original object (black dotted curve) and reconstructions with 19 (red dashed curve), 18 (blue solid curve) and 5 (green dash-dot curve) probes. **(d)** Normalized root mean square error of the same 3 tomographic reconstructions vs. iteration number.

an FDT system designer must compromise between resolving inter-frame evolution and minimizing intra-frame RMS error.

5.3 Experimental FDT setup

As a laboratory demonstration of FDT, we visualized nonlinear propagation of a laser pulse in fused silica. The evolving index structure is a 3D

slice $\Delta n(\zeta_{\text{ob}}, x_{\text{ob}}, z_{\text{ob}})$ of the nonlinear refractive index profile of a pump pulse (duration $\tau_{\text{pu}} = 100$ fs, wavelength $\lambda_{\text{pu}} = 800$ nm, energy $0.4 \leq E_{\text{pu}} \leq 0.7 \mu\text{J}$) focused with f -number ~ 30 to radius $w_0 = 25 \mu\text{m}$ (peak incident intensity $0.4 \leq I_0 \leq 0.7 \text{ TW cm}^{-2}$) near the entrance of a Kerr medium: a fused silica plate of linear index $n_0(\lambda_{\text{pu}}) = 1.45$ and lowest-order Kerr coefficient $n_2 \approx 2 \times 10^{-16} \text{ cm}^2\text{W}^{-1}$. Incident power exceeded the critical power $P_{\text{cr}} = 3.7\lambda_{\text{pu}}^2/8\pi n_0 n_2 \approx 3.2 \text{ MW}$ for self-focusing by a factor of 1.2 to 2.2. Our plate thickness $L = 3 \text{ mm}$ satisfied the weak diffraction criterion $L_{\text{eff}} < L_{\text{diff}}^{(\text{pr})}$ discussed in connection with Eq. (3.1). At our highest E_{pu} , we observe a 3D slice of dynamics preceding self-guided filament formation [14, 87].

The primary technical challenge in implementing FDT in the laboratory is to avoid runaway complexity and cost in generating, formatting and detecting a multi-probe pulse array. Conventional multi-probe experiments require an array of beam splitters to divide probes from pump, and a multi-mirror hyper-Michelson interferometer to format the probe train [76]. Such setups are challenging to align and sensitive to vibrations. Moreover, recording the phase streaks by conventional FDH methods requires a separate spectrometer with charge-coupled device (CCD) detector for each probe.

We addressed this challenge with the setup in Fig. 5.5. Only two “probe generating” pulses (800 nm, 30 fs, 30 μJ) were split directly from the pump. These crossed simultaneously at a small adjustable angle ($\alpha \sim 5 \text{ mrad}$) in a 3-layer structure consisting of a β -barium borate (BBO) crystal sandwiched between two HZF4 glass plates. Cascaded four-wave-mixing in the first HZF4

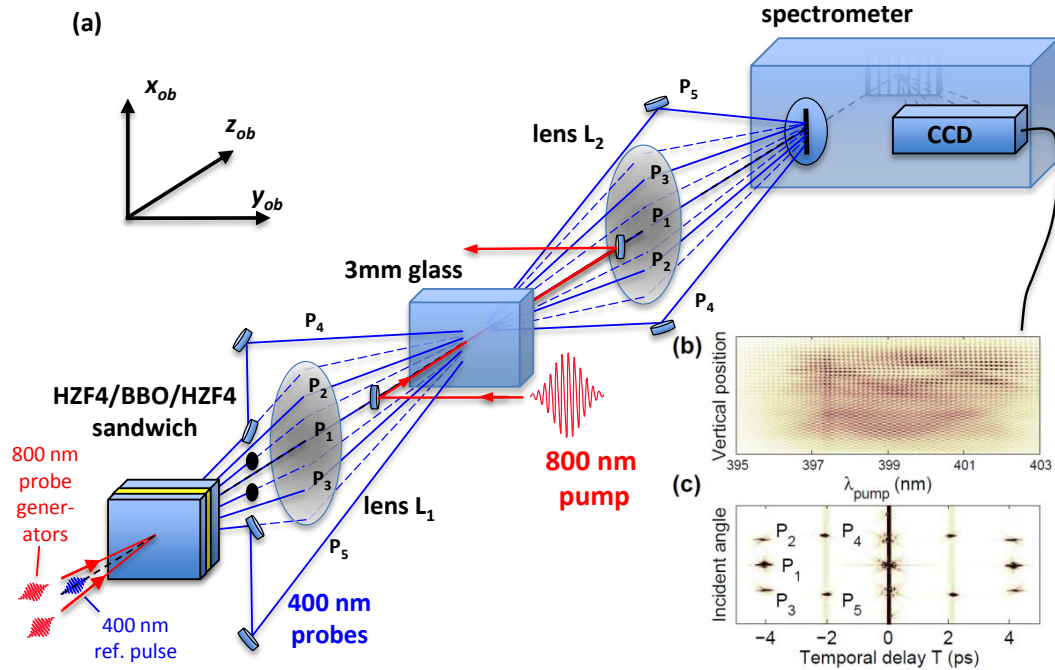


Figure 5.5: Schematic set-up for single-shot FDT of evolving laser-generated structures. (a) Experimental setup for probe generation and delivery to the imaging spectrometer. (b) Frequency-domain hologram, or interference pattern, of five probe and reference pulse detected by the CCD camera of the spectrometer. (c) Fourier transformation of the frequency-domain hologram yields a reciprocal hologram, in which peaks P_1 thru P_5 encode the phase modulations of the 5 probes. Phase streaks in Fig. 5.6 are recovered by windowing and inverse Fourier transforming these 5 peaks.

plate (5 mm thick, $n_2^{(\text{HZF4})} \sim 10^{-15} \text{ cm}^2\text{W}^{-1}$) created a fan of up to eight 800 nm daughter pulses. The number depended on probe generator intensity, and was limited by the onset of self-focusing and self-phase modulation. The BBO crystal (Type I, 500 μm thick) then frequency-doubled each beam, and created an additional probe midway between each fundamental pair by sum-frequency generation, producing a fan of up to fifteen 400 nm probes separated from each other by angle $\alpha/2$. The second HZF4 plate (15 mm thick) chirped them to 600 fs duration. Any desired subset of the array was easily selected by blocking unwanted probes. Here, for reasons discussed further below, we selected 5 probes at $\theta = 0.1^\circ, 1.4^\circ, -1.2^\circ, -7.6^\circ$ and 9.5° inside the fused silica, corresponding to projection angles $\phi = 1.0^\circ, 27^\circ, -25^\circ, -65^\circ$ and 68° , respectively, for $v_{\text{ob}} = 0.68c$ and $v_{\text{pr}} = 0.66c$.

Spatio-temporal overlap of multiple probes was achieved automatically by imaging the first HZF4 glass plate to the sample with lens L_1 ($f = 20 \text{ cm}$, 3 cm diameter). The pump-generated object swept across, and imprinted a phase streak on, each probe. To probe at angles θ beyond the aperture of L_1 , mirrors can re-direct selected probes from the fan along independent delivery lines to the sample. This was done for our two largest angle probes P_4, P_5 . As shown in Fig. 5.5, a chirped 400 nm reference pulse, also split from the pump, co-propagated with it, advanced temporally by $T \sim 2\text{--}4 \text{ ps}$.

Lens L_2 ($f = 15 \text{ cm}$, f -number 5.6) imaged reference and phase-modulated probes from the sample exit face to the slit of a single imaging spectrometer, which selected a line-out of constant y_0 , thus limiting the final

reconstructed objects to 3D slices $\Delta n(\zeta_{\text{ob}}, x_{\text{ob}}, y_0, z_{\text{ob}})$ of the full 4D object $\Delta n(\zeta_{\text{ob}}, x_{\text{ob}}, y_{\text{ob}}, z_{\text{ob}})$. Lens L_2 also ensured simultaneous, spatially-overlapped delivery of all probes within its aperture. Reference and probes interfered inside the spectrometer, projecting a grid-like frequency-domain intensity pattern or hologram $I(\omega, x)$ (Fig. 5.5b) onto the CCD. This hologram stored the phase modulations of all probes in one shot, analogous to coherent multiplexing methods in holographic data storage [35]. To analyze phase shift in each probe, a 2D Fourier transform of $I(\omega, x)$ yielded a reciprocal 2D hologram $\tilde{I}(T, \theta'_i)$ (Fig. 5.5c), in which each reference-probe interference pattern appeared as an isolated peak (P_1 thru P_5) at a position determined by probe angle θ'_i and time-delay T . Peaks $P_{4,5}$ appear at a different T than other peaks because P_4 and P_5 have their own references (not shown). Each phase streak was reconstructed by windowing and inverse Fourier-transforming a specific peak P_i , as in FDH.

The peaks P_i in the reciprocal hologram must be well separated to avoid cross-talk. Generally, the maximum number N of probes is limited by this peak separation, which is related in turn to the angular separation $\Delta\theta$ between probes. In the experiment, $\Delta\theta$ was limited to the probe divergence angle $\Delta\theta_{\text{min}} = \lambda_{\text{pr}}/\Delta x_{\text{ob}}$, or ~ 10 mrad for our system. On the other hand, the spectrometer CCD pixel size $x_{\text{pix}} \sim 40 \mu\text{m}$ limited the maximum probe-reference angular separation to $\theta_{\text{max}} = M\lambda_{\text{pr}}/x_{\text{pix}} \sim 200$ mrad, where $M \sim 20$ is the magnification of lens L_2 . Thus ideally our system supports $N_{\text{max}} = \theta_{\text{max}}/\Delta\theta_{\text{min}} \sim 20$. In practice, θ_{max} is limited to ~ 100 mrad (and N_{max}

to ~ 10) by the physical aperture and spherical aberration of lenses L_1 and L_2 . We chose $\Delta\theta$ conservatively at $\sim 2\Delta\theta_{\min}$ to thoroughly eliminate cross-talk, yielding five probes. Although this 5-probe system adequately resolved the main self-focusing dynamics, a substantial increase in probe number and image quality is available by investing in large aperture, aberration-corrected lenses and a larger, more finely-pixelated CCD.

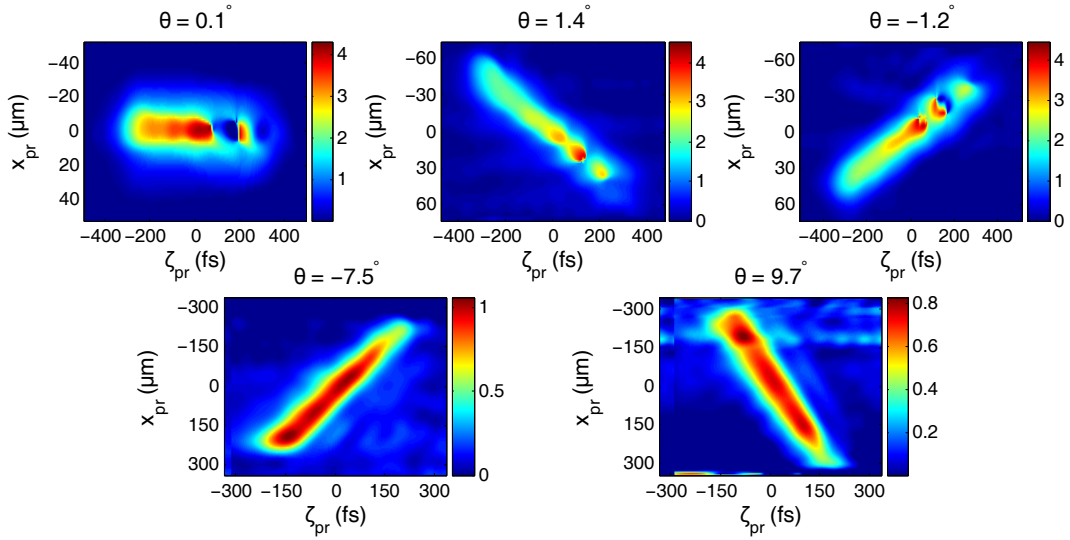


Figure 5.6: Phase streaks induced by the evolving index profile. $E_{\text{pu}} = 0.7\mu\text{J}$, and projection angles are $\phi = 1.0^\circ, 27^\circ, -25^\circ$ (top row), and -65° and 68° (bottom). Vertical (horizontal) scales denote transverse (longitudinal) position of the pump-induced phase streak within the temporally stretched probe pulse profile. The left-most end of each streak corresponds to the entrance of the medium; $\zeta_{\text{pr}} = x_{\text{pr}} = 0$ is approximately the mid-point of the pump pulse propagation through the Kerr medium. The spectrometer slit was centered on the images that L_2 projected at the spectrometer entrance. Color bars give phase shift in rad.

Figure 5.6 shows 5 phase streaks for $E_{\text{pu}} = 0.7 \mu\text{J}$. Small ϕ streaks (top row) highlight evolution of the object's transverse (x_{ob}) profile. Oscil-

lations in transverse radius Δx_{ob} and peak index change Δn_{max} , indicating dynamic balance between self-focusing and defocusing, were evident in the last $\sim 1/3$ of these streaks. Streaks near $\phi \sim 70^\circ$ (bottom row) highlight evolution of its longitudinal (ζ_{ob}) profile, which remained nearly constant due to the low dispersion of fused silica. To visualize evolution of the object's full $\Delta n(\zeta_{\text{ob}}, x_{\text{ob}}, y_0, z_{\text{ob}})$ profile, we tomographically reconstructed a movie from all five streaks using the ART algorithm [33, 34, 59].

5.4 Single-shot tomographic movies

5.4.1 Laser pulse self-focusing and plasma ionization

Figure 5.7a shows movie frames, or 2D snapshots, of the nonlinear index profile $\Delta n(\zeta_{\text{ob}}, x_{\text{ob}})$ at 5 selected propagation distances z_{ob} after entering ($z_{\text{ob}} = 0$), and before exiting ($z_{\text{ob}} = 3$ mm), the Kerr medium, for E_{pu} from 0.4 μJ (top row) to 0.7 μJ (bottom row). The inter-frame spacing ($\Delta z_{\text{ob}} = 500$ μm) approximates the inter-frame resolution limit for transverse profile variations and twice this limit for longitudinal variations. The main feature in each frame is a positive $\Delta n(\zeta_{\text{ob}}, x_{\text{ob}})$ profile of transverse $1/e^2$ radius $13 < \Delta x_{\text{ob}} < 25$ μm and longitudinal duration ~ 100 fs, that is attributable mainly to the instantaneous lowest-order nonlinear Kerr response $n_2 I_{\text{pu}}$ of fused silica to the pump pulse. Diffraction, characterized by length $L_{\text{diff}}^{(\text{pu})} = \pi(\Delta x_{\text{ob}})^2 / \lambda_{\text{pu}} n_0(\lambda_{\text{pu}})$, and self-focusing, characterized by focal length $L_{\text{nl}} = \lambda_{\text{pu}} / 2\pi n_0 n_2 I_{\text{pu}}$ [68], respectively, govern most transverse pump dynamics. The reconstruction resolves them as long as $L_{\text{diff}}^{(\text{pu})} > 500 \mu\text{m}$ (*i.e.*

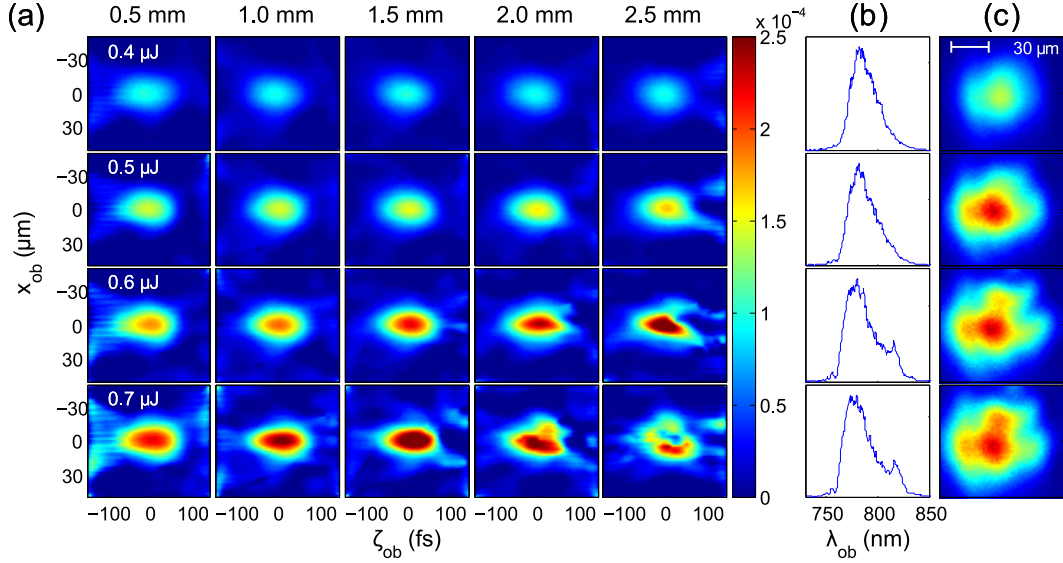


Figure 5.7: Single-shot tomographic movies of the evolving index profile. **(a)** Selected 2D snapshots $\Delta n(\zeta_{\text{ob}}, x_{\text{ob}})$ of the pump nonlinear index profile at 5 different propagation positions z_{ob} indicated at top, and pump energies indicated at left. The color bar shows the dimensionless refractive index change. **(b)** Spectra of the transmitted pump pulses. The spectrum in the top row is nearly identical to the incident spectrum. **(c)** Near field images of the transmitted pump spatial profiles, with a resolution of $\sim 20 \mu\text{m}$.

$\Delta x_{\text{ob}} > 14 \mu\text{m}$) and $L_{\text{nl}} > 500 \mu\text{m}$ (*i.e.* $I_{\text{pu}} < 1 \text{ TW cm}^{-2}$). Self-focusing beyond these limits can introduce dynamics faster than the inter-frame resolution, as well as additional nonlinearities such as plasma generation [44, 64, 88] and higher-order Kerr effect [3, 4, 20]. Dispersion, characterized by length $L_{\text{dis}} = \tau_{\text{pu}}^2 / \beta_2 = 277 \text{ mm}$, governs evolution of the longitudinal profile [68]. Since $L_{\text{dis}} \gg L$, the pulse and its $n_2 I_{\text{pu}}$ profile propagate with negligible change in duration.

The reconstructed movies in Fig. 5.7a depict various propagation regimes.

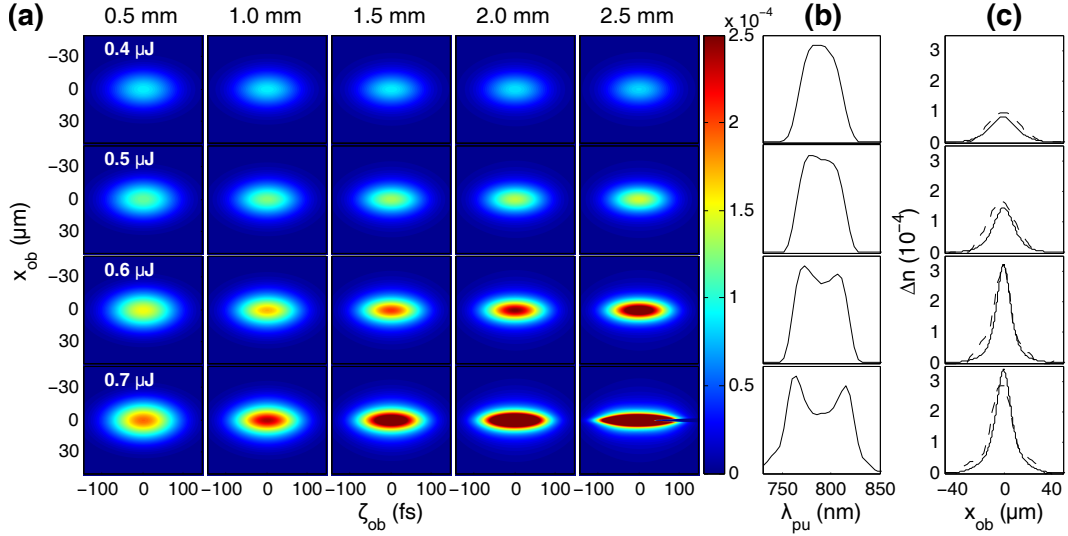


Figure 5.8: NLSE-simulated movies of the evolving index profile. **(a)** Selected 2D snapshots $\Delta n(\zeta_{ob}, x_{ob})$ of the pump nonlinear index profile from NLSE simulations for the same 4 pump energies and same 5 propagation times as shown in Fig. 5.7a. The color bar indicates the dimensionless refractive index change. **(b)** Spectra of the transmitted pump pulses from NLSE simulations, for direct comparison with measured spectra shown in Fig. 5.7b. **(c)** Solid curves: NLSE-simulated pump transverse spatial profiles at $\zeta_{ob} = 0$ near the exit plane ($z_{ob} = 2.5$ mm) for pump energy from 0.4 to 0.6 μJ , and at $z_{ob} = 1.5$ mm for 0.7 μJ . Dashed curves: corresponding line-outs of FDT-reconstructed pump spatial profile from Fig. 5.7a for direct comparison.

For $E_{pu} = 0.4$ μJ (top row), Δx_{ob} and index shift $\Delta n(\zeta_{ob} = 0, x_{ob} = 0)$ at the center of the profile remained nearly constant over 3 mm propagation distance, indicating that diffraction and self-focusing were balanced. For $E_{pu} = 0.5$ μJ (2nd row), Δx_{ob} contracted slightly, while $\Delta n(0, 0)$ increased slightly (I_{pu} increased from 0.5 to 0.6 TW cm^{-2}), indicating that self-focusing slightly dominated. In these cases, the exit pump spectrum (Fig. 5.7b, top 2 rows) and spatial profile (Fig. 5.7c, top 2 rows) retained nearly their incident shapes (not

shown), and transverse dynamics were fully resolved. At $E_{\text{pu}} = 0.6 \mu\text{J}$, the pulse self-focused strongly and monotonically to $\Delta x_{\text{ob}} \approx 15 \mu\text{m}$ and $I_{\text{pu}} > 1.5 \text{ TW cm}^{-2}$, indicating that self-focusing dynamics slightly exceeded the inter-frame resolution limit near the end of the medium. New structure developed in the output spectrum (Fig. 5.7b, 3rd row), a consequence of self-phase modulation, and in the spatial profile, which split into 3 lobes (Fig. 5.7c, 3rd row). The last movie frame shows the uppermost of these lobes separating from the central profile at $z_{\text{ob}} = 2.5 \text{ mm}$, thus capturing the onset of multi-filamentation. The other lobe lies outside the image plane.

At $E_{\text{pu}} = 0.7 \mu\text{J}$, similar structure developed in the exit spectrum and beam profile (Fig. 5.7b,c, 4th row). In this case, however, the pulse self-focused to $\Delta x_{\text{ob}} \approx 15 \mu\text{m}$ ($I_{\text{pu}} > 1.5 \text{ TW cm}^{-2}$) within $z_{\text{ob}} = 1.5 \text{ mm}$ (Fig. 5.7a, 4th row) instead of $z_{\text{ob}} = 3 \text{ mm}$, after which further collapse was arrested and sub-structure developed in the index profiles. One such sub-structure is the split-off of the upper spatial lobe, now evident at $z_{\text{ob}} = 2.0 \text{ mm}$. The dominant new feature, appearing at $z_{\text{ob}} = 2.5 \text{ mm}$, is a steep-walled index “hole” near the center of the Δn profile. No such “hole” was observed in the exit beam profile (Fig. 5.7c, 4th row). Thus it is the result of a negative index change that locally cancels the positive nonlinear index change $n_2 I_{\text{pu}}$. This feature appears within a single frame and thus, like the “dot” in the phantom simulations of Fig. 5.3, tests the inter-frame resolution of the tomographic reconstruction.

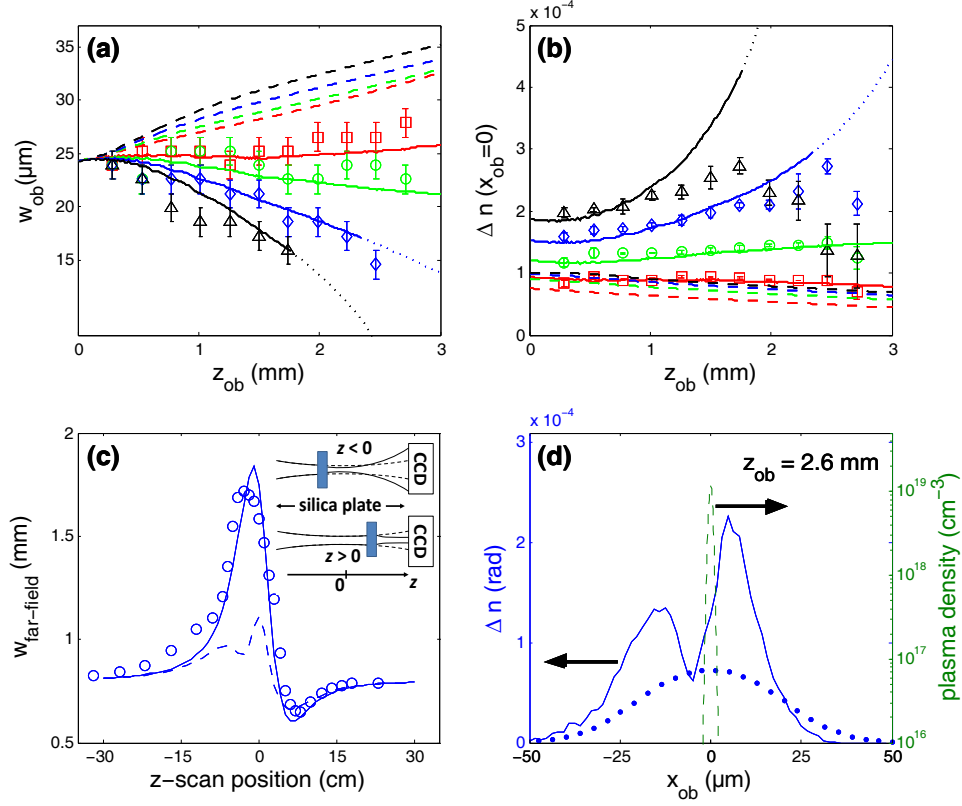


Figure 5.9: Comparison of FDT data with NLSE simulations. **(a)** Reconstructed radius Δx_{ob} and **(b)** index shift $\Delta n(\zeta_{ob} = 0, x_{ob} = 0)$ at the center of Kerr profiles $\Delta n(\zeta_{ob}, x_{ob}, z_{ob})$ from Fig. 5.7a vs. propagation position z_{ob} . Data points are for various E_{pu} : red squares, 0.4 μJ; green circles, 0.5 μJ; blue diamonds, 0.6 μJ; black triangles, 0.7 μJ. For $E_{pu} = 0.7$ μJ and $z_{ob} > 1.6$ mm, Δx_{ob} is not well defined because of the complex Kerr profile shape, and thus is not plotted. Solid curves are from NLSE calculations taking only $n_2 I_{pu}$ into account; the dotted portion of these curves indicates the region after multiple filaments formed. Dashed curves include 4th-order Kerr effect with $n_4 = -3.3 \times 10^{-28} \text{ cm}^4 \text{ W}^{-2}$ [20]. **(c)** Results of z-scan measurements of Kerr lensing by the fused silica plate, as illustrated in inset. Solid blue curve is calculated radius based on lowest-order Kerr lensing, dashed curve includes n_4 as above. **(d)** Lineout (solid blue curve) of Δn vs. x_{ob} at $\zeta_{ob} = 0$, $z_{ob} = 2.6$ mm, showing index hole near center of the Kerr profile, compared to calculated radial distribution of plasma density (dashed curve) at $z_{ob} = 2.6$ mm due to 6-photon ionization. Dotted blue curve shows suppression of the Kerr profile from 4th-order Kerr effect using n_4 as above.

5.4.2 Comparison of FDT reconstruction with NLSE simulations

To help understand the results in Fig. 5.7, we calculated propagation of the pump using a nonlinear Schrödinger equation (NLSE) [14, 87] that included diffraction, group-velocity dispersion, self-steepening, electronic and Raman-induced Kerr self-focusing, multi-photon and tunneling ionization [39], electron-hole recombination, and plasma defocusing, as discussed in Sec. 1.1. Input pulses were modeled as Gaussians that retained cylindrical symmetry as they propagated [14, 87]. The calculations thus do not capture asymmetric multi-filamentation observed in some FDT images, but adequately model propagation up to the formation of such filaments. Pump pulse propagation was simulated using the model in Ref. [14], in which a NLSE and a coupled electron-hole plasma generation-recombination equation were solved numerically.

$$\frac{\partial A}{\partial z} = \frac{i}{2k_0 n} T^{-1} \nabla_{\perp}^2 A - \frac{i\beta_2}{2} \frac{\partial^2 A}{\partial \zeta^2} + N_{NL} \quad (5.9)$$

$$\frac{\partial \rho}{\partial \zeta} = W_{PI}(|A|^2) + \frac{\sigma|A|^2}{E_g} \rho - \frac{\rho}{\tau_r}. \quad (5.10)$$

In the NLSE, the first and second terms are responsible for transverse diffraction and longitudinal dispersion respectively, and the third nonlinear term $N_{NL} = ik_0 n_2 T [(1 - f_R)|A|^2 + f_R R(\zeta) \otimes |A(\zeta)|^2] A - \frac{\sigma}{2}(1 + i\omega_0 t_c) T^{-1}(\rho A) - \frac{W_{PI}(|A|^2) E_g}{2|A|^2} A$ denotes instantaneous Kerr effect, delayed Raman-induced Kerr effect, plasma absorption/defocusing, and photo-ionization loss of the laser wave. We also performed some simulations that included a fourth-order Kerr term $n_4 I_{\text{pu}}^2$ term, as discussed in the next section. The operator $T = 1 +$

$(i/\omega_0)\partial/\partial\zeta$ leads to self-steepening and space-time coupling. The plasma generation-recombination equation has taken photo-ionization, avalanche ionization, and recombination into account, while the photo-ionization term $W_{PI}(|A|^2)$ is based on Keldysh's formulation generalizing both multi-photon and tunneling ionization mechanisms [39]. To compare simulation results with experimental data, transverse (longitudinal) imaging resolution $\Delta x_{\text{res}} \sim 5 \mu\text{m}$ ($\Delta z_{\text{res}}^{(\text{loc})}/v_{\text{ob}} \sim 70 \text{ fs}$) were taken into account by convolving the simulated index profile with a Gaussian function with transverse (longitudinal) dimension Δx_{res} ($\Delta z_{\text{res}}^{(\text{loc})}/v_{\text{ob}}$). Simulation parameters were either from our direct measurements (*e.g.* $n_2 = 2 \times 10^{-16} \text{ W} \cdot \text{cm}^{-2}$ from z-scan measurements) or most recent references for each parameter: $n_4 = -3.3 \times 10^{-28} \text{ W} \cdot \text{cm}^{-2}$ [20]; $n_0 = 1.45$, group velocity dispersion $\beta_2 = 36.1 \text{ fs}^2\text{mm}^{-1}$, silica band-gap $E_g = 9 \text{ eV}$, and constants $\tau_d = 32 \text{ fs}$, $\tau_s = 12 \text{ fs}$, $f_R = 0.18$ for the Raman response function $R(\zeta) = \tau_s(\tau_s^{-2} + \tau_d^{-2}) \exp(-\zeta/\tau_d) \sin(\zeta/\tau_s)$ [14]; plasma collision time $\tau_c = 1.7 \text{ fs}$ and plasma recombination time $\tau_r = 170 \text{ fs}$ [80].

Figure 5.8a shows multi-frame movies of the evolving $\Delta n(\zeta_{\text{ob}}, x_{\text{ob}}, z_{\text{ob}})$ from NLSE simulations neglecting HOKE, for direct comparison with FDT reconstructions in Fig. 5.7a. Simulated and reconstructed movies agree with high fidelity despite the lack of any adjustable parameters. To quantify this agreement, Table 5.1 lists RMS deviations d between the FDT reconstructions in Fig. 5.7a and the NLSE simulations in Fig. 5.8a. For most frames of Fig. 5.7a, $d \leq 0.5$, even smaller than for the 18-19 probe configurations of the phantom simulation (see Fig. 5.4d). This reflects the high fidelity of these

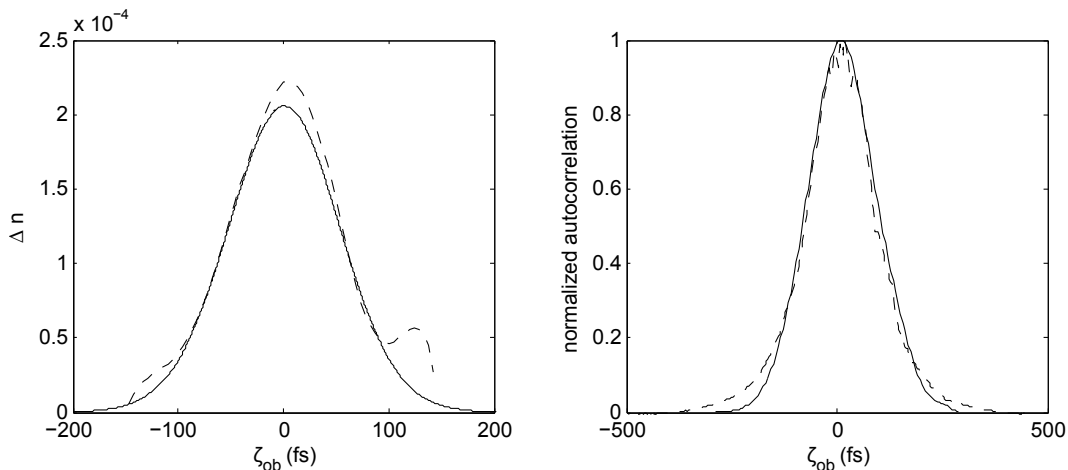


Figure 5.10: Direct comparison of measured and calculated longitudinal pulse profiles. **(a)** FDT reconstruction (solid line) and NLSE simulation (dashed line) of the longitudinal profile. **(b)** Autocorrelation trace calculated from FDT-reconstructed longitudinal profile (solid line) and direct measurement (dash line). Except for the direct autocorrelation measurement, the curves are lined out from Fig. 5.7 and 5.8 with $z_{\text{ob}} = 1.5$ mm, $x_{\text{ob}} = 0$, $E_{\text{pu}} = 0.6$ μJ .

reconstructions, as well as the absence of sharp-edged structures that were inserted into the phantom simulations to test stringently for reconstruction artifacts. We observe $d > 0.5$ in two places. First, frames that encompass the entrance ($t_{\text{ob}} < 2.5$ ps, $z_{\text{ob}} < 0.5$ cm) or exit ($t_{\text{ob}} > 12.2$ ps, $z_{\text{ob}} > 2.5$ mm) of the medium (not shown in Fig. 5.7a) yield larger d because of “edge artifacts” attributable to the sharp index discontinuity. When edge frames are omitted, we observe $d < 0.5$ for $0.4 \leq E_{\text{pu}} \leq 0.6 \mu\text{J}$ (compare 1st and 2nd rows of Table 5.1). Second, in the last two frames for $E_{\text{pu}} = 0.7 \mu\text{J}$, we observe $d > 0.5$. This is in part because the “real” pulse develops multiple filaments (Fig. 5.7c, bottom) that cylindrically-symmetric NLSE simulations fail to capture, even though FDT reconstructions capture a slice of them. Thus here a shortcoming

t_{ob} range	z_{ob} range	$E_{\text{pu}} = 0.4\mu\text{J}$	$0.5\mu\text{J}$	$0.6\mu\text{J}$	$0.7\mu\text{J}$
0 – 14.7 ps	0 – 3 mm	0.63	0.65	0.66	0.99
2.5 – 12.2 ps	0.5 – 2.5 mm	0.37	0.49	0.50	0.95
2.5 – 7.4 ps	0.3 – 1.5 mm	0.37	0.49	0.50	0.46

Table 5.1: RMS deviations of FDT reconstructions from NLSE simulations.

of the NLSE simulation, not the FDT reconstruction, contributes to larger d . The small index “hole” that appears at $z_{\text{ob}} = 2.5$ mm also contributes because it challenges FDT resolution in all 3 variables ($\zeta_{\text{ob}}, x_{\text{ob}}, z_{\text{ob}}$), and deviates in shape from the narrower (in x_{ob}), longer (in ζ_{ob}) negative-index plasma filament that appears in the corresponding NLSE simulation frame. Excluding these final two frames, $d < 0.5$ even for $E_{\text{pu}} = 0.7\mu\text{J}$ (3rd row of Table 5.1); including them, d exceeds that of the phantom 5-probe configuration III (see Fig. 5.4d) by only $\sim 25\%$. Despite locally enhanced d , the reconstruction captures the essential physical feature (a transient plasma filament), albeit with distorted shape. Thus direct comparison of Fig. 5.7a and Fig. 5.8a and RMS error analysis show that the reconstructions are not significantly corrupted by artifacts.

Figs. 5.8b,c, Fig. 5.9 and Fig. 5.10 highlight several specific areas of quantitative agreement. First, regarding transverse profiles, Fig. 5.9 compares (a) $\Delta x_{\text{ob}}(z_{\text{ob}})$ (FWHM) and (b) $\Delta n(0, 0, z_{\text{ob}})$ from reconstructions (data points) with NLSE-simulated values (solid curves). For $E_{\text{pu}} = 0.4, 0.5 \mu\text{J}$, they agree well for all z_{ob} ; for $E_{\text{pu}} = 0.6, 0.7 \mu\text{J}$, they agree up to the onset of multi-filamentation, beyond which solid calculated curves are drawn dotted. Fig. 5.8c directly compares the complete simulated (solid curves)

and reconstructed (dashed) transverse index profiles near the exit plane (for $E_{\text{pu}} = 0.4, 0.5, 0.6 \mu\text{J}$) or at the onset of multi-filamentation ($0.7 \mu\text{J}$), further illustrating the close agreement. Second, both simulated (Fig. 5.8a) and reconstructed (Fig. 5.7a) longitudinal profiles evolve negligibly (Fig. 5.10a), and agree with independent autocorrelation measurements (Fig. 5.10b) of incident and transmitted pulse duration, as expected for $L \ll L_{\text{dis}}$. Although longitudinal breakup of the pulse temporal envelope (“pulse splitting”) triggered by material dispersion [43, 68] or ionization [79, 87] has been observed in previous fs pulse filamentation experiments and simulations, and is an important mechanism in arresting self-focusing collapse [13], our NLSE simulations predict that pulse splitting would occur only for $z_{\text{ob}} > 0.3 \text{ cm}$ (for $E_{\text{pu}} = 0.7 \mu\text{J}$), beyond our sample length. Previous observations of fs pulse splitting in glass used higher power pulses [87] or longer propagation lengths [68] than our experiment. Third, simulated (Fig. 5.8b) and measured (Fig. 5.7b) output pump spectra show similar trends as E_{pu} increases. Specifically, the simulations reproduce the development of an asymmetric double-peaked spectrum for $E_{\text{pu}} \geq 0.6 \mu\text{J}$, caused by self-phase modulation. The asymmetry in the peaks is attributable to slight self-steepening, which otherwise plays a minor role since our sample length L is much less than the characteristic self-steepening length $L_{\text{ss}} = c\tau_{\text{pu}}/n_2I_{\text{pu}} \approx 15 \text{ cm}$ [7] for our conditions.

Beyond the point at which $0.6, 0.7 \mu\text{J}$ pumps lost cylindrical symmetry, the calculations, though no longer in quantitative agreement with the data, nevertheless mirror qualitative trends in the FDT images. For example,

for $E_{\text{pu}} = 0.7 \mu\text{J}$ and $z_{\text{ob}} > 2.0 \text{ mm}$, the calculated $\Delta n(0, 0, z_{\text{ob}})$ increases sharply to ~ 0.00065 before dropping equally sharply (Fig. 5.9b, black dotted curve) due to formation of an electron-hole plasma, which contributes a compensating negative index change. The measured $\Delta n(0, 0, z_{\text{ob}})$ increases to a lower maximum, then also drops (Fig. 5.9b, black data points). Here the calculated Δn evolves more quickly than the inter-frame resolution; thus (like the “dot” in the phantom simulations) the reconstruction “rounds off” the temporal or z_{ob} dynamics, partly explaining the discrepancy. Absence of multi-filamentation in the calculation also contributes to the discrepancy. The FDT images themselves provide additional insight. In this region, the steep-walled index “hole” appeared (see Fig. 5.7a, bottom right frame), inducing de-focusing and presumably pulse splitting in a longer medium [43, 68, 79, 87]. This hole had $\sim 10 \mu\text{m}$ diameter, significantly narrower than the $n_2 I_{\text{pu}}$ envelope (see Fig. 5.9d, solid curve). Such a narrow hole is consistent with the onset of multi-photon ionization, the mechanism that accounts for the drop in $\Delta n(0, 0, z_{\text{ob}})$ in our NLSE simulation. Six photons are needed to create an electron-hole pair in fused silica, so plasma generation rate scales as I^6 . Thus plasma concentrates in the center of the self-focused profile (Fig. 5.9d, dashed curve), and appears suddenly as I increases, consistent with the FDT images.

5.4.3 High-order nonlinear refractive index and electron-hole plasma ionization in laser-glass interactions

The relative importance of plasma defocusing [44, 64, 88] and negative electronic Kerr effect [3, 4, 20] in arresting the collapse of self-focusing pulses

has been debated extensively in connection with nonlinear pulse propagation in gaseous media. Although there has been comparatively little discussion of this issue for condensed media, a measured value $n_4 = -3.3 \times 10^{-28} \text{ cm}^4\text{W}^{-2}$ of the 4th-order Kerr coefficient of fused silica has been reported [20]. In view of this measurement, and the importance of nonlinear pulse propagation in fused silica in optical fiber communication and micro-machining, we considered the possibility that 4th-order Kerr effect might contribute to, or even dominate, the arrest of self-focusing under our conditions. There were three findings. First, our NLSE calculations that included 4th-order Kerr effect using the previously reported n_4 deviated significantly from all FDT data, even before the onset of multi-filamentation, as shown by the dashed curves in Fig. 5.9a,b. This n_4 actually induced self-defocusing under our conditions, contrary to observation. RMS deviation d between the NLSE calculations and the reconstructions (Fig. 5.7a) also grew to > 0.8 , even in regions free of edge artifacts and for $E_{\text{pu}} \leq 0.6 \mu\text{J}$, much larger than values in Table 1. Second, as an independent check of $|n_4/n_2|$, we conducted standard z-scan measurements of our silica plate’s nonlinear index [74]. Results, exemplified by Fig. 5.9c (circles), fit well to a nonlinear lens determined solely by $n_2 I_{\text{pu}}$ (solid curve). Our FDT and z-scan results both place an upper limit of $10^{-29} \text{ cm}^4\text{W}^{-2}$ on $|n_4|$. Third, we found that a negative 4th-order Kerr effect, even of limited value, broadly suppressed the positive $n_2 I_{\text{pu}}$ profile, rather than producing the observed narrow index hole that appeared at $t_{\text{ob}} = 12.2 \text{ ps}$ ($z_{\text{ob}} = 2.5 \text{ mm}$) for $E_{\text{pu}} = 0.7 \mu\text{J}$ (see Fig. 5.7a, 4th row, last panel). This is because it scales

as I_{pu}^2 instead of I_{pu}^6 , like plasma generation. Thus our results do not support an important role of a 4th-order Kerr effect. However, they do not rule out the possibility that a negative electronic Kerr effect of higher than 4th order contributes to forming this index hole.

In summary, FDT generalizes FDSC by applying multiple probe simultaneously, thus visualizing the evolving spatiotemporal profile of a light-speed index structure in a single shot for the first time. Compact methods to generate and detect these multiple probes were developed, making FDT only slightly more complicated than a standard pump-probe experiment. Conventional tomographic reconstruction algorithms were generalized and adapted to FDT. With improvements in probe bandwidth and imaging resolution, FDT could image laser wakefield accelerators. In particular, the FDSC data of Chapter 4 could be converted to tomographic movies of the complete plasma bubble profile by applying additional wide bandwidth probes at different angles.

Chapter 6

Multi-object-plane imaging over long interaction distance

The visualization methods discussed in preceding chapters are all based on the assumption that the depth of view of the imaging system that relays phase-modulated probe(s) from interaction region to detector exceeds the interaction length. This assumption enables simplifications such as Eq. (3.1) in relating measured phase shifts back to the index structure, but limits the interaction length to a few millimeters for object sizes ($\sim 10\mu\text{m}$) typical of intense laser-matter interaction experiments. This limit nevertheless covers a broad range of applications, including ultrafast laser material processing, laser-plasma proton/ion acceleration and electron acceleration up to ~ 100 MeV, and fast ignition. However, recent applications require much longer interactions. For example, femtosecond laser pulses form multi-meter-long self-guided filaments in air, which can be used for remote sensing [13]. Laser wake field acceleration with low plasma density (10^{17} cm^{-3}) yields multi-GeV electrons by elongating the acceleration distance to around 10 cm [89]. Electron-bunch-driven plasma wakefield accelerators use interaction length up to ~ 1 m [6, 36]. Such applications require a new approach to visualizing the structure and evolution of light-speed index objects over meter-scale interaction lengths.

6.1 Probe diffraction and the Rytov approximation

For arbitrary interaction length, a probe field E propagating in a non-dispersive medium with transient index perturbation Δn satisfies the equation

$$\frac{\partial E}{\partial z} = \frac{i}{2n_0k} \nabla_{\perp}^2 E + ik\Delta n E \quad (6.1)$$

where $k = 2\pi/\lambda_{\text{pr}}$ denotes the probe wave vector and n_0 is the refractive index of the unperturbed medium at the central wavelength of the probe. The first term on the right side describes diffraction of probe light, the second term the modulation of the probe profile by the index perturbation Δn . The first term becomes significant only when the propagation distance L exceeds the diffraction length $L_{\text{dif}}^{(\text{pr})} = \pi\sqrt{\Delta x^2 + \Delta y^2}/\lambda_{\text{pr}}$, where Δx and Δy represent the index structure size along transverse dimensions x and y . For $L < L_{\text{dif}}$, only the second term is important. The solution of Eq. (6.1) is then simply $E(z) = E(0) \exp(ik \int \Delta n dz)$, which immediately yields the simplified integral relations Eq. (2.11) for FDH or Eq. (3.1) for FDSC/FDT between accumulated probe phase shift and index profile Δn . Thus, in this limit, the probe is modified purely by phase accumulation, with no amplitude modulation.

For $L \geq L_{\text{dif}}^{(\text{pr})}$, Fresnel diffraction, described by the first term on the right side of Eq. (6.1), becomes significant, and both phase and amplitude profiles of the probe are modulated during its interaction with the index object. We can then write the probe field as $E = E_0 \exp \psi$, where E_0 is the unperturbed probe satisfying $\partial_z E_0 = (i/2n_0k) \nabla_{\perp}^2 E_0$, $\exp \text{Re}(\psi)$ describes its amplitude modulation, and $\exp \text{Im}(\psi)$ its phase modulation. Substituting this

field in Eq. (6.1), and assuming the probe beam is much wider than the index object, we get

$$\frac{\partial\psi}{\partial z} = \frac{i}{2n_0k} [\nabla_{\perp}^2\psi + (\nabla_{\perp}\psi)^2] + ik\Delta n, \quad (6.2)$$

with a nonlinear term. In order to linearize the reconstruction process, we use the Rytov approximation [16]

$$(\nabla_{\perp}\psi)^2 \ll 2n_0k^2\Delta n, \quad (6.3)$$

i.e. phase and amplitude modulation vary slowly over transverse distances of the order of λ_{pr} . Eqn. 6.3 describes interaction of probe and object over an effective distance L' for which a specific probe point overlaps with the index structure. For collinear pump and probe, $L' \approx L$. Since ψ increases with L' , a sufficiently long L could then enhance ψ beyond the Rytov limit. However, for pump and probe pulses whose paths intersect at small oblique angle θ , $L' \approx \sqrt{\Delta x^2 + \Delta y^2}/\theta$ can be considerably smaller than L , so Eqn. 6.3 is more easily satisfied. Thus by using a small pump-probe intersection angle θ , the evolution of an index structures over a long distance can be reconstructed *linearly*.

6.2 Multi-object-plane imaging (MOPI)

In this section, we describe an experiment that images an evolving light-speed index object over propagation distance $L \gg L_{\text{dif}}$ in a single shot. The object is the Kerr and plasma index profiles of an intense fs laser pulse as it forms a self-guided filament in air. The physics superficially resembles that

of a fs pulse propagating through glass, as described in the previous chapter. However, there are important differences in the details: the propagation distance is ~ 10 cm instead of 3 mm, the pump pulse is several mJ instead of $< 1\mu\text{J}$, the plasma lifetime is several ps instead of < 1 ps, and the Kerr index contains a delayed molecular rotational component as well as an instantaneous electronic component. To deal with probe diffraction, the modulated probe is imaged to each of several detectors from multiple object planes within the 10 cm interaction region, rather than just a single object plane at the exit of the medium as in FDH and FDT. Hence we call this approach multi-object plane imaging (MOPI). The concept can be compared to high-speed sports photography, which must be done with wide aperture optics for efficient exposure within brief shutter opening times, at the expense of a small depth of field. To achieve large depth of field, the sports photographer's MOPI solution would be to use multiple high-speed cameras, each one focused at a different object plane separated from that of its neighbor camera by a depth of field. Through computer processing, a composite photograph that is in focus over a large depth of field can then be assembled.

6.2.1 Experimental setup

In the experiment, a pump laser pulse (duration 70 to 140 fs, center wavelength 800 nm, energy 1 – 3 mJ) is focused to beam waist $w_0 \sim 63 \mu\text{m}$ in air, where it induces a Kerr index profile and a plasma channel of $< 1\%$ atmospheric density in its wake. A collimated and *fully compressed* probe pulse

($\sim 14 \mu\text{J}$, 70 to 140 fs duration) split from the pump crosses the interaction region at angle $\theta \sim 1^\circ$ with waist $\sim 3 \text{ mm}$ (see Fig. 6.1). In contrast to FDH, FDSC and FDT methods described in previous chapters, the probe pulse is NOT temporally stretched by chirping to illuminate the object's entire length. Instead, the compressed probe illuminates only a 70 to 140 fs longitudinal slice of the pump-generated structure at a specified time delay t behind the pump over a 10 cm path. Thus a single probe images the evolution of the transverse profile of a selected longitudinal slice of the object. To image the entire length of the object in one shot, additional probes with different delays t must be used. Alternatively, for stable filaments, t can be changed on different shots to build up a composite image. Here we demonstrate the latter approach, but there is no fundamental difficulty in implementing the former.

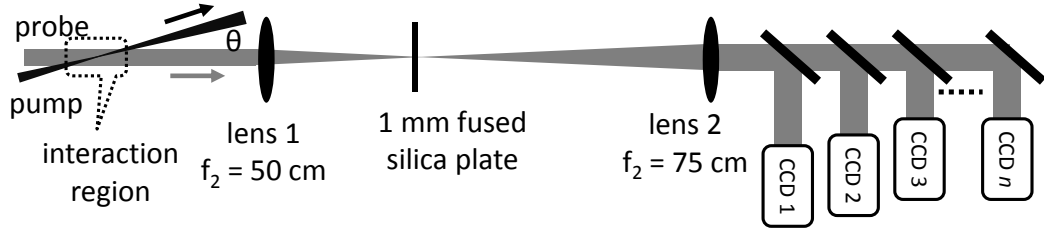


Figure 6.1: Schematic diagram of Multi-object-plane imaging setup. Here nonlinear phase contrast imaging is applied to resolve small phase shift induced by tenuous plasma in air.

The illuminated slice sweeps transversely across the probe profile with velocity $v_\perp = c \sin \theta \approx c\theta$, thereby mapping its index profile at propagation distance z onto transverse position x on the probe profile via the relation $x = z\theta$ (Fig. 6.2). Only index structures at $z = x/\sin \theta$ modulate the probe

at x ; thus in principle index structures at $z \neq x/\sin\theta$ do not affect the probe, provided θ is large enough.

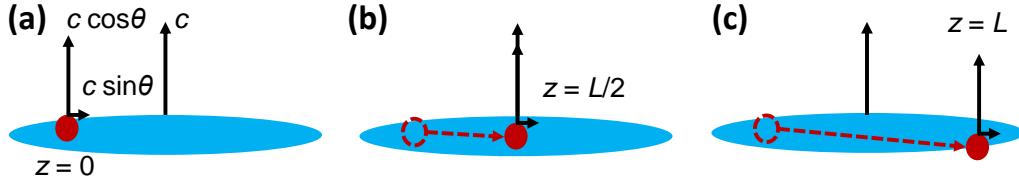


Figure 6.2: Schematic diagram of small oblique angle probe. Relative positions of pump induced index structure (red) and probe pulse (blue) at different propagation distance: **(a)** $z = 0$; **(b)** $z = L/2$; **(c)** $z = L$.

After the interaction, copies of the phase-modulated probe created by beam splitters are imaged through a $4f$ system ($f_1 = 50$ cm, $f_2 = 75$ cm) from multiple object planes (MOPs) at z_i ($i = 1, 2, 3, \dots$) along the pump path to corresponding image planes, where charge-coupled device (CCD) cameras recorded “bow-tie” shaped images (Fig. 6.3), in which the waists corresponds to object planes that are exactly imaged, the wider wings to nearby out-of-focus regions. These bow-tie images are, in essence, phase streaks as discussed in the previous three chapters, with three important differences. First, only one plane (corresponding to the waist) is in focus for each detector. A phase retrieval algorithm, discussed in the next section, must be applied to recover a complete in-focus composite streak from images projected from different object planes. Second, the phase modulation has been converted to amplitude modulation using a nonlinear phase contrast imaging (PCI) technique, discussed in Sec. 6.3. The amplitude modulation is recorded directly on the

CCDs without the use of a spectrometer or interferometry. This approach was chosen here because the present experiment, as well as target applications to multi-GeV plasma accelerators, involve tenuous ($n_e \sim 10^{17} \text{ cm}^{-3}$) plasmas that yield correspondingly small phase shifts. PCI can resolve phase shifts as small as ~ 10 mrad, beyond the resolving capability of interferometry by one order of magnitude. Moreover, for large phase shifts, amplitude modulation increases monotonically with phase shift, avoiding 2π phase wrapping problems that arise in interferometry and two-dimensional holography. Third, the streaks record a time sequence of the transverse profiles of just a single longitudinal slice of the object, rather than projections of the entire object as in FDSC and FDT.

6.2.2 Phase retrieval from multi-object-plane images

The probe pulse crossing the interaction region accumulates phase shift $\phi(\zeta, y, z) = (2\pi/\lambda_{\text{pr}} \sin \theta) \int \Delta n(\zeta, x, y, z) dx$ at specific propagation position z , and induces diffraction pattern at $x = z \sin \theta$ only, requiring a minimum probe angle θ_{min} . To resolve two evolution events separated by a propagation distance of Δz , $\Delta x \approx \theta \Delta z$ should exceed the transverse size σ_x of both the index object and of the Fresnel diffraction pattern due to the propagation along Δz . For example, an index object propagating at z_1 perturbs the probe profile at $x_1 = \theta z_1$ by introducing amplitude modulation $\delta E(z_1) = \delta \exp \{ -[(x - x_1)^2 + y^2]/w_0^2 \}$.

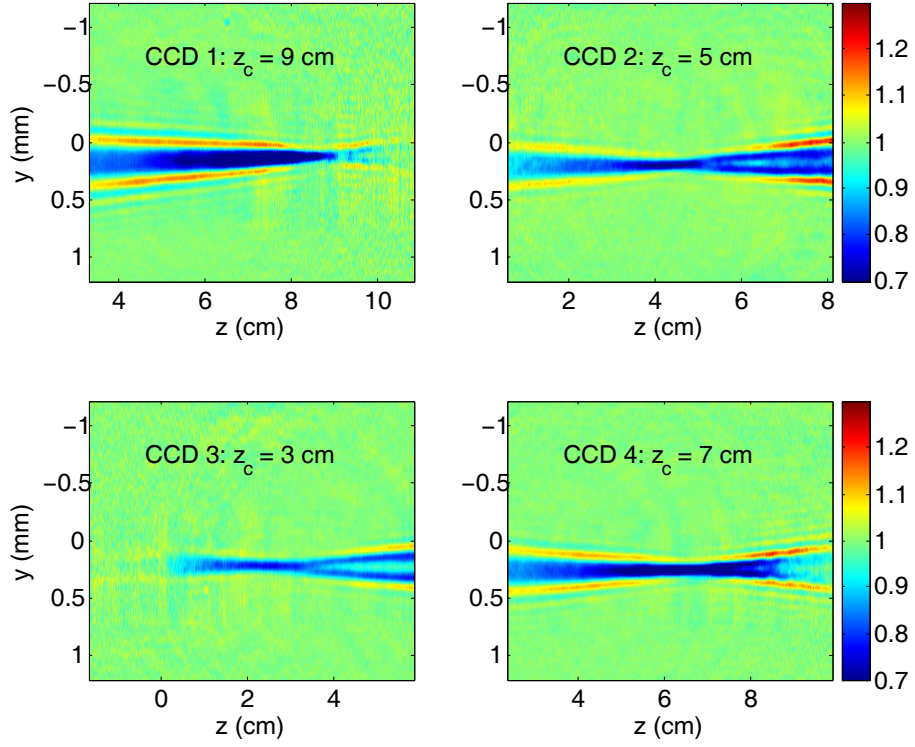


Figure 6.3: Multi-object-plane imaging raw data. Intensity modulation of a probe at delay $t = 1.7$ ps behind a 3 mJ pump imaged from object planes at $z_i = 3, 5, 7,$ and 9 cm, as captured by four CCD cameras. Color scales indicate probe relative intensity modulation.

Thus the field after propagation to $z_2 = z_1 + L$ is

$$\begin{aligned} \delta E(z_2) &= \mathcal{F}\mathcal{F}\mathcal{F} \left\{ \mathcal{F}\mathcal{F}\mathcal{F} [\delta E(z_1)] \exp \left[-\frac{i\lambda L}{4\pi} (k_x^2 + k_y^2) \right] \right\} \\ &= \frac{\delta}{1 + i\lambda L/\pi w_0^2} \exp \left\{ -\frac{(1 - i\lambda L/\pi w_0^2) [(x - x_1)^2 + y^2]}{w_0^2 [1 + (\lambda L/\pi w_0^2)^2]} \right\}. \end{aligned} \quad (6.4)$$

Thus the maximum transverse size of the diffraction pattern is $w_0 \sqrt{1 + (\lambda L/\pi w_0^2)^2}$.

It should be considerably smaller than the actual transverse shift $L \sin \theta$ along the x direction, in order to resolve evolution of the index structure. For any propagation length, this criteria sets a limit $L \sin \theta \gg \lambda L/\pi w_0$. Thus the

probe angle must satisfy

$$\theta \gg \theta_{\min} = \frac{\lambda}{\pi w_0}. \quad (6.5)$$

In the experiment, $\lambda = 800$ nm, $\sigma \sim 100$ μm , so Eq. (6.5) yields $\theta_{\min} \sim 0.14^\circ$. Thus the chosen $\theta \approx 1^\circ$ satisfies the condition for the minimum probe angle.

A corollary of Eq. (6.5) is the quasi-1D diffraction of the index structure along the y -direction within the probe transverse profile, which is responsible for the flared parts of the “bow-tie” profiles in Fig. 6.3. From a naive application of the Huygens-Fresnel principle, the diffracted wave from an object confined in both x and y dimensions spreads out in both x and y directions. Thus it might appear at first sight that the bow-tie flare at a given x_2 would include contributions from diffracted waves originating from z positions corresponding to neighboring $x_1 \neq x_2$. However, the criterion (6.5) dictates that such diffracted waves cannot catch up with the transverse movement of the index object itself when $\theta > \theta_{\min}$. Even if the object were to propagate to L' , so that the diffraction pattern of phase perturbation at x_1 reached x_2 , the disturbed field is $\delta E_2 \sim (\pi w_0^2 \delta / \lambda L') \exp(-\pi^2 w_0^2 (x_2 - x_1)^2 / \lambda^2 L'^2) \exp(-\pi^2 w_0^2 y^2 / \lambda^2 L'^2)$. Even though the first exponential function may not vanish if $L' \gg (x_2 - x_1) / \sin \theta$, the contribution of diffraction pattern from z_1 is a flat background with a broad width $\Delta y \sim \lambda L' / \pi w_0 \gg w_0$ along the y -direction and amplitude (*i.e.* $\delta L'^{-1}$), which is negligible. Thus the diffraction pattern at x_2 is only contributed locally by the index structure at z_2 , like a beam diffracted by a string whose cross-section is the same as the index structure’s transverse profile at

x_2 or z_2 . The equation governing probe propagation and diffraction

$$\frac{\partial E}{\partial z} = \frac{i\lambda}{4\pi} \nabla_{\perp}^2 E + \frac{2\pi i}{\lambda} \Delta n(z) E \quad (6.6)$$

thus reduces to a quasi-1D version at specific x :

$$\frac{\partial E}{\partial z} = \frac{i\lambda}{4\pi} \frac{\partial^2 E}{\partial y^2} + \frac{2\pi i}{\lambda} \Delta n(z) \delta\left(z - \frac{x}{\theta}\right) E. \quad (6.7)$$

This quasi-1D simplification decouples phase shift reconstruction at different x transverse positions, enabling one-dimensional reconstruction of the phase shift ϕ line-by-line at different x using the Gerchberg-Saxton algorithm [24].

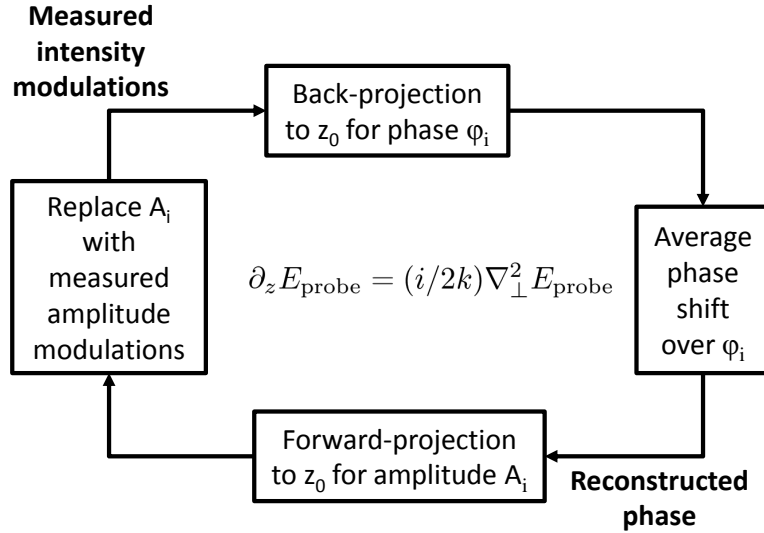


Figure 6.4: Schematic diagram of iteration procedure in the Gerchberg-Saxton algorithm.

The Gerchberg-Saxton algorithm for retrieving phase shift from amplitude modulation on multiple object planes z_i is illustrated in Fig. 6.4. In

experiments, probe amplitudes with modulations at different propagation positions z_i are measured without phase shift information. In order to calculate $\psi(y, z)$ at z , all these phase profiles are set to zero at the beginning, and the complete probe fields with amplitude and phase propagates from z_i to z based on Eq. 6.7, yielding electric field $E_i(y, z)$ at z from different z_i . Then the mean value $\bar{E}(y, z) = (1/N) \sum_i E_i(y, z)$ is set as the electric field at z where N is the number of cameras, or the number of object planes. The mean field $\bar{E}(y, z)$ then back-propagates to each z_i position with electric field $E_i(y, z_i)$. Finally the amplitude $|E_i(y, z_i)|$ is replaced by the measured probe amplitude modulation $A_i(y)$. Thus the loop is closed in one step of the iterations. In each iteration step, the error of reconstruction ϵ is calculated through

$$\epsilon = \sqrt{\sum_i [|E_i(y, z_i)| - A_i(y)]^2}. \quad (6.8)$$

Typically after 200 to 300 iterations, the error ϵ converges to zero and the phase shift imprinted on the probe can be obtained from $\psi(y, z) = \arg [\bar{E}_i(y, z)]$.

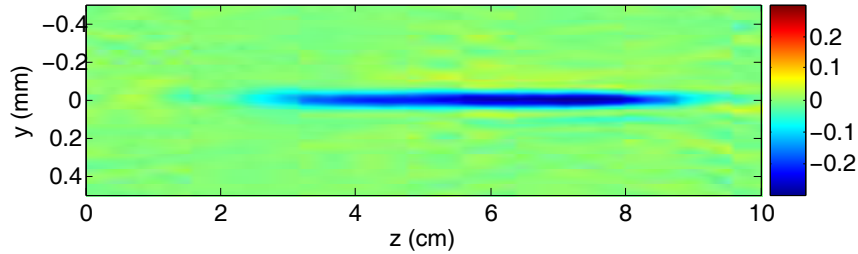


Figure 6.5: Reconstructed phase shift of plasma channel from multi-object-plane amplitude modulation. The color scale denotes the original phase shift.

As an example, Fig. 6.5 shows the reconstructed phase track of a probe that propagated 1.7 ps behind the pump pulse by analyzing amplitude mod-

ulations captured by four CCD cameras shown in Fig. 6.3. With this delay, pump-induced plasma was entirely responsible for probe phase shift. Indeed this image matched a plasma fluorescence image recorded from the side. If we assume the plasma filament is cylindrically symmetric, Abel inversion analysis yields electron density $n_e \approx 10^{16} \text{ cm}^{-3}$ (0.03% atmospheric density). The high signal-to-noise ratio (~ 20) implies that plasma density fluctuations $\Delta n_e < 10^{15} \text{ cm}^{-3}$ could be imaged in a single shot. This high sensitivity originates partly from our conversion of phase to intensity modulations, without the need to resolve fringe shifts. Moreover, compared to transverse probe techniques [1, 9, 70], the small probe angle lengthens overlap time of probe and object, magnifying the phase shift induced by tenuous plasma structures.

6.3 Nonlinear phase contrast imaging and schlieren for high sensitivity and robustness

To image tenuous plasma or other faint refractive index structures, a phase contrast imaging (PCI) procedure can be applied [93]. In conventional PCI of a small phase shift ($\phi < 0.4 \text{ rad}$) [90], a tiny quarter wave phase plate is placed on the focal spot of the first imaging lens 1 in Fig. 6.1. The probe field carrying phase shift $\exp(i\phi) \approx 1 + i\phi$ can be conceptually divided into an intense unperturbed part (corresponding to the factor 1) that focuses tightly onto the wave plate, and thus experiences a $\pi/2$ phase shift, and a weak diffracted part (corresponding to the factor $i\phi$) that does not focus tightly, and thus bypasses the wave plate. As a result, the measured probe has intensity

$|i + i\phi|^2 \approx 1 + 2\phi$, *i.e.* phase is mapped linearly to intensity modulation, which can be measured with high sensitivity. However, for probe pulses derived from large laser systems such as ours, the pointing direction of the probe beam is not stable enough to reliably hit the tiny phase shifter, which is as small as the focal spot size.

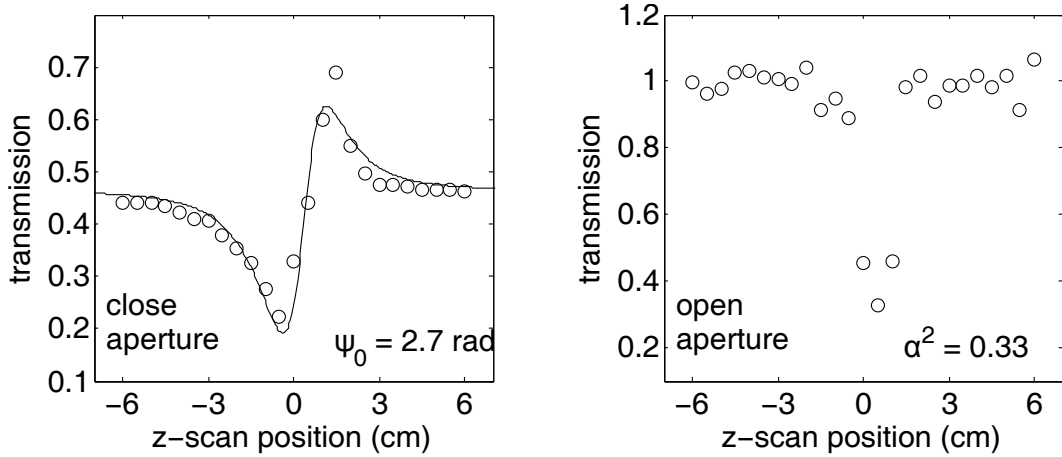


Figure 6.6: Calibration of nonlinear phase shift and absorption in the nonlinear Kerr medium using close (left) and open (right) aperture z-scan measurements. The Kerr medium is a 1-mm thick fused silica glass at the focal plane of the 4- f imaging system shown in Fig. 6.1.

To implement robust PCI, we used a nonlinear Kerr effect by placing a 1mm fused silica plate at the Fourier plane of the 4 f imaging system, where it preferentially induced Kerr phase shift ψ_0 and nonlinear absorption α on the portion of the probe light that was unperturbed by the object, and thus focused tightly in the plate. The value of ψ_0 and α can be directly measured through closed- or open-aperture z-scan [74] as shown in Fig. 6.6. These measurements yielded $\psi_0 = 2.7 \text{ rad}$ and $\alpha = 0.57$ for the unperturbed probe.

After collimation by lens 2, the actual probe phase shift on the image plane becomes ψ , as discussed further below. The unperturbed probe part $\alpha \exp(i\psi)$ interferes with the signal part $i\phi$, yielding a modulated intensity profile

$$I \propto 1 + \frac{2 \sin \psi}{\alpha} \phi \quad (6.9)$$

There are two advantages to this nonlinear implementation of phase contrast imaging: (1) nonlinear absorption accompanies phase shift, thereby improving sensitivity, as in dark field schlieren imaging; (2) by avoiding the conventional use of a micron-size phase shifting plate or needle tip absorber to induce ψ_0 and/or α , nonlinear optical processes increase the robustness of the system to probe beam-pointing instability. The nonlinear phase shift ψ and nonlinear absorption α can be adjusted by varying the probe energy, thus the probe intensity modulation is a function of the probe energy.

The relation between ψ_0 and ψ is derived by assuming that the probe has a Gaussian transverse profile $E_0 \sim \exp[-(x_0^2 + y_0^2)/w_0^2]$. Thus at the focal plane of the $4f$ imaging system, the field is $E_1 \sim \exp[-k_0^2 w_0^2 (x_1^2 + y_1^2)/4f_1^2]$ by Fourier transformation. At the fused silica plate, probe-intensity-dependent phase shift is induced with Gaussian shape. The transmitted field is then

$$\begin{aligned} E'_1 &\sim \exp\left[-\frac{k_0^2 w_0^2 (x_1^2 + y_1^2)}{4f_1^2}\right] \exp\left\{i\psi_0 \exp\left[-\frac{k_0^2 w_0^2 (x_1^2 + y_1^2)}{2f_1^2}\right]\right\} \\ &= \sum_{m=0}^{\infty} \frac{(i\psi_0)^m}{m!} \exp\left[-\frac{(2m+1)k_0^2 w_0^2 (x_1^2 + y_1^2)}{4f_1^2}\right]. \end{aligned} \quad (6.10)$$

Here the Taylor expansion of exponential function, i.e. $e^x = \sum_{m=0}^{\infty} x^m/m!$, is

applied. The field at the image plane is another Fourier transform of E'_1 :

$$E_2 \sim \sum_{m=0}^{\infty} \frac{(i\psi_0)^m}{m!(2m+1)} \exp\left[-\frac{f_1^2/f_2^2}{2m+1} \frac{x_2^2 + y_2^2}{w_0^2}\right]. \quad (6.11)$$

Generally the probe beam size is large enough that the area disturbed by the pump induced index structure shows no significant intensity variations, i.e. $x_2, y_2 \ll w_0$ in the interesting signal area. So this almost constant field is $E_2(x_2 = 0, y_2 = 0) = \sum_{m=0}^{\infty} (i\psi_0)^m / m!(2m+1)$, and the phase shift at the image plane induced by the nonlinear Kerr effect in the glass plate is

$$\psi = \arg \left[\sum_{m=0}^{\infty} \frac{(i\psi_0)^m}{(2m+1)m!} \right]. \quad (6.12)$$

As an simple, empirical estimate of ψ from z-scan measured ψ_0 , we assume $\psi_0 \ll 1$ so that high order terms in Eq. (6.12) are terminated and the sum is reduced to $1 + i\psi_0/3 \approx \exp(i\psi_0/3)$. So we have a simple relation $\psi = \psi_0/3$. Even for $\psi_0 \sim 1$ or larger than 1, this relation still holds because the series in Eq. (6.12) converges even faster than an exponential function. For example, in the experiment, the measured ψ_0 at the focal plane is 2.7 rad, and the phase shift on the image plane is 0.83 rad, roughly one-third of ψ_0 .

6.4 Multi-object-plane phase-contrast imaging of laser filaments in air

Figure 6.5 illustrates a plasma channel 1.7 ps after the driving pulse. This plasma lives for tens of picoseconds before recombining. To observe the key laser-air interaction dynamics that lead to formation of long self-guided

filaments, the pump-probe delay should be varied in the vicinity of pump-probe temporal overlap.

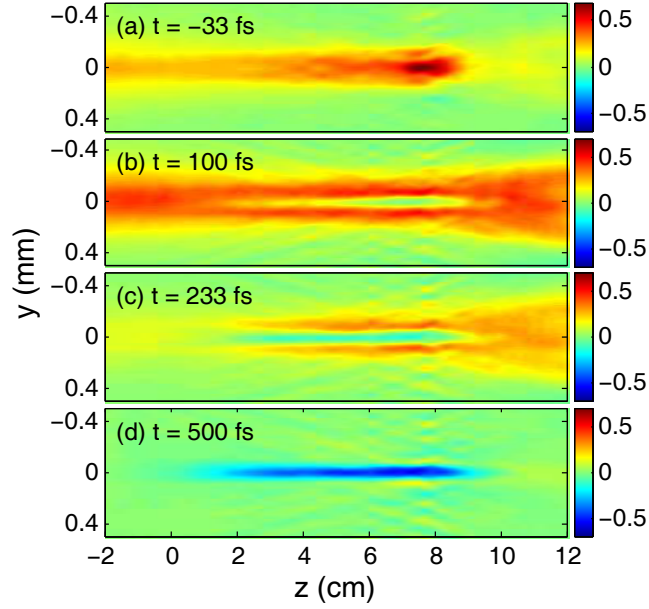


Figure 6.7: Four single-shot measurements of the z -evolution of the transverse index profile behind a 3 mJ pump focused in air, with probe at indicated time delays: (a) pump leading edge, where a positive electronic Kerr effect dominates; (b) pump trailing edge, where a negative plasma contribution is superposed on the electronic Kerr profile; (c) a molecular rotation time behind the pump, where the plasma contributions is superposed on a weaker delayed Kerr profile; (d) further behind the pump, where only plasma contributes. Color scales give probe phase shift in rad.

Fig. 6.7 presents four single-shot multi-object-plane phase contrast imaging (MOP-PCI) measurements of the continuous probe phase shift profiles $\Delta\phi_{\text{pr}}(z, y)$ at delays $t =$ (a) -33 fs, (b) 100 fs, (c) 233 fs and (d) 500 fs behind the peak of a 3 mJ, 140 fs pump pulse focused in air. For the data in Fig. 6.7(a), the probe overlapped the leading edge of the pump pulse, which

self-focused as it propagated. The phase shift originated mainly from the instantaneous electronic Kerr effect, yielding a positive phase-shift that increased monotonically in amplitude up to $z \sim 8$ cm, after which it weakened due to nonlinear absorption and ionization. For the shot in Fig. 6.7(b), the probe overlapped the trailing edge of the pump. Here the positive electronic Kerr contribution was still present, but plasma that grew in density in the trailing edge of the pump burned a deep, narrow negative index “hole” into the center of the wider positive transverse phase profiles over the interval $2 < z < 9$ cm. The plasma channel is relatively narrow because only the intense central part of the pump can effectively ionize the air, and such channel defocused the pump like a negative lens. Moreover diffraction of the pump trailing edge from the plasma filament widened and transversely modulated the background positive Kerr profile compared to the data in (a). For the shot in Fig. 6.7(c), the probe trailed approximately one molecular rotation time behind the pump. Here the instantaneous Kerr effect was no longer present, but a delayed molecular-rotation Kerr effect created a weak, broad positive index profile, still superposed on the narrow axial index hole of the long-lived plasma. At later delays (Fig. 6.7(d)), only the negative plasma contribution is present. The Kerr/plasma dynamics illustrated in Fig. 6.7 has been extensively studied in the context of laser filament formation in air (see *e.g.* Ref. [13, 88] and references therein). The new contribution here is to visualize the z -evolution of the associated index profile at each t over the entire propagation length in a single shot with good signal-to-noise ratio. If necessary, multi-

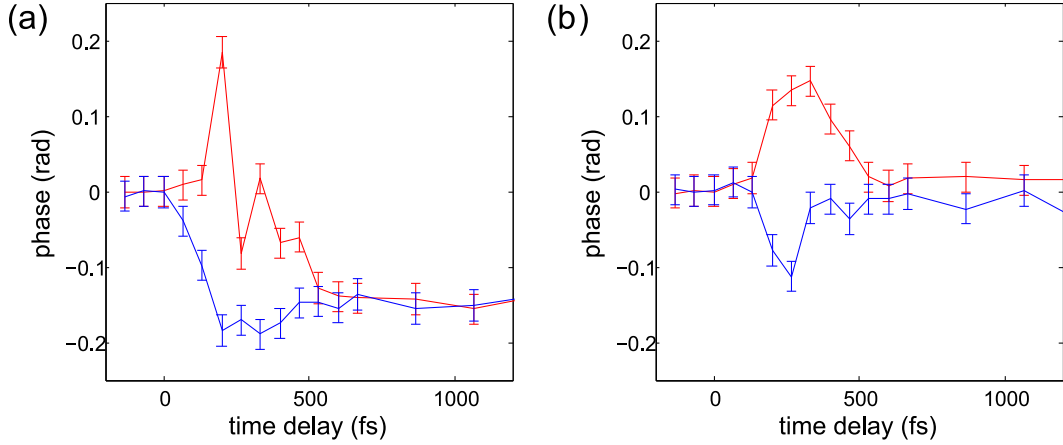


Figure 6.8: Probe phase shift at $z = 7.5$ cm versus pump-probe time delay on axis (a) $y = 0$ or off axis (b) $y = 100 \mu\text{m}$. Different probe polarizations are applied. Red: $\mathbf{E}_{\text{pu}}//\mathbf{E}_{\text{pr}}$; blue: $\mathbf{E}_{\text{pu}} \perp \mathbf{E}_{\text{pr}}$

object-plane phase contrast imaging can be multiplexed straightforwardly to visualize evolution at several t in one shot, rather than in separate shots as in Fig. 6.7(a)-(d), by propagating several probes with different t along separate small- θ paths through the interaction region, then imaging each to different areas of the CCDs or to separate CCD arrays.

By taking multiple shots with different pump-probe delays t , the evolution of the index structure $\phi(\zeta, y, z) \propto \int \Delta n(\zeta, x, y, z) dx$ was obtained. Fig. 6.8 showed the temporal profile of the index structure at $z = 7.5$ cm, both on axis ($y = 0$, a) and off-axis ($y = 100 \mu\text{m}$, b). Meanwhile the probe polarization was also adjusted to either parallel (red) or perpendicular (blue) to the linearly polarized pump. Nonlinear refractive index and plasma generation contribute to the probe phase shift. The former has an instantaneous electronic component ϕ_{inst} and a delayed molecular rotation component

ϕ_{rot} . For co-polarized pump and probe (red), positive instantaneous ($t = 0$) and positive time-delayed ($t \sim 300$ fs) Kerr index shift is resolved because $\phi_{\parallel} = \phi_{\text{inst}} + \phi_{\text{rot}}$. For crossed-polarized pump and probe (blue), the phase shift equals $\phi_{\perp} = \phi_{\text{inst}}/3 - \phi_{\text{rot}}/2$ because of the nonlinear susceptibility tensor's isotropic property of nitrogen or oxygen in air. Thus negative time-delayed ($t \sim 300$ fs) phase shift in blue curves is observed (Fig. 6.8). Comparing Fig. 6.8a and b, phase shift on axis after $t > 500$ fs showed a stable negative value ~ -0.15 rad, however the off-axis phase shift relaxes to zero. This is because the plasma channel ionized by the pump laser pulse can only be generated near the optical axis.

6.4.1 Multi-object-plane imaging resolution

In each shot in Fig. 6.7, the reconstructed phase at a specific longitudinal delay t shows the history of the index structure's transverse profile $\phi(y, z) = (2\pi/\lambda \sin \theta) \int \Delta n(t, x, y, z) dx$, with resolution limits on measuring fine structures along longitudinal t -direction and transverse y -direction. The longitudinal t -resolution is determined by the probe pulse duration since the probe selects the specific slice of the index structure along longitudinal t -direction and its duration determines the accuracy. On the other hand, the transverse y -resolution depends on the numerical aperture, or f -number, of the imaging lenses, as for other imaging techniques.

Multi-object-plane imaging also resolves the evolving index structure at different propagation distance z . Limits to resolving events within a short

distance Δz constitutes the z -resolution. The z -resolution is determined by the transverse size of the object along x and by diffraction from nearby structures. A point at x of the probe profile overlaps with an object of transverse size σ for time $\sigma/c\theta$, during which the object propagates $\Delta z \sim \sigma/\theta$. Thus the phase shift at x averages the object's evolution over Δz , defining one contribution to z -resolution. In addition, light diffracted from $x \pm \sigma$ or beyond can contribute to the phase at x . However, if the probe angle is larger than the minimum θ_{\min} , the diffraction contribution on z -resolution becomes negligible.

6.5 Tilted probe pulse front for pump–probe walk-off compensation

A subtlety of single- t MOPI data such as Fig. 6.7 is that the component of the object's velocity along the probe propagation direction is $v_{\parallel} = c \cos \theta$, slightly smaller than the probe speed c . Thus as the probe propagates from $z = 0$ to L , the index structure gradually lags behind, accumulating time delay walk-off $\Delta t = L(1 - \cos \theta)/c \approx L\theta^2/2c$. To maintain well-defined delay t , Δt should be smaller than probe duration τ_{pr} , thus setting an upper limit of the probe angle

$$\theta < \theta_{\max} = (2c\tau_{\text{pr}}/L)^{1/2}. \quad (6.13)$$

For $\tau_{\text{probe}} \sim 100$ fs and $L \sim 10$ cm, $\theta_{\max} \sim 1.4^\circ$. Thus t remained well-defined for the data in Fig. 6.7.

However, in experiments requiring longer L , shorter τ_{pr} , or larger θ (*e.g.* to improve z -resolution or to reduce pump scatter into the probe line), time

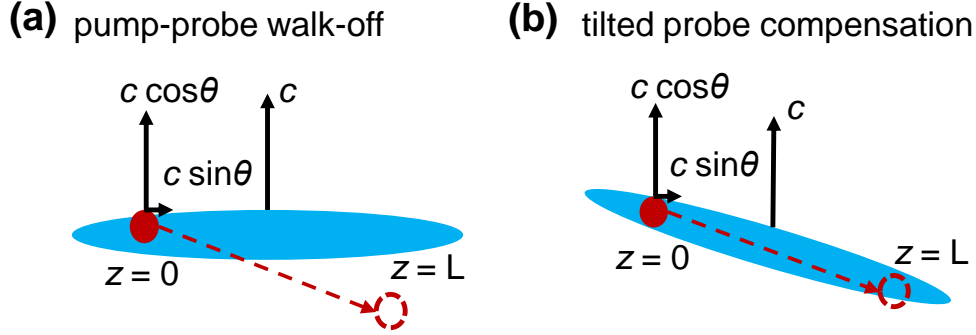


Figure 6.9: Schematic diagram of probe pulse tilting for pump-probe walk-off compensation. (a) Pump-probe walk-off for probe angle larger than θ_{\min} . (b) Walk-off compensation through tilting the pulse front of the probe.

delay walk-off could limit MOPI measurements. In such cases, time delay walk-off can be compensated straightforwardly by tilting the intensity front of the probe pulse by angle $\theta/2$, as shown in Fig. 6.9. A specified delay t of the object then remains perfectly overlapped with the same longitudinal position of the probe intensity profile throughout the propagation length. As a numerical example, a probe tilted by a prism with angular dispersion $0.05 \text{ rad}/\mu\text{m}$ enables probe angle as large as $\theta = 4.6^\circ \sim 3\theta_{\min}$ without walk-off. Moreover, angular dispersion of the probe is negligible as long as L remains much smaller than a critical length $L_c = \pi c^2 \tau_{\text{pr}}^2 / \lambda \tan^2(\theta/2) \approx 9 \text{ m}$.

The critical length L_c is limited by the spatiotemporal broadening of the probe after the angular dispersive optics such as prism and grating. Consider a Gaussian pulse $E(x, t) = E_0 \exp(-x^2/\sigma^2 - t^2/\tau^2)$ with its frequency domain expression as $\tilde{E}(x, \omega) = (E_0 \tau / 2\sqrt{\pi}) \exp(-x^2/\sigma^2 - \omega^2 \tau^2 / 4)$. The dispersive optics introduces extra phase $k\omega x(\partial_\omega \alpha)$, where $\partial_\omega \alpha$ is the angular dispersion

of the optics. After propagation for L in free space, the probe pulse finally becomes

$$\begin{aligned}
E(x, t) &= \frac{E_0 \tau \sigma}{4} \int \exp \left[- \left(k_x - k \frac{\partial \alpha}{\partial \omega} \omega \right) \frac{\sigma^2}{4} - \frac{\omega^2 \tau^2}{4} - \frac{ik_x^2 L}{2k} \right] e^{ik_x x} e^{-i\omega t} dk_x d\omega \\
&= E_0 \exp \left[-\frac{x^2}{\sigma^2 + 2L/k} \right] \exp \left\{ - \left[\tau^2 + \frac{2k^2 \sigma^2 L (\partial_\omega \alpha)^2}{k\sigma^2 + 2L} \right]^{-1} \left[t - \frac{k^2 \sigma^2 \partial_\omega \alpha x}{2L + k\sigma^2} \right]^2 \right\} \quad (6.14)
\end{aligned}$$

Thus Eq. (6.14) demonstrates that the probe pulse is tilted by an angle $\tan \gamma = \omega \partial_\omega \alpha (1 + 2L/k\sigma^2)^{-1} \approx \omega \partial_\omega \alpha = \lambda \partial_\lambda \alpha$, and the dispersion of the prism or grating can be chosen to fit the probe angle to achieve $\gamma = \theta/2$. Meanwhile, the probe experiences significant pulse broadening as the propagation L increases from τ to $\sqrt{\tau^2 + 2kL(\partial_\omega \alpha)^2(1 + 2L/k\sigma^2)^{-1}}$. In order to reduce the pulse broadening and maintain longitudinal t -resolution, the condition that $\tau^2 \gg 2kL(\partial_\omega \alpha)^2$ should be satisfied, setting the critical propagation distance

$$L \ll L_c = \frac{\pi c^2 \tau^2}{\lambda \tan^2(\theta/2)} \quad (6.15)$$

To illustrate walk-off compensation, we repeated the experiment with normal and tilted probe pulses of 70 fs duration and $\theta = 2.5^\circ$, which exceeded $\theta_{\max} = 1.2^\circ$ for $L = 10$ cm. Fig. 6.10a shows results at selected t for a normal probe. A probe whose peak ($t_i = 0$) overlapped the pump-induced index object initially at $z \approx 0$ outran the object within 2 cm, yielding a phase streak only 2 cm long (Fig. 6.10a, top panel). For larger initial delays ($t_i = 66$ and 133 fs), the probe outran the object at progressively larger z , yielding progressively longer streaks (lower 2 panels). In all of these cases, the probe overlapped the object at a drifting delay $t = t_i - z/c \cos \theta$. Fig. 6.10b shows results for

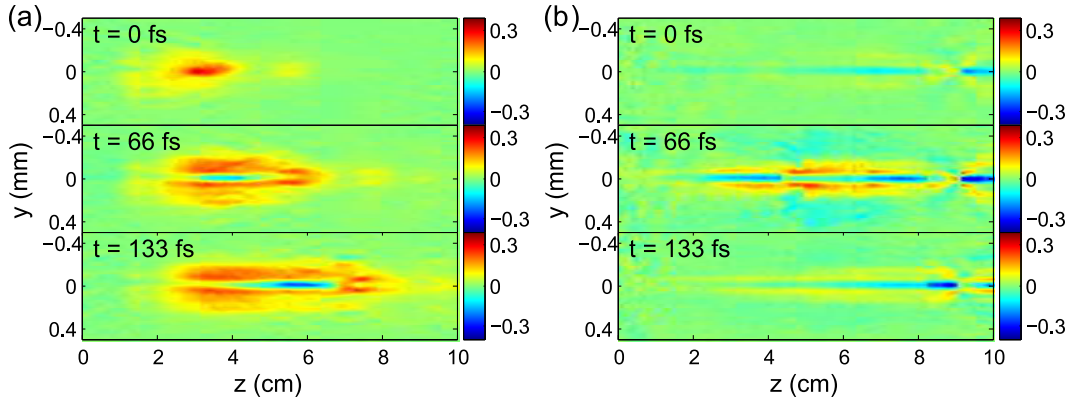


Figure 6.10: (a) Single-shot phase profiles with different pump-probe delays, showing effect of object-probe walk-off; (b) as in (a), but with optimally tilted probe, showing walk-off compensation, and color scales in (a-b) gives probe phase in rad.

an optimally tilted probe. In this case, all phase streaks were ~ 10 cm long, because the tilted probe overlapped the object at constant $t = t_i$ throughout the interaction.

In summary, multi-object-plane imaging measures the evolution of the transverse profile of light-speed index structures with high sensitivity over ≥ 10 cm path lengths at a specific time delay behind the drive pulse in a single shot. This method is uniquely suited to visualizing structures with low index contrast propagating over long paths with significant shot-to-shot variations or low repetition rate. It can be generalized to full 4D single-shot visualization by using multiple probes.

Chapter 7

Petawatt laser driven wakefield acceleration and its optical diagnosis

In Chapter 4, plasma wake structures were imaged in a laser wake field accelerator (LWFA), driven by ~ 40 TW laser pulses, that produced ~ 100 MeV electron beams. Multi-TW laser pulses have accelerated electrons to as high as ~ 1 GeV within a ~ 1 cm long preformed plasma channel [48]. Such electron beams were used to generate coherent x-ray beams [42]. These experiments were restricted to plasma electron densities $n_e > 10^{18}$ cm $^{-3}$ at which terawatt laser pulses could resonantly excite a wake and inject plasma electrons into it. However, the maximum electron energy is inherently limited to ~ 1 GeV within this density regime by dephasing between accelerating electrons and the plasma wakefield, and by depletion of the laser pulse.

Our group recently demonstrated a multi-GeV laser plasma accelerator [89]. From computer simulations, general requirements for multi-GeV LWFAs are well known. First, the LWFA should operate in a “blowout” regime. Both numerical modeling [53] and experimental diagnostics [18] have shown that bubble formation is essential for producing collimated, quasi-monoenergetic electron beams. Second, plasma density must be reduced to $n_e < 10^{18}$ cm $^{-3}$

to increase dephasing length L_D and pump-depletion length L_{PD} to multiple centimeters, factors that more than compensate for the slightly weaker accelerating field $E_z \propto \sqrt{n_e}$ at lower density. Third, laser peak power P must be kept well above the critical power $P_{cr} = 17\omega_0^2/\omega_p^2$ GW for relativistic self focusing. Here ω_0 is the laser frequency and $\omega_{cr} \propto \sqrt{n_e}$ is the plasma frequency. This enables the drive pulse to self focus and self compress during its initial non-linear interaction with the plasma, increasing its intensity to a level at which blowout occurs, and helps it to self-guide over multiple Rayleigh lengths once acceleration begins, thereby exploiting the increased acceleration length set by L_D and L_{PD} . For n_e in the low 10^{17} cm⁻³ range, the power must therefore approach 10^{15} W, or 1 petawatt (PW), a capability that is just emerging from recent advances in laser technology [27].

7.1 Petawatt laser driven plasma accelerators for electron and x-ray generation

Using the Texas Petawatt Laser at peak power of 1.1 PW [27], our laser wakefield acceleration experiments demonstrated quasi-monoenergetic electron beam with peak energy up to 2 GeV and maximum energy up to 2.3 GeV. Our results also showed that the highest electron energy (2 GeV) was achieved in a narrow range of plasma density (4 to 6×10^{17} cm⁻³). It is shown that self-injection and multi-GeV acceleration occur despite a irregular transverse laser profile outside the focal volume for long interaction length. In addition, the highly collimated electron beam with sub-milliradian (FWHM) divergence

angle and unprecedented pointing stability, justifying the application of the quasi-monoenergetic multi-GeV electron sources for collider and coherent light source [89].

7.1.1 Generation and measurements of 2 GeV electrons

Figure 7.1 shows a schematic layout of the experiments. Linearly polarized pulses from the Texas Petawatt Laser (duration $\tau \sim 150$ fs, wavelength $\lambda = 1.057 \mu\text{m}$, energy $E_{\text{laser}} \leq 150$ J)[27] were focused with f -number ($f\#$) 47 into the 1.5 mm radius entrance aperture of a 9-cm-long gas cell, which was pulse-filled with 1 to 8 Torr helium (He) of 99.99% purity. Transversely scattered pump light was imaged through a side window in the cell. Accelerated electrons emerged through a 3-mm radius exit aperture and were deflected in a plane perpendicular to the laser polarization by a magnetic field from a permanent dipole magnet. This field is profiled with 1% accuracy using a Hall probe, and the effective field was used in calculating electron trajectories. A high-sensitivity image plate (hereafter IP_{HS}) detected undeflected betatron X-rays and energy-dispersed electrons of energy $E > 0.5$ GeV at the end of an evacuated tube, 2.46m downstream from the magnet. A high-resolution image place (IP_{HR}), a phosphor (LANEX) screen and a plastic scintillator further reinforce the detection of GeV electrons. Between magnet and detectors, electrons and X-rays passed through two arrays of thin, precisely positioned tungsten-wire fiducials, which cast identifying shadows on the detectors. These shadows determined the electron energy at 2 GeV with 5% uncertainty at the

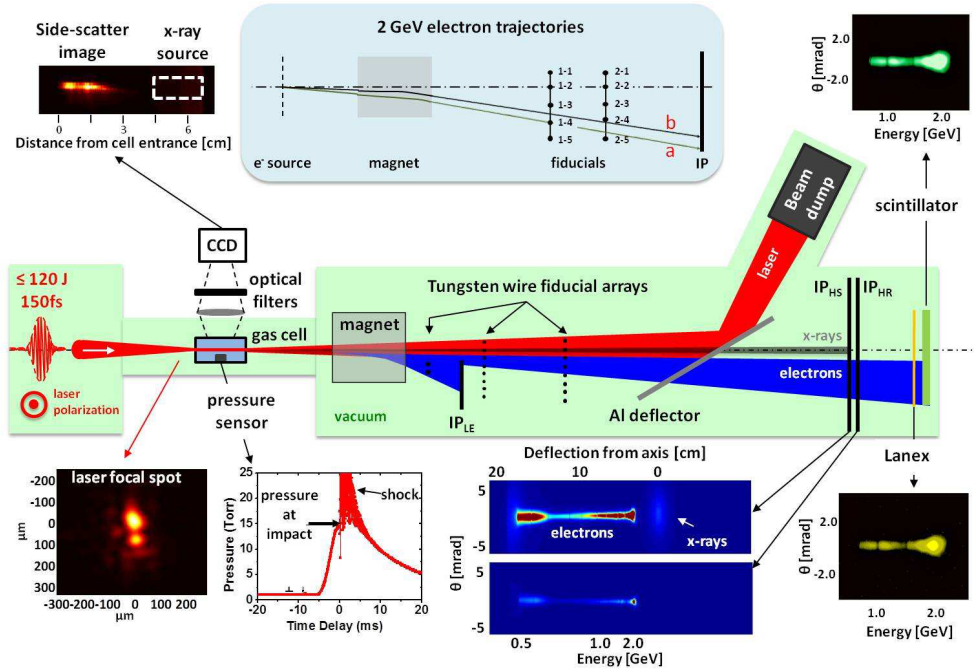


Figure 7.1: Schematic diagram of PW laser-driven wakefield accelerator. The green area were in a vacuum chamber at 10^{-6} Torr. The linearly polarized PW laser pulse enters the interaction region from left. Inside the gas cell, He plasma was generated and accelerated electrons to 2 GeV which were detected by the magnetic spectrometer with two arrays of $127 \mu\text{m}$ diameter tungsten-wire fiducials 1.256 and 1.764 m after the gas cell exit. Surrounding panels include: **(a)** transversely scattered light imaged to a CCD camera; **(b)** trajectories of 2 GeV electrons relative to the fiducial arrays; **(c-f)** unprocessed data showing electrons up to 2.3 GeV and fiducial shadows using scintillator **(c)**, LANEX **(d)**, IP_{HS} **(e)** and IP_{HR}; **g** He pressure versus time with an acoustic shock wave; **h** a typical laser focal spot.

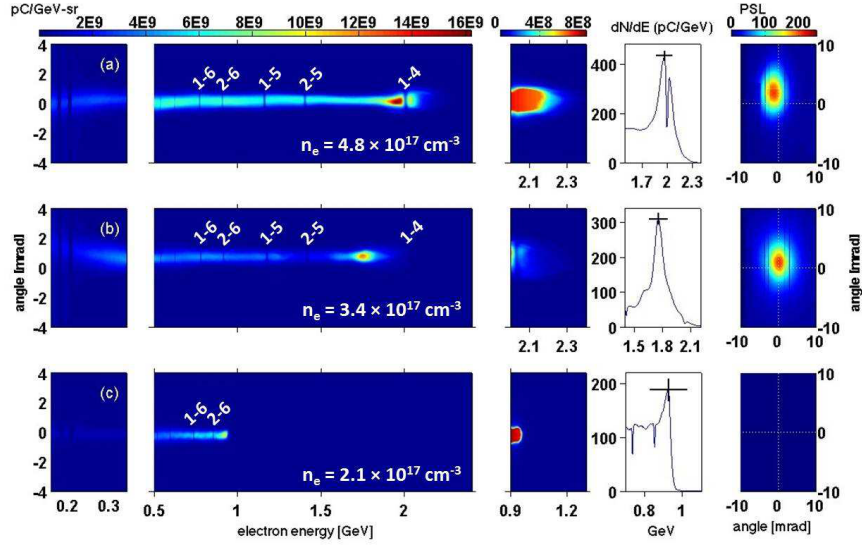


Figure 7.2: Electron spectra and betatron X-ray profiles for three shots (a–c) from the accelerator. Column 1: low energy electrons (< 350 MeV) recorded by another image plate (IP_{LE}). Column 2: GeV electron spectra recorded on IP_{HS} . Column 3: zoom-in of high-energy tails. Column 4: vertically integrated electron energy spectra around each high-energy peak. Column 5: betatron X-ray angular distribution recorded on IP_{HS} .

2σ level.

Figure 7.2 presents GeV electron spectra (column 1 to 4) and corresponding betatron X-ray angular distributions (column 5) in three separate shots (a–c). Table 7.1 shows numerical properties of and experimental conditions for each shot. Peak electron energy at 2 GeV is observed for shots a and b, and the high energy tail in shot a can reach 2.3 GeV. Mono-energetic behavior is convincing that the energy spread (FWHM) of the electron energy peak is below 7% for all these three shots. The electron beams also exhibit

Shot	E_e (GeV)	$\Delta E/E_e$	θ_e (mrad)	Q_{tot} (pC)	n_e (10^{17}cm^{-3})	E_{laser} (J)	τ (fs)
a	2.0 ± 0.1	6%	0.6 ± 0.1	540 ± 60	4.8 ± 0.1	100 ± 5	160 ± 10
b	1.8 ± 0.1	5%	0.5 ± 0.1	400 ± 50	3.4 ± 0.1	120 ± 5	150 ± 10
c	0.95 ± 0.1	7%	0.5 ± 0.1	100 ± 20	2.1 ± 0.1	129 ± 5	160 ± 10

Table 7.1: Properties of and experimental conditions for producing GeV electron beams

highly collimated behavior with a maximum diverging angle no larger than 0.6 mrad. The accelerated electrons are self-injected into the plasma wakefield without any external injection mechanisms, however, the injection process is so efficient that up to 500 pC total charge was observed, with $> 10\%$ of them aggregated around the mono-energetic peak. A large amount of electrons accelerated and trapped in a plasma bubble with transverse field is critical for betatron X-ray generation.

7.1.2 Betatron X-ray generation

Fig. 7.2 column 5 shows the angular distribution of betatron X-rays which were emitted from accelerated electrons wiggling within the evacuated plasma bubble. The electrons experience betatron oscillation at frequency $\omega_\beta = \omega_p/\sqrt{2}\gamma$ because of the transverse electric field within the bubble. Here γ is the increasing Lorentz factor of the accelerated electrons; for 2 GeV electrons, $\gamma = 4000$. Meanwhile, the measured diverging angle of the X-ray beam is around 2.5 mrad, corresponding to the strength parameter $K = \gamma\theta_\beta \approx 10$. Since K significantly exceeds 1, the transverse motion of electrons is in the large K wiggler regime rather than the small K undulator limit. In this

case, a broad spectrum of the X-ray beam with a critical photon energy $E_{\text{crit}} = 3\hbar K\gamma^2\omega_\beta$ should be observed. Coarse betatron X-ray spectra were obtained by measuring X-ray transmission through aluminum and copper masks with stepped thickness of 2 mm, 1 mm, 0.5 mm, and 0.25 mm. Only X-ray photons beyond a specific threshold energy can transmit through a given thickness of material. Thus stepped masks of Al/Cu can resolve the X-ray spectrum with low resolution. Typical X-ray spectra were peaked at 25 ± 10 keV and with a high energy tail extending beyond 70 keV [89]. The total X-ray photon number ranged from 10^8 to 10^9 , compared to previous 10^6 to 10^8 photons using a 200 MeV laser wakefield accelerator [42]. Moreover, compared to > 100 keV x-rays emitted by 700 MeV electrons [10] where the betatron amplitude was resonantly enhanced by the rear of the laser pulse, the X-ray observed here appeared not to be resonantly enhanced.

7.2 Multi-object-plane imaging of petawatt-laser-driven plasma wakes

In this section we present initial results of multi-object-plane imaging of the interaction of petawatt laser pulses with tenuous plasma under conditions that produced 2 GeV electrons. Because only limited time and equipment were available, only a low-resolution MOPI setup was used. Improved MOPI is an ongoing priority of our group's petawatt-laser-driven LWFA experiments.

7.2.1 Relativistic self-focusing and merging of laser hot-spots

Multi-GeV electron acceleration in tenuous plasma (10^{17} cm^{-3}) requires acceleration length as long as $\sim 10 \text{ cm}$. Thus obtaining and maintaining a focused laser transverse profile over such long distance is critical. The irregular transverse profile of focused Texas PW pulses, which sometimes contain multiple hot-spots, complicates this self-focusing and self-guiding process. Single-shot optical diagnosis of the plasma bubble structure created by such complicated pulses is a critical part of understanding current limitations to accelerator performance, and improving its performance in the future. The laser beam self-focuses relativistically in photo-ionized plasma, enabling laser intensity $I_0 > 2 \times 10^{19} \text{ W/cm}^2$ to be achieved. As a result, the vector potential of the laser pulse reaches $a = 0.85\sqrt{\lambda^2(\mu\text{m})I_0(10^{18} \text{ W/cm}^2)} > 4$, sufficient to generate plasma wakefield in the nonlinear bubble regime. For irregular incident laser pulse profiles, neighboring hot-spots can merge together to a single high-intensity laser spot for wakefield excitation [19].

A simulation of non-axisymmetric laser wave propagating relativistically in the plasma was conducted based on the nonlinear Schrödinger equation (NLSE)

$$2ik\frac{\partial a}{\partial z} + \nabla_{\perp}^2 a + 4k_p^2 \left(1 - \frac{1 + k_p^{-2}\nabla_{\perp}^2\gamma}{\gamma}\right) = 0 \quad (7.1)$$

where k and k_p are the laser and plasma wave number, respectively. Three assumptions underlie Eq. (7.1): (i) the laser pulse profile evolves slowly — *i.e.* $k\partial_z \gg \partial_z^2$; (ii) longitudinal profiles of the laser pulse and plasma wave are not taken into account; thus the laser ponderomotive force on each electron

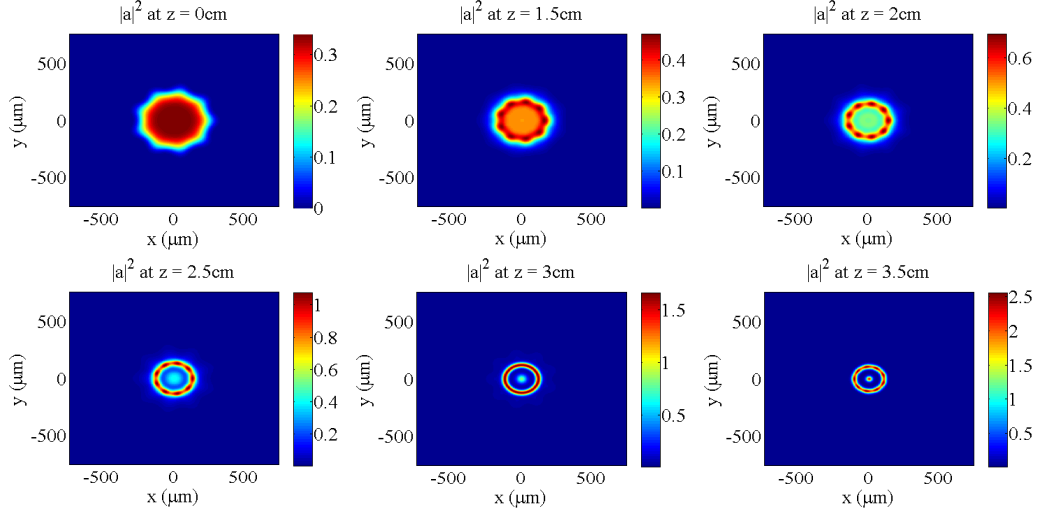


Figure 7.3: NLSE simulation illustrating topological changes of a relativistically self-focusing laser pulse. The color bars indicate the squared laser strength parameter a^2 . The laser pulse evolves according to the NLSE in a plasma of density $n_e = 5 \times 10^{17} \text{ cm}^{-3}$, through propagation distance at $z = 0$ (a), 1.5 cm (b), 2.0 cm (c), 2.5 cm (d), 3.0 cm (e), and 3.5 cm (f).

is balanced by the field induced by plasma charge separation; (iii) the laser is focused by the relativistic effect and free electron redistribution.

Fig. 7.3 showed propagation dynamics of a laser pulse with multiple hotspots, represented by initial azimuthally varying super-Gaussian envelopes of the form $a = a_0 \exp[-(r_{\perp}/w_0)^n] \times [1 + \alpha (r_{\perp}/w_0)^m \cos(m\phi)]$ where m and n are integers and α a fraction between 0 and 1. Here we have $m = 9$, $n = 6$, $\alpha = 0.25$, $a_0 = 0.58$ and $w_0 = 275 \mu\text{m}$, and the plasma density is $n_e = 5 \times 10^{17} \text{ cm}^{-3}$. At the beginning of the propagation process ($z < 2 \text{ cm}$), hot-spots self-focus separately, and then start to merge to a central spot and a ring outside at $z = 3 \text{ cm}$. After $z = 3.5 \text{ cm}$, laser energy is fed from the ring to the central

spot, and normalized peak intensity increases to $|a|^2 \approx 2.5$ for plasma wave excitation. This simplified calculation roughly illustrate the dynamics of laser propagation in plasma, *i.e.* self-focusing and hot-spot coalescence for the first $2 \sim 3$ cm of the propagation distance until intensity reaches values sufficient to excite a plasma bubble needed for electron capture and acceleration.

7.2.2 Preliminary multi-object-plane imaging results

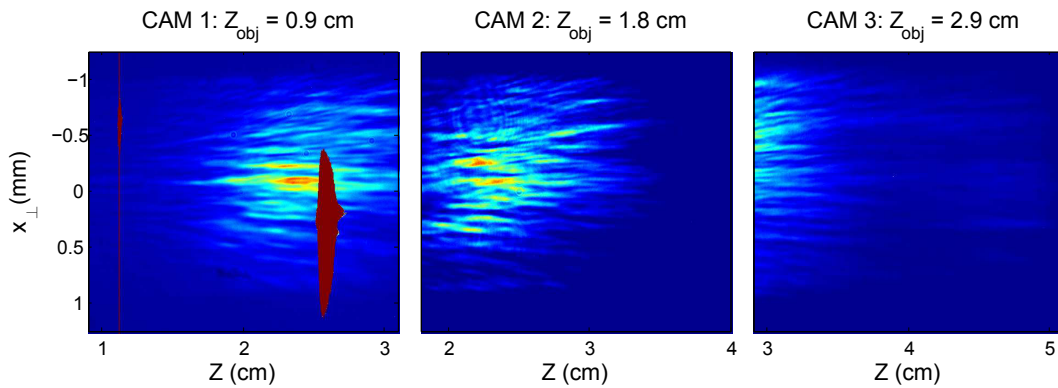


Figure 7.4: Multi-object-plane imaging probe intensity modulation. Three probes images the gas cell at $z = 0.9$ cm (a), 1.8 cm (b), 2.9 cm (c), respectively.

Multi-object-plane imaging discussed in Chapter 6 was applied to measure plasma wakefield-induced refractive index perturbation driven by the Texas PW laser. Three CCD cameras were used to image the interaction region at distances $z = 0.9$, 1.8, and 2.9 cm from the gas cell entrance. Fig. 7.4 shows probe intensity profile modulations of the probe resulting from its plasma-induced phase shift. The $\sim 100 \mu\text{m}$ wide plasma wakefield is surrounded by a plasma channel about one millimeter wide. Apart from their contrasting

widths, however, the phase shifts induced by wake or plasma channel are not inherently distinguishable. In fact, the total phase shift induced by the channel was so large that phase-contrast enhancement of imaging sensitivity proved unnecessary. Phase-to-amplitude conversion was accomplished by exploiting the existing finite aperture of the optical imaging system.

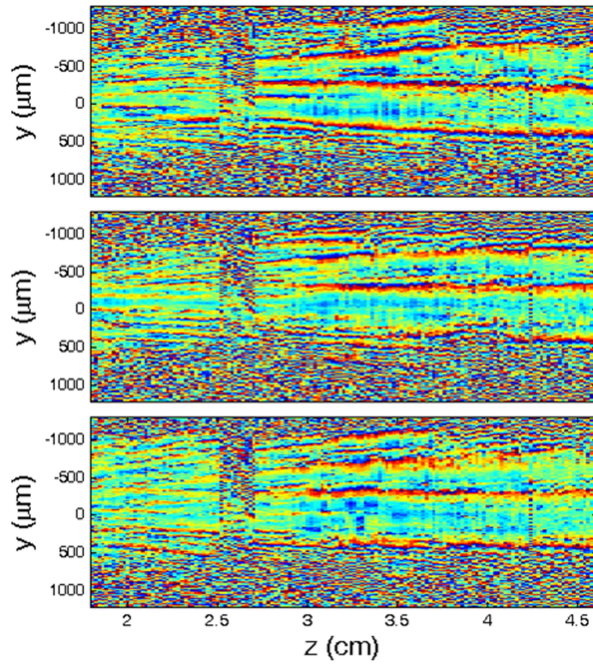


Figure 7.5: Reconstructed plasma wakefield induced probe phase shift in three different shots, showing spatial profile (x_{\perp}) of wakefields at different propagation distance (z).

Fig. 7.5 showed reconstructed probe phase shift from probe intensity modulations for three shots. In all three shots, phase shift induced by 1 mm plasma channel is present, with transverse range from $x_{\perp} \approx -800$ to $400 \mu\text{m}$

and over the whole propagation distance. However, for $z > 3$ cm, a ~ 100 μm wide phase shift structure forms in the center of the plasma channel, which is believed to be introduced by plasma bubble formation after the laser propagates to $z \sim 3$ cm. This is consistent with the NLSE simulation of the petawatt laser pulse propagating in plasma, which showed that the laser self-focuses near the beginning of the plasma, reaching intensity required for bubble formation after $z > 3$ cm. This is also supported by the optical side-scattering images shown in Fig. 7.1. The side-scattering signal only exists within $z < 3$ cm for all these three shots, and disappears after that region. For $z > 3$ cm, the laser pulse is guided inside the plasma bubble without free electrons inside, thus the scattering of the laser pulse is extremely low. However, for $z < 3$ cm, the laser pulse overlaps with free electrons and enables significant scattering. The correlation between multi-object-plane imaging and side scattering imaging results further confirm the bubble formation for electron acceleration.

In summary, petawatt-laser-driven wakefield accelerators represents a major new development in plasma acceleration. It features “long” pulse laser (~ 100 fs) propagating in tenuous plasma ($\sim 10^{17}$ cm^{-3}), and achieves multi-GeV electron acceleration and coherent keV X-ray generation. Compared to multi-terawatt-laser-driven wakefield accelerators, the petawatt-driven devices take advantage of elongated dephasing length and depletion length, at the expense of slightly reduced acceleration field because of the low plasma density. To quantitatively visualize the light-speed acceleration structures in petawatt laser wakefield acceleration, our multi-object-plane imaging (MOPI) technique

should replace frequency-domain interferometry, since it successfully meets the challenges that multi-centimeter interaction length raises to the imaging depth of field. Here we were only able to complete a preliminary MOPI observation of bubble formation. Future improved MOPI experiments should resolve the transverse profile evolution, and the spatiotemporal profile of the plasma bubbles in each single shot, once the experimental conditions are further improved. For example, the probe pulse can be fully compressed, controlled with reduced time-jitter, and tilted with the pulse front for longitudinal pump-probe compensation. In addition, advanced method for pump-probe synchronization method can also be adopted to define the accurate time T_0 within ~ 100 fs.

Chapter 8

Conclusion and Outlook

In summary, three single-shot optical techniques for visualizing the evolving structure of light-speed index objects have been developed: frequency-domain streak camera (FDSC), frequency-domain tomography (FDT), and multi-object-plane imaging (MOPI). For each of these techniques, prototype experiments or applications in laser wakefield acceleration were demonstrated. These techniques provide experimental physicists a visualization capability that heretofore has been available only through intensive particle-in-cell (PIC) simulations based on estimated initial conditions. These techniques bring the evolving structure of laser wakefields and other light-speed structures into direct, immediate experimental view for the first time, and provide a basis for optimizing and scaling them.

As shown in Table 8.1, these techniques visualize evolving (z -dependent) refractive index structures $n(\zeta, x, y, z)$ in a single shot. The FDSC provides a time sequence of the index structure's projections at a specific projection angle $\phi(\theta)$. By choosing the probe angle θ over a small range in the lab frame, the projection angle ϕ can vary from 0 to $\sim 90^\circ$, revealing the evolution history of the transverse or longitudinal profiles, respectively. In Chapter 4, we

showed that an FDSC revealing the evolving longitudinal profile of laser-driven plasma bubbles provided key physical insights into the causes of both optimal and sub-optimal electron acceleration. Frequency-domain tomography (FDT), a multi-probe generalization of FDSC, applies probes at different angles simultaneously to reconstruct a time sequence of the index structure’s spatiotemporal profile – *i.e.* a movie. Movie frames generated by FDT in a single shot were compared directly with frames generated by a computer simulation that required many hours, yet agreed with high fidelity on most essential details. To visualize evolution over long propagation distances, where probe diffraction limits the performance of FDSC or FDT, MOPI extended the depth of field by imaging from multiple object planes simultaneously and adopting a small probe oblique angle geometry. Nonlinear phase contrast imaging was applied to improve imaging sensitivity to tenuous, low-contrast index structures.

Techniques	Equation	Probe number	Interaction distance
FDSC	$\int n(\zeta, x, y_{\text{slit}}, z) dx$	single probe	short
FDT	$n(\zeta, x, y_{\text{slit}}, z)$	multi-probe	short
MOPI	$\int n(\zeta_0, x, y, z) dy$	single probe	long

Table 8.1: Comparison among single-shot visualization techniques: frequency-domain streak camera (FDSC), frequency-domain tomography (FDT), multi-object-plane imaging (MOPI)

It is interesting to discuss these different techniques in the language of degrees of freedom, in order to explore the possibility of accomplishing true single-shot 4-dimensional visualization of evolving index structures $n(\zeta_{\text{ob}}, x_{\text{ob}}, y_{\text{ob}}, z_{\text{ob}})$. In all these techniques, the profile of the probe field phase shifts is measured at

a detector: the transverse profile $\psi(x_{\text{pr}}, y_{\text{pr}})$ in MOPI, or the spatiotemporal profile $\psi(\zeta_{\text{pr}}, x_{\text{pr}})$ in FDSC or FDT. It is impossible to image the complete profile $\psi(\zeta_{\text{pr}}, x_{\text{pr}}, y_{\text{pr}})$ with a single detector in a single shot because any optical detector integrates the signal over its shutter time, which lasts up to nanoseconds. On the other hand, evolutional, or z_{ob} -dependent, information of the index structure is encoded within the probe profile's transverse or longitudinal dimension, through oblique angle geometry or pump-probe group delay respectively. Thus a general rule for all single-shot optical visualization techniques is that a single probe in a single shot can only provide the evolving light speed object's information with two degrees of freedom, one along its evolutional dimension z_{ob} and the other along a specific view of its spatiotemporal profiles, no matter what trick is used. For example, a single probe in FDSC or FDT provides a 2D phase streak. Line-outs across the streak axis provide the object's projection at the specific projection angle ϕ and those along the streak represent the evolution history. In the case of MOPI, the object's evolution dynamics are mapped onto one probe transverse dimension, and the object's transverse profiles is directly imprinted onto the other probe transverse dimension.

The challenge of visualizing 4-D evolution of the index structure amounts to recovering the two missing degrees of freedom. For all visualization techniques listed in Table 8.1, one degree of freedom is lost due to the relative motion between pump and probe (a form of integration, or blurring), whereas the other is lost due to a slicing procedure. For FDSC, the index structure's

projection provides an image along the projection view angle, but blurs the spatiotemporal profile ($\zeta_{\text{ob}}-x_{\text{ob}}$) along the perpendicular direction. The sliced dimension along y_{ob} originates from the spectrometer slit. FDT provides our prototypical example of successful recovery of a missing degrees of freedom, specifically the blurred dimension. By applying multiple probes in a single shot together with tomographic reconstruction, the integrated or blurred dimension is resolved. However, the “sliced” dimension along y_{ob} can be resolved only by using multiple spectrometers with the entrance slit of each aligned with a different y_{ob} . In the oblique angle MOPI case, a single probe resolved the evolution (z) history of the transverse profile along x , leaving the transverse dimension y integrated and the longitudinal dimension ζ sliced by the limited probe duration. The y -transverse dimension can be resolved by applying probes at different azimuthal angles and the longitudinal ζ -dependent information by varying the pump-probe time delay over multiple shots (as demonstrated in Chapter 5), or by using multiple probes at different delays in a single shot.

All optical visualization techniques can be categorized as pump-probe schemes for refractive index measurement, which in plasma is closely related to spatial distribution of free electrons. Future work might explore the birefringence of plasma in a relativistic intense laser field [86], much as measurements of birefringence in gaseous nonlinear Kerr medium helps distinguish electronic and molecule rotation components of the nonlinear refractive index [88]. Plasma refractive index in strong laser fields is not only a function

of plasma density, but also depends on the free electrons' relativistic quivering energy. Measurement of birefringence from the latter component provides electron quivering energy (or “temperature”) distribution, in the light-speed pump co-moving frame. Moreover, because of momentum conservation along the transverse direction, the laser vector potential \mathbf{a}_0 equals the transverse electron momentum \mathbf{p}_\perp that $\mathbf{a}_0 = \mathbf{p}_\perp$. Thus electron quivering “temperature” map can be directly related to the spatiotemporal profile of laser pulse at relativistic laser intensity (*i.e.* $> 10^{18}$ W/cm²). Visualization of relativistic-intensity laser pulse evolution is potentially able to reveal underlying physics in relativistic nonlinear optics and intense laser plasma interactions. Currently no techniques exist for directly measuring relativistic laser intensities, or the associated plasma birefringence that it induces.

Visualization of laser wakefield accelerators is not limited to optical methods, especially visible pump-probe schemes. The boundaries of plasma bubbles in modern laser plasma accelerators are sometimes formed of free electrons beyond the critical density, and thus reflecting long-wavelength probe photons and leaving the sharp sheath layer undetectable. Refractive index or plasma density measurements yield only indirect information about the acceleration field. To probe electromagnetic fields directly in laser plasma physics, particle probes instead of laser pulses can be another option. As an example, protons accelerated by an intense laser pulse were used to probe the target normal sheath acceleration (TNSA) mechanism in laser proton accelerators [71]. Similarly, electrons from laser wakefield accelerators can also be used to probe

laser plasma structures. Such electrons have unique advantages over protons: narrower energy spectrum, better beam collimation, much larger charge-mass ratio, sensitivity to weak fields or thin plasma features. Moreover, the time duration of the electron bunch is typically less than 10 fs, providing a superior source for time-resolved studies of intense laser plasma physics.

Appendices

Appendix A

Laser systems for experiments

Experiments in this dissertation involve single-shot optical visualization of refractive index structures triggered by lasers at different energy scales, ranging from microjoule to ~ 100 joules per pulse. For laser filamentation propagation in solids or gases, the Kerr-induced self-focusing requires laser peak power of the order of several times the critical power $P_{\text{cr}} = \lambda^2/4\pi n_0 n_2$, which is 2.4 GW for air and 1.6 MW for silica glass. Thus if 100 fs laser is propagating in the air (Chapter 6) or glass (Chapter 3 and 5), the pulse energy is of the order of millijoule or microjoule respectively. For laser-plasma acceleration experiments, the laser power should exceed the relativistic critical power of plasma $P_{\text{cr}} \approx 17(\omega/\omega_p)^2$ GW. Thus the laser pulse energy varies based on the plasma density. Laser-plasma accelerators at 10^{19} cm^{-3} density that produce ~ 100 MeV electron beams requires multi-terawatt laser power and ~ 1 J level of laser energy, whereas laser-plasma accelerators at 10^{17} cm^{-3} density for multi-GeV electrons needs petawatt laser with ~ 100 J energy per pulse. Here the laser systems for these experiments are reviewed.

The UT³ Ti:Sapphire laser is a commercial system (Alpha 10/XS) from Thales Lasers. The basic specifications of the system are shown in Table A.1.

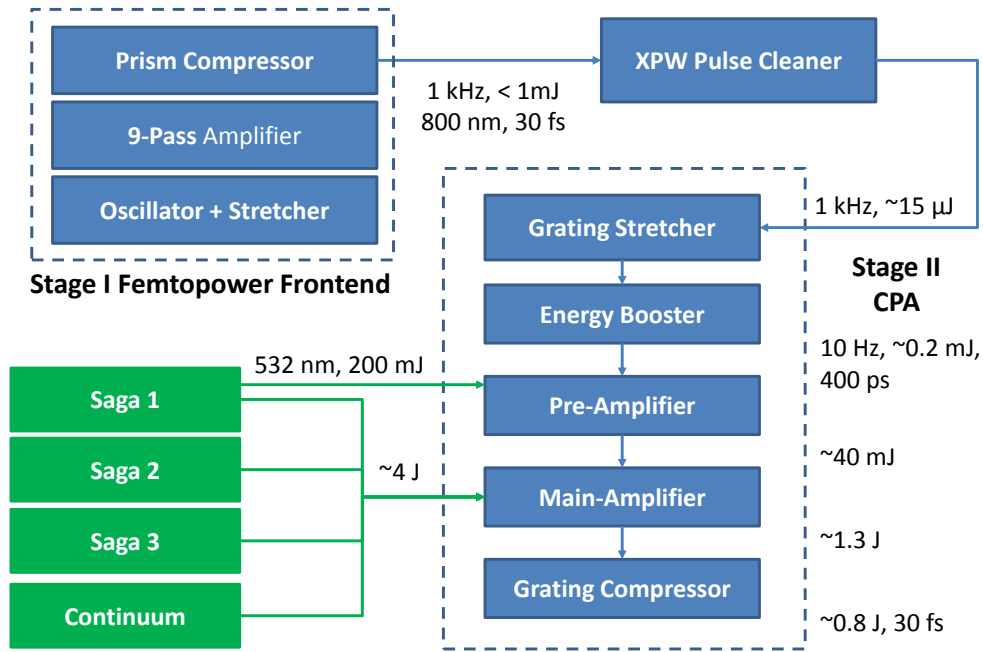


Figure A.1: Schematic diagram of the UT³ Alpha 10/XS 45 TW laser system.

The whole system consists of two stages of chirped pulse amplification (CPA) (Fig. A.1). The first stage is a compact laser system from Femtolasers with one kilohertz output of 30 fs laser pulses centered at 800 nm. The maximum output pulse energy is 1 mJ. However in practice it is attenuated to 0.2 mJ using a half-wave plate and polarizer in order to avoid optical damage in the cross-polarization wave (XPW) generator for pulse cleaning. The cleaned pulses are chirped to 400 ps in the grating stretcher and amplified to 0.2 mJ in the booster, then they are sent to amplifiers. The pre-amplifier is pumped by a small portion (~ 200 mJ) of the SAGA 1 laser. Seed light travels five passes through a Ti:Sapphire crystal to be amplified to 40 mJ. The main

Repetition rate	10 Hz
Peak power	≥ 45 TW
Energy per pulse	1.2 J
Pulse duration	≤ 30 fs
Wavelength	~ 800 nm

Table A.1: Output specifications of Alpha 10/XS 45 TW

amplifier has three passes and is pumped by four pump lasers, thus the seed beam is amplified to 1.3 J per pulse. After the grating compressor, the pulse is compressed back to 30 fs, and pulse energy is around 800 mJ.

Using this system, laser energy of widely different orders of magnitude is obtainable by coupling the beam out at different stages. For glass filamentation experiments, the kilohertz output of the front end is directly used to provide microjoule level laser pulses. To study laser filamentation in air, the output from the pre-amplifier is compressed by a separately built grating compressor, yielding ~ 20 mJ, 40 fs laser pulses. Laser plasma acceleration experiments were conducted with full laser power.

Appendix B

The Frequency-Domain Tomography reconstruction algorithm and codes

The frequency-domain tomography (FDT) reconstruction code is named **FDT3D**, and runs on a personal computer with Windows 7 operating system and Microsoft Visual Studio 2010 software. The code is written in C++, and defines three classes — **Voxel**, **Phantom**, and **FDSC** — which describe the index structure at specific $(\zeta_{\text{ob}}, x_{\text{ob}}, z_{\text{ob}})$, the whole index structure $\Delta n(\zeta_{\text{ob}}, x_{\text{ob}}, z_{\text{ob}})$, and phase streak $\psi(\zeta_{\text{pr}}, x_{\text{pr}})$, respectively. The algorithm is based on Algebraic Reconstruction Technique (ART) [34].

First of all, the general head file **fdt3d.h** is defined, and there is a declaration of standard libraries. Two global constants are defined, **PI** representing $\pi = 3.141592654 \dots$ and **Wpr** representing probe laser wavelength which is 0.4 micrometer. Classes (*i.e.* **Voxel**, **Phantom**, and **FDSC**) and functions (**GenFDSC**, **LoadFDSC**, **SimpleART**, **TrickART**) are claimed.

```
1 #pragma once
3 #include "Phantom.h"
4 #include "FDSC.h"
5 #include "Voxel.h"
7 #include <iostream>
8 #include <sstream>
9 #include <cmath>
```

```

#include <fstream>
11 #include <string>
#include <vector>
13 #include <cstdlib>
#include <ctime>
15
#define PI 3.14159265358979323846264338327950288419716939937510
17 #define Wpr 0.4
// #define MAXRAND
19
void GenFDSC(Phantom &obj, std::vector<FDSC> &proj, std::vector<
    double> &alist, std::vector<double> &dplist, std::vector<double>
    &dqlist, double Np, double Nq);
21 void LoadFDSC(Phantom &solution, std::vector<FDSC> &proj, std::
    string fname);
void SimpleART(Phantom &obj, std::vector<FDSC> &proj);
23 void TrickART(Phantom &obj, Phantom &stand, std::vector<FDSC> &
    proj, std::vector<double> bt, double zedge);

```

The class **Voxel** defines a specific spatiotemporal point of the index evolution history $\Delta n(\zeta, x, z)$. The position and index value of the point is stored in each object of class **Voxel**.

```

1 #pragma once
3 class Voxel
{
5 public:
    Voxel(void) {}
    Voxel(int x, int y, int z, double v) {}
    ~Voxel(void) {}
    double GetVal(void) {return val;}
    int GetXi(void) {return xi;}
    int GetYi(void) {return yi;}
    int GetZi(void) {return zi;}
    void SetXi(int x) {xi=x;}
    void SetYi(int y) {yi=y;}
    void SetZi(int z) {zi=z;}
    void SetVal(double v) {val=v;}
17 private:
    int xi, yi, zi;

```

```

19 |     double val;
    | };

```

The object of the class **Phantom** represents the whole 3D index structure evolution history $\Delta n(\zeta, x, z)$. It gets access to each voxel, *i.e.* reading and writing. Here two construction functions are defined. The one with 6 input parameters set all voxel index values to zero, and is typically applied to store the reconstructed solution in both phantom simulation or actual data processing. The other one with 7 parameters is used for the phantom simulation only, *i.e.* the phantom object is constructed using this construction function and stored in one object of the class **Phantom**.

```

#pragma once
2 |
#include <vector>
4 | #include <cmath>
#include <iostream>
6 | #include "Voxel.h"
8 |
class Phantom
9 | {
10 | public:
    Phantom(void);
12 |     Phantom(int nx, int ny, int nz, double xsize, double ysize,
        double zsize);
    Phantom::Phantom(int nx, int ny, int nz, double xsize, double
        ysize, double zsize, double val);
14 |     //Phantom(Phantom &ori);
    ~Phantom(void);
16 |     double GetVoxel(int xi, int yi, int zi);
    double GetVoxel(Voxel vox);
18 |     void SetVoxel(int xi, int yi, int zi, double val);
    void SetVoxel(Voxel Voxel);
20 |     int GetXSize(void){return Nx;}
    int GetYSize(void){return Ny;}
22 |     int GetZSize(void){return Nz;}

```

```

24     double GetXdSize(void){return dx;}
25     double GetYdSize(void){return dy;}
26     double GetZdSize(void){return dz;}
27 private:
28     int Nx, Ny, Nz;
29     double dx, dy, dz;
30     std::vector<Voxel> vox;
31 };
32 //=====
33
34 #include "Phantom.h"
35
36 Phantom::Phantom(void):Nx(0),Ny(0),dx(0.0),dy(0.0)
37 {
38 }
39
40 Phantom::Phantom(int nx, int ny, int nz, double xsize, double
41 ysize, double zsize):Nx(nx),Ny(ny),Nz(nz),dx(xsize),dy(ysize),
42 dz(zsize)
43 {
44     int i, j, k;
45     double val(0);
46     double Xr(dx*Nx), Yr(dy*Ny), Zr(dz*Nz);
47     for (k=-Nz; k<Nz; ++k)
48     {
49         double z = dz*k;
50         for (j=-Ny; j<Ny; ++j)
51         {
52             for (i=-Nx; i<Nx; ++i)
53             {
54                 double x = dx*i;
55                 double y = dy*j;
56                 // original phantom object before March 18, 2013
57                 // double val = exp(-exp(-(y/Yr/yscal+0.2)/0.05)-
58                 // pow((y/Yr/yscal+0.1)/0.3,2))*exp(-exp(-(x/Xr/
59                 // xscal+0.3)/0.05)-pow((x/Xr/xscal+0.1)/0.4,2));
60
61                 // Further test of selected phantom pattern, March
62                 // 21, 2013
63                 double xdim, ydim, jump;
64                 if (z/Zr>0)
65                 {
66                     xdim = z/Zr+1;
67                     ydim = 1;

```

```

64         }
        else
66         {
            xdim = 1;
            ydim = -z/Zr+1;
68         }
        jump = exp(-pow(30*z/Zr,2))+0.2/(1+exp(-100*z/Zr))
        ;
70         val = exp(-pow(5*(y/Yr+0.2)/ydim,18))*exp(-pow(5*(
            x/Xr+0.2)/xdim,18))-exp(-pow(5*1.2*(y/Yr+0.2)/
            ydim,18))*exp(-pow(5*1.2*(x/Xr+0.2)/xdim,18));
        val = val+jump*exp(-pow(7*(y/Yr-0.45),2))*exp(-pow
            (7*(x/Xr-0.45),2));
72
        vox.push_back(Voxel(i,j,k,val));
74     }
    }
76 }
78
Phantom::Phantom(int nx, int ny, int nz, double xsize, double
    ysize, double zsize, double val):Nx(nx),Ny(ny),Nz(nz),dx(xsize
    ),dy(ysize),dz(zsize)
80 {
    for (int k=-Nz; k<Nz; ++k)
82         for (int j=-Ny; j<Ny; ++j)
            for (int i=-Nx; i<Nx; ++i)
84                 vox.push_back(Voxel(i,j,k,val));
    }
86
Phantom::~~Phantom(void)
88 {
    }
90
double Phantom::GetVoxel(int xi, int yi, int zi)
92 {
    if (yi>=Ny || yi<=-Ny || xi>=Nx || xi<=-Nx || zi<=-Nz || zi>=Nz)
94         return 0;
    else
96         return vox[(zi+Nz)*4*Nx*Ny+(yi+Ny)*2*Nx+(xi+Nx)].GetVal();
    }
98
double Phantom::GetVoxel(Voxel vox)
100 {
    int xi = vox.GetXi();

```

```

102     int yi = vox.GetYi();
103     int zi = vox.GetZi();
104     return GetVoxel(xi, yi, zi);
105 }
106 void Phantom::SetVoxel(int xi, int yi, int zi, double val)
107 {
108     if (yi>=Ny || yi<=-Ny || xi>=Nx || xi<=-Nx || zi<=-Nz || zi>=Nz);
109     else
110     {
111         vox[(zi+Nz)*4*Nx*Ny+(yi+Ny)*2*Nx+(xi+Nx)].SetXi(xi);
112         vox[(zi+Nz)*4*Nx*Ny+(yi+Ny)*2*Nx+(xi+Nx)].SetYi(yi);
113         vox[(zi+Nz)*4*Nx*Ny+(yi+Ny)*2*Nx+(xi+Nx)].SetZi(zi);
114         vox[(zi+Nz)*4*Nx*Ny+(yi+Ny)*2*Nx+(xi+Nx)].SetVal(val);
115     }
116 }
117
118 void Phantom::SetVoxel(Voxel voxel)
119 {
120     int xi = voxel.GetXi();
121     int yi = voxel.GetYi();
122     int zi = voxel.GetZi();
123     double val = voxel.GetVal();
124     SetVoxel(xi, yi, zi, val);
125 }
126 }

```

The class **FDSC** basically describes the phase shift at a specific point (ζ_{pr}, x_{pr}) in the probe phase streak. The position, phase shift, and the probe angle are stored, and accessible through member functions. The pump and probe laser group velocities are normalized to light speed and stored as **bob_val** and **bpr_val** respectively. The variable **list** is generated dynamically and includes all voxels through which the projection trajectory crosses.

```

#pragma once
2
#include <cmath>
4 #include <vector>
#include <fstream>

```

```

6 #include <iostream>
7 #include "Phantom.h"
8
9 class FDSC
10 {
11 public:
12     FDSC(void);
13     FDSC(double ang, double p, double q, Phantom &obj); //
14
15     Construction function for Phantom simulation
16     FDSC(double ang, double p, double q, double val, Phantom &
17         solution);
18     // Construction function for actual data processing
19     ~FDSC(void);
20     double GetVal(){return val;}
21     double GetP(){return p;}
22     double GetQ(){return q;}
23     double GetAng(){return ang;}
24     std::vector<Voxel> GetList(){return list;}
25     static double bpr_val(void){return bpr;}
26     static double bob_val(void){return bob;}
27 private:
28     double ang; // Angle between pump and probe
29     double p,q; // Each pixel number in a FDSC
30     int Nx,Ny,Nz; // voxel number along three
31         dimensions of the original movie
32     double dx,dy,dz; // size of each voxel
33     double val; // phase shift value of FDSC
34     std::vector<Voxel> list; // voxel list along the FDSC
35         integral line
36     static double bpr; // probe group velocity
37     static double bob; // pump group velocity, or object
38         velocity
39 };
40
41 //=====
42 #include "FDSC.h"
43 #include "fdt3d.h"
44
45 double FDSC::bob = 0.6806;
46 double FDSC::bpr = 0.6616;
47
48 FDSC::FDSC(void)
49 {
50 }

```

```

44
46 FDSC::FDSC(double ang, double p, double q, Phantom &obj):ang(ang),p(p
    ),q(q)
    // constructive function for simulation data, assumptions:
48 // 1. At time 0, the centers of probe frame and object frame
    overlap
    {
50     Nx = obj.GetXSize();
51     Ny = obj.GetYSize();
52     Nz = obj.GetZSize();
53     dx = obj.GetXdSize();
54     dy = obj.GetYdSize();
55     dz = obj.GetZdSize();
56     val = 0;
57     double cv(cos(ang)),sv(sin(ang)),tv(tan(ang));
58     double x1,x2,y1,y2,z1,z2;
59     int flap_x, flap_y;
60     double r = bpr/bob;
61     // Determine the crossing points between the projection
        trajectory and the whole evolution box, time scale O(1),
        space scale O(1)
62     // The definition of x1,y1,x2,y2 are different from later,
        here just mean z positions.
63     if (r*cv<1)
64     {
65         x1 = (p*cv+q*sv-Nx*dx)/(1-r*cv);
66         x2 = (p*cv+q*sv+Nx*dx)/(1-r*cv);
67         flap_x = -1;
68     }
69     else if (r*cv>1)
70     {
71         x1 = (p*cv+q*sv+Nx*dx)/(1-r*cv);
72         x2 = (p*cv+q*sv-Nx*dx)/(1-r*cv);
73         flap_x = 1;
74     }
75     else
76     {
77         x1 = -Nz*dz;
78         x2 = Nz*dz;
79         flap_x = 0;
80     }
81     if (sv>0)
82     {
        y1 = (-p*sv+q*cv-Ny*dy)/r/sv;

```



```

84         y2 = (-p*sv+q*cv+Ny*dy)/r/sv;
           flap_y = -1;
86     }
     else if (sv<0)
88     {
           y1 = (-p*sv+q*cv+Ny*dy)/r/sv;
           y2 = (-p*sv+q*cv-Ny*dy)/r/sv;
           flap_y = 1;
92     }
     else
94     {
           y1 = -Nz*dz;
           y2 = Nz*dz;
           flap_y = 0;
98     }
    z1 = std::max(-Nz*dz, std::max(x1, y1));
    z2 = std::min(Nz*dz, std::min(x2, y2));
    x1 = p*cv+q*sv-(1-r*cv)*z1;
    x2 = p*cv+q*sv-(1-r*cv)*z2;
    y1 = -p*sv+q*cv-r*sv*z1;
    y2 = -p*sv+q*cv-r*sv*z2;
104

106    // Determine the cross points on each wall, time scale O(N),
           space scale O(N)
    std::vector<int> xwall;
    std::vector<int> ywall;
    std::vector<int> zwall;
108    for (int zi = floor(z1/dz)+1; zi<=floor(z2/dz); ++zi)
           zwall.push_back(zi);
112    if (flap_x==1)
           for (int xi = floor(x1/dx)+1; xi<=floor(x2/dx); ++xi)
                   xwall.push_back(xi);
114    else if (flap_x==-1)
           for (int xi = floor(x1/dx); xi>floor(x2/dx); --xi)
                   xwall.push_back(xi);
116    else;
118    if (flap_y==1)
           for (int yi = floor(y1/dy)+1; yi<=floor(y2/dy); ++yi)
                   ywall.push_back(yi);
120    else if (flap_y==-1)
           for (int yi = floor(y1/dy); yi>floor(y2/dy); --yi)
                   ywall.push_back(yi);
122    else;
124

126    // Combine all cross points on three walls, generating the

```

```

    projection list , time scale O(N) , space scale O(N)
128  double t=0;
    int xin(0),yin(0),zin(0);
130  double tx = xwall.empty() ? 1.1:(xwall[0]*dx-x1)/(x2-x1);
    double ty = ywall.empty() ? 1.1:(ywall[0]*dy-y1)/(y2-y1);
132  double tz = zwall.empty() ? 1.1:(zwall[0]*dz-z1)/(z2-z1);
    int xp = floor(x1/dx);
134  int yp = floor(y1/dy);
    int zp = floor(z1/dz);
136  while (xin<xwall.size() || yin<ywall.size() || zin<zwall.size
        ())
    {
138      double tmp = t;
        t = tx;
140      int index = 1;
        if (ty<t)
142      {
            index = 2;
144            t = ty;
        }
        if (tz<t)
146      {
            index = 3;
148            t = tz;
        }
        // double sect = (t-tmp)*sqrt((x2-x1)*(x2-x1)+(y2-y1)*(y2-
150        y1)+(z2-z1)*(z2-z1));
        double sect = (t-tmp)*(z2-z1);
152        list.push_back(Voxel(xp,yp,zp,sect));
        val += 2*PI/Wpr*FDSC::bpr_val()/FDSC::bob_val()*sect*obj.
154        GetVoxel(xp,yp,zp);
        switch (index)
156        {
            case 1:
158                xp = flap_x==1?xwall[xin]:xwall[xin]-1;
                    ++xin;
160                tx = (xin==xwall.size())?1.1:(xwall[xin]*dx-x1)/(x2-x1
                    );
                    break;
162            case 2:
                    yp = flap_y==1?ywall[yin]:ywall[yin]-1;
164                    ++yin;
                    ty = (yin==ywall.size())?1.1:(ywall[yin]*dy-y1)/(y2-y1
                    );
                    break;
166            case 3:
                    zp = flap_z==1?zwall[zin]:zwall[zin]-1;
                    ++zin;
                    tz = (zin==zwall.size())?1.1:(zwall[zin]*dz-z1)/(z2-z1
                    );
                    break;
        }
    }

```

```

168         case 3:
            zp = zwall[zin];
            ++zin;
170         tz = (zin==zwall.size())?1.1:(zwall[zin]*dz-z1)/(z2-z1
            );
            break;
172         default:
            std::runtime_error("Error in generating index of pump
            wall...\n");
174     }
    }
176 // double sect = (1-t)*sqrt((x2-x1)*(x2-x1)+(y2-y1)*(y2-y1)+(
    z2-z1)*(z2-z1));
    double sect = (1-t)*(z2-z1);
178 list.push_back(Voxel(xp,yp,zp,sect));
    val += 2*PI/Wpr*FDSC::bpr_val()/FDSC::bob_val()*sect*obj.
    GetVoxel(xp,yp,zp);
180 }

182 FDSC::FDSC(double ang, double p, double q, double val, Phantom &
    solution):ang(ang),p(p),q(q),val(val)
    // constructive function for simulation data, assumptions:
184 // 1. At time 0, the centers of probe frame and object frame
    overlap
    {
186     Nx = solution.GetXSize();
        Ny = solution.GetYSize();
188     Nz = solution.GetZSize();
        dx = solution.GetXdSize();
190     dy = solution.GetYdSize();
        dz = solution.GetZdSize();
192     double cv(cos(ang)),sv(sin(ang)),tv(tan(ang));
        double x1,x2,y1,y2,z1,z2;
194     int flap_x, flap_y;
        double r = bpr/bob;
196     // Determine the crossing points between the projection
        trajectory and the whole evolution box, time scale O(1),
        space scale O(1)
        // The definition of x1,y1,x2,y2 are different from later,
        here just mean z positions.
198     if (r*cv<1)
        {
200         x1 = (p*cv+q*sv-Nx*dx)/(1-r*cv);
            x2 = (p*cv+q*sv+Nx*dx)/(1-r*cv);
202         flap_x = -1;

```

```

204     }
    else if (r*cv>1)
    {
206         x1 = (p*cv+q*sv+Nx*dx)/(1-r*cv);
           x2 = (p*cv+q*sv-Nx*dx)/(1-r*cv);
208         flap_x = 1;
    }
    else
    {
212         x1 = -Nz*dz;
           x2 = Nz*dz;
214         flap_x = 0;
    }
    if (sv>0)
    {
218         y1 = (-p*sv+q*cv-Ny*dy)/r/sv;
           y2 = (-p*sv+q*cv+Ny*dy)/r/sv;
220         flap_y = -1;
    }
    else if (sv<0)
    {
224         y1 = (-p*sv+q*cv+Ny*dy)/r/sv;
           y2 = (-p*sv+q*cv-Ny*dy)/r/sv;
226         flap_y = 1;
    }
    else
    {
230         y1 = -Nz*dz;
           y2 = Nz*dz;
232         flap_y = 0;
    }
    z1 = std::max(-Nz*dz, std::max(x1, y1));
    z2 = std::min(Nz*dz, std::min(x2, y2));
236    x1 = p*cv+q*sv-(1-r*cv)*z1;
           x2 = p*cv+q*sv-(1-r*cv)*z2;
238    y1 = -p*sv+q*cv-r*sv*z1;
           y2 = -p*sv+q*cv-r*sv*z2;
240
    // Determine the cross points on each wall, time scale O(N),
    // space scale O(N)
242    std::vector<int> xwall;
           std::vector<int> ywall;
244    std::vector<int> zwall;
    for (int zi = floor(z1/dz)+1; zi<=floor(z2/dz); ++zi)
246        zwall.push_back(zi);

```

```

248     if (flap_x==1)
        for (int xi = floor(x1/dx)+1; xi<=floor(x2/dx); ++xi)
            xwall.push_back(xi);
250     else if (flap_x==-1)
        for (int xi = floor(x1/dx); xi>floor(x2/dx); --xi)
252         xwall.push_back(xi);
        else;
254     if (flap_y==1)
        for (int yi = floor(y1/dy)+1; yi<=floor(y2/dy); ++yi)
256         ywall.push_back(yi);
        else if (flap_y==-1)
258         for (int yi = floor(y1/dy); yi>floor(y2/dy); --yi)
            ywall.push_back(yi);
260     else;

262     // Combine all cross points on three walls, generating the
        projection list, time scale O(N), space scale O(N)
        double t=0;
264     int xin(0),yin(0),zin(0);
        double tx = xwall.empty() ? 1.1:(xwall[0]*dx-x1)/(x2-x1);
266     double ty = ywall.empty() ? 1.1:(ywall[0]*dy-y1)/(y2-y1);
        double tz = zwall.empty() ? 1.1:(zwall[0]*dz-z1)/(z2-z1);
268     int xp = floor(x1/dx);
        int yp = floor(y1/dy);
270     int zp = floor(z1/dz);
        while (xin<xwall.size() || yin<ywall.size() || zin<zwall.size
            ())
272     {
        double tmp = t;
274         t = tx;
        int index = 1;
276         if (ty<t)
            {
278             index = 2;
                t = ty;
280             }
        if (tz<t)
282         {
            index = 3;
284             t = tz;
            }
286         // double sect = (t-tmp)*sqrt((x2-x1)*(x2-x1)+(y2-y1)*(y2-
            y1)+(z2-z1)*(z2-z1));
        double sect = (t-tmp)*(z2-z1);
288         list.push_back(Voxel(xp,yp,zp,sect));

```

```

290     switch (index)
291     {
292     case 1:
293         xp = flap_x==1?xwall[xin]:xwall[xin]-1;
294         ++xin;
295         tx = (xin==xwall.size())?1.1:(xwall[xin]*dx-x1)/(x2-x1
296         );
297         break;
298     case 2:
299         yp = flap_y==1?ywall[yin]:ywall[yin]-1;
300         ++yin;
301         ty = (yin==ywall.size())?1.1:(ywall[yin]*dy-y1)/(y2-y1
302         );
303         break;
304     case 3:
305         zp = zwall[zin];
306         ++zin;
307         tz = (zin==zwall.size())?1.1:(zwall[zin]*dz-z1)/(z2-z1
308         );
309         break;
310     default:
311         std::runtime_error("Error in generating index of pump
312         wall...\n");
313     }
314 }
315 //double sect = (1-t)*sqrt((x2-x1)*(x2-x1)+(y2-y1)*(y2-y1)+(z2
316 -z1)*(z2-z1));
317 double sect = (1-t)*(z2-z1);
318 list.push_back(Voxel(xp,yp,zp,sect));
319 }
320 FDSC::~~FDSC(void)
321 {
322 }

```

The FDSC data is generated in the file **GenFDSC.cpp**, including two functions **GenFDSC** and **LoadFDSC**. The former is used to calculate phase streaks based on artificially assumed index structures in the phantom simulation, whereas the latter directly loads phase shift data from experiments.

Phase streak data is stored in an array of **FDSC** objects.

```

1 #include "fdt3d.h"
3 template<typename T> int sgn(T val)
4 {
5     if (val>0)
6         return 1;
7     else if (val<0)
8         return -1;
9     else
10        return 0;
11 }
13 void GenFDSC(Phantom &obj, std::vector<FDSC> &proj, std::vector<
double> &alist, std::vector<double> &dplist, std::vector<double>
&dqlist, double Np, double Nq)
14 {
15     double r = FDSC::bpr_val()/FDSC::bob_val();
16     double Xr = obj.GetXdSize()*obj.GetXSize();
17     double Yr = obj.GetYdSize()*obj.GetYSize();
18     double Zr = obj.GetZdSize()*obj.GetZSize();
19     for (int ia=0; ia<alist.size(); ++ia)
20     {
21         double dp = dplist[ia];
22         double dq = dqlist[ia];
23         double ang = alist[ia];
24         double cv = cos(ang);
25         double sv = sin(ang);
26         std::cout<<"Generating FDSC at angle "<<ang*180/PI<<"
degree...\n";
27         for (int qi=-Nq; qi<Nq; ++qi)
28         {
29             for (int pi=-Np; pi<Np; ++pi)
30             {
31                 double p = dp*pi;
32                 double q = dq*qi;
33                 double x1 = p*cv+q*sv+(1-r*cv)*Zr;
34                 double y1 = -p*sv+q*cv+r*sv*Zr;
35                 double x2 = p*cv+q*sv-(1-r*cv)*Zr;
36                 double y2 = -p*sv+q*cv-r*sv*Zr;
37                 double corner1 = sgn((x2-x1)*(-Yr-y1)-(y2-y1)*(-Xr
-x1));
38                 double corner2 = sgn((x2-x1)*(-Yr-y1)-(y2-y1)*(Xr-
x1));

```

```

39         double corner3 = sgn((x2-x1)*(Yr-y1)-(y2-y1)*(-Xr-
        x1));
        double corner4 = sgn((x2-x1)*(Yr-y1)-(y2-y1)*(Xr-
        x1));
41         if (abs(corner1+corner2+corner3+corner4)==4)
            continue;
43         else if (((x1>Xr) && (x2>Xr)) || ((x1<-Xr) && (x2
        <-Xr)) || ((y1>Yr) && (y2>Yr)) || ((y1<-Yr) &&
        (y2<-Yr)))
            continue;
45         else
            proj.push_back(FDSC(ang, pi*dp, qi*dq, obj));
47     }
49 }
51 }
51 void LoadFDSC(Phantom &solution, std::vector<FDSC> &proj, std::
string fname)
53 {
55     std::ifstream ifile(fname);
55     std::string line;
57     double ang, p, q, val;
57     double r = FDSC::bpr_val()/FDSC::bob_val();
59     double Xr = solution.GetXdSize()*solution.GetXSize();
59     double Yr = solution.GetYdSize()*solution.GetYSize();
61     double Zr = solution.GetZdSize()*solution.GetZSize();
61     while (std::getline(ifile, line))
63     {
63         std::istringstream istr(line);
63         istr >> ang;
65         double cv = cos(ang);
65         double sv = sin(ang);
67         istr >> p;
69         // p = p*0.3*FDSC::bpr_val();
69         istr >> q;
69         istr >> val;
71         double x1 = p*cv+q*sv+(1-r*cv)*Zr;
71         double y1 = -p*sv+q*cv+r*sv*Zr;
73         double x2 = p*cv+q*sv-(1-r*cv)*Zr;
73         double y2 = -p*sv+q*cv-r*sv*Zr;
75         double corner1 = sgn((x2-x1)*(-Yr-y1)-(y2-y1)*(-Xr-x1));
75         double corner2 = sgn((x2-x1)*(-Yr-y1)-(y2-y1)*(Xr-x1));
77         double corner3 = sgn((x2-x1)*(Yr-y1)-(y2-y1)*(-Xr-x1));
77         double corner4 = sgn((x2-x1)*(Yr-y1)-(y2-y1)*(Xr-x1));

```



```

79         if (abs(corner1+corner2+corner3+corner4)==4)
           continue;
81     else if (((x1>Xr) && (x2>Xr)) || ((x1<-Xr) && (x2<-Xr)) ||
              ((y1>Yr) && (y2>Yr)) || ((y1<-Yr) && (y2<-Yr)))
           continue;
83     else
           proj.push_back(FDSC(ang,p,q,val,solution));
85     }
}

```

The ART reconstruction is based on the algorithm introduced in the reference [34]. Here two functions are defined in the same file **ART.cpp**, they are **SimpleART** and **TrickART**. The former one describes the basic ART algorithm and iteration procedure, however typically it cannot guarantee a good reconstruction quality. Thus the **TrickART** function is developed to incorporate the selective smoothing procedure and some prior constraints on the solution.

```

1 #include "fdt3d.h"
3 // Definition of reconstruction parameters
  const double relax_para = 0.1;           // relax parameter for
      all ART routines
5 const int Max_Iter = 20;                 // maximum number of
      iterations
  const double meas_para = 2;             // For Add1ART,
      control the weight of measured data compared to 1 for prior
      data
7 const double tol_para = 0.05;           // For Add2ART,
      tolerance of the measured projection
9 //=====
  /*
11 Function description
13     void SimpleART(Phantom &obj, std::vector<FDSC> &proj);

```

```

15 1. Input:
    obj    — reference of reconstructed object, initially
17         set as a three dimension zero matrix
    proj   — reference of measured or generated projection
           data in the form of vector

19 2. Output:  reconstructed object.

21 3. Controlable parameters:
    relax_para  — relaxation parameter, ranging from -1
                to 1, positive small number is preferred
23    Max_Iter   — maximum iteration number required,
                around 10 is enough.

25 4. Algorithm:
     $x(k+1) = x(k) + rp(k) * (y(i) - \langle r(i), x(k) \rangle) / \langle r(i), r(i) \rangle^2 * r(i)$ 
    )

27
29 5. Reference:
    H. Garbor's book Chap 11

31 */
32 //=====
33 void SimpleART(Phantom &obj, std::vector<FDSC> &proj)
34 {
35     std::cout<<"SimpleART is running...\n";
36     int iter(0);
37     while (iter<Max_Iter)
38     {
39         std::cout<<"Simple ART running at "<<iter+1<<" iteration
40             ... \n";
41         for (int iFDSC=0; iFDSC<proj.size(); ++iFDSC)
42         {
43             double z1(0), z2(0);
44             std::vector<Voxel> cross = proj[iFDSC].GetList();
45             for (int ivox=0; ivox<cross.size(); ++ivox)
46             {
47                 z1 += obj.GetVoxel(cross[ivox].GetXi(), cross[ivox]
48                     .GetYi(), cross[ivox].GetZi()) * cross[ivox].
49                     GetVal();
50                 z2 += pow(cross[ivox].GetVal(), 2);
51             }
52             z1 *= 2*PI/Wpr*iFDSC::bpr_val()/iFDSC::bob_val();
53             z2 *= 2*PI/Wpr*iFDSC::bpr_val()/iFDSC::bob_val();
54             double coef = relax_para*(proj[iFDSC].GetVal()-z1)/z2;
55             for (int ivox=0; ivox<cross.size(); ++ivox)

```

```

53         {
           double val = cross [ivox].GetVal()*coef+obj.
               GetVoxel(cross [ivox].GetXi(),cross [ivox].GetYi
                   (),cross [ivox].GetZi());
           obj.SetVoxel(cross [ivox].GetXi(),cross [ivox].GetYi
               (),cross [ivox].GetZi(),val);
55         }
56     }
57     ++iter;
58 }
59 }
60 // End SimpleART
61
62 //=====
63 /*
64 Function description
65
66 void TrickART(Phantom &obj, std::vector<FDSC> &proj, std::vector<
67     double> bt)
68
69     1. Input:
70         obj      — reference of reconstructed object, initially
71                   set as a three dimension zero matrix
72         proj     — reference of measured or generated projection
73                   data in the form of vector
74         bt       — smooth parameter for 3D smoothing
75
76     2. Output:  reconstructed object.
77
78     3. Controlable parameters:
79         relax_para — relaxation parameter, ranging from -1
80                   to 1, positive small number is prefered
81         Max_Iter   — maximum iteration number required,
82                   around 10 is enough.
83         bt1        — weight of central pixel in the
84                   smoothing procedure
85         bt2        — weight of the edge neighbours in the
86                   smoothing procedure
87         bt3        — weight of the point neighbours in the
88                   smoothing procedure
89
90     4. Algorithm:
91         Iteration step:
92         
$$x(k+1) = x(k) + rp(k) * (y(i) - \langle r(i), x(k) \rangle) / \langle r(i), r(i) \rangle$$


```

```

85     Smoothing step:
        x(i,j) = bt1*x(i,j) + 0.25*bt2*[x(i,j+1)+x(i,j-1)+x(i
            -1,j)+x(i+1,j)] + 0.25*bt3*[x(i+1,j+1)+x(i+1,j-1)+
            x(i-1,j+1)+x(i-1,j-1)]
87 */
88 //=====
89 void TrickART(Phantom &obj, Phantom &stand, std::vector<FDSC> &
    proj, std::vector<double> bt, double zedge)
    {
91     std::cout<<"TrickART is running...\n";
        int iter(0);
93     std::vector<double> residue(Max_Iter);
        std::ofstream res_file("residue.txt");
95     while (iter<Max_Iter)
        {
97         std::cout<<"TrickART running at "<<iter+1<<" iteration...\n";
            for (int iFDSC=0; iFDSC<proj.size(); ++iFDSC)
            {
99                 double z1(0), z2(0);
                    std::vector<Voxel> cross = proj[iFDSC].GetList();
                    for (int ivox=0; ivox<cross.size(); ++ivox)
                    {
103                        z1 += obj.GetVoxel(cross[ivox].GetXi(), cross[ivox].
                            GetYi(), cross[ivox].GetZi())*cross[ivox].
                            GetVal();
105                        z2 += pow(cross[ivox].GetVal(), 2);
                    }
                    z1 *= 2*PI/Wpr*FDSC::bpr_val()/FDSC::bob_val();
                    z2 *= 2*PI/Wpr*FDSC::bpr_val()/FDSC::bob_val();
109                    double coef = relax_para*(proj[iFDSC].GetVal()-z1)/z2;
                    for (int ivox=0; ivox<cross.size(); ++ivox)
                    {
111                        int xi = cross[ivox].GetXi();
                            int yi = cross[ivox].GetYi();
                            int zi = cross[ivox].GetZi();
115                        double val = cross[ivox].GetVal()*coef+obj.
                            GetVoxel(xi, yi, zi);
                            // Applying selective smoothing to the object
117                        val = bt[0]*val+bt[1]/6*(obj.GetVoxel(xi-1,yi,zi)+
                            obj.GetVoxel(xi+1,yi,zi)+obj.GetVoxel(xi,yi-1,
                            zi)+obj.GetVoxel(xi,yi+1,zi)+obj.GetVoxel(xi,
                            yi,zi-1)+obj.GetVoxel(xi,yi,zi+1))
                            +bt[2]/12*(obj.GetVoxel(xi-1,yi-1,zi)+obj.
                            GetVoxel(xi-1,yi+1,zi)+obj.GetVoxel(xi+1,

```

```

119         yi-1,zi)+obj.GetVoxel(xi+1,yi+1,zi)+obj.
        GetVoxel(xi-1,yi,zi-1)+obj.GetVoxel(xi-1,
        yi,zi+1)
120     +obj.GetVoxel(xi+1,yi,zi-1)+obj.GetVoxel(xi
        +1,yi,zi+1)+obj.GetVoxel(xi,yi-1,zi-1)+
        obj.GetVoxel(xi,yi-1,zi+1)+obj.GetVoxel(
        xi,yi+1,zi-1)+obj.GetVoxel(xi,yi+1,zi+1))
121     +bt[3]/8*(obj.GetVoxel(xi-1,yi-1,zi-1)+obj.
        GetVoxel(xi+1,yi-1,zi-1)+obj.GetVoxel(xi
        -1,yi+1,zi-1)+obj.GetVoxel(xi+1,yi+1,zi
        -1)+obj.GetVoxel(xi-1,yi-1,zi+1)
122     +obj.GetVoxel(xi+1,yi-1,zi+1)+obj.GetVoxel(xi
        -1,yi+1,zi+1)+obj.GetVoxel(xi+1,yi+1,zi+1)
        );
        // Applying positive value to the object
123     // if (val<0)
        // val = 0;
124     // Applying the glass edge prior information
125     if (abs(zi*obj.GetZdSize()+xi*obj.GetXdSize())>
        zedge)
126         val = 0;
127     obj.SetVoxel(xi,yi,zi,val);
128 }
129 }
130 }
131 residue[iter] = 0;
132 for (int ix=-obj.GetXSize(); ix<obj.GetXSize(); ++ix)
133     for (int iy=-obj.GetYSize(); iy<obj.GetYSize(); ++iy)
134         for (int iz=-obj.GetZSize(); iz<obj.GetZSize(); ++
        iz)
135             residue[iter] += pow((obj.GetVoxel(ix,iy,iz)-
        stand.GetVoxel(ix,iy,iz)),2);
        residue[iter] = sqrt(residue[iter]/8/obj.GetXSize()/obj.
        GetYSize()/obj.GetZSize());
136     res_file <<iter <<'\t'<<residue[iter]<<std::endl;
        ++iter;
137 }
138 }
139 res_file.close();
140 }
141 // End TrickART

```

As an example, here is the **main** function loading phase streak data

from a “.txt” file “simuFDSC_FF.txt”, reconstructing the index structure evolution history, and writing the results into file “recon_simuFDSC_FF.txt”.

```

1 #include "fdt3d.h"
3 int main(void)
4 {
5     srand(time(NULL));
6     const double zedge(1500.0);
7     const int Nx(32),Ny(32),Nz(128);
8     const double dx(30.0/Nx),dy(50.0/Ny),dz(1550.0/Nz);
9     std::cout<<"Generating phantom data...\n";
10    // Phantom obj(Nx,Ny,Nz,dx,dy,dz);
11    Phantom solution(Nx,Ny,Nz,dx,dy,dz,0.0);
12    // Output of the original object
13    std::cout<<"Generating FDSC at multiple probing angles...\n";
14    std::vector<FDSC> proj;
15
16    LoadFDSC(solution,proj,"simuFDSC_FF.txt");
17    // GenFDSC(obj,proj,alist,dplist,dqlist,128,128);
18
19    // ART reconstruction
20
21    std::vector<double> bt(4);
22    bt[0] = 0.96;
23    bt[1] = 0.02;
24    bt[2] = 0.01;
25    bt[3] = 1-bt[0]-bt[1]-bt[2];
26    TrickART(solution,solution,proj,bt,zedge);
27    std::cout<<"Exporting reconstructed object to recon.txt"<<std
28    ::endl;
29    std::ofstream ofile1("recon_simuFDSC_FF.txt");
30    for (int iz=1; iz<=2*Nz; ++iz)
31        for (int iy=1; iy<=2*Ny; ++iy)
32            for (int ix=1; ix<=2*Nx; ++ix)
33                ofile1<<ix<<"\t"<<iy<<"\t"<<iz<<"\t"<<solution.
34                GetVoxel(ix-1-Nx,iy-1-Ny,iz-1-Nz)<<std::endl;
35    ofile1.close();
36
37    return 0;
38 }

```

Appendix C

Publications by the author while at University of Texas

1. Zhengyan Li, R. Zgadza, X. Wang, Y. Y. Chang, and M. C. Downer, “Single-shot tomographic movies of evolving light-velocity objects,” *Nature Communications* **5**, 3085 (2014).
2. Zhengyan Li, C.-H. Pai, Y. Y. Chang and M. C. Downer, “Single-shot imaging of evolving light-velocity objects by multi-object-plane phase-contrast imaging,” *Optics Letters* **38**, 5157–5160 (2013).
3. X. Wang, R. Zgadza, N. Fazel, Z. Li, S. A. Yi, X. Zhang, W. Henderson, Y.-Y. Chang, R. Korzekwa, H.-E. Tsai, C.-H. Pai, H. Quevedo, G. Dyer, E. Gaul, M. Martinez, A. C. Bernstein, T. Borger, M. Spinks, M. Donovan, V. Khudik, G. Shvets, T. Ditmire and M. C. Downer, “Quasi-monoenergetic laser-plasma acceleration of electrons to 2 GeV,” *Nature Communications* **4**, 1988 (2013).
4. Z. Li, R. Zgadza, X. Wang, S. Reed and M. C. Downer, “Frequency-domain streak camera for ultrafast imaging of evolving light-velocity objects,” *Optics Letters* **35**, 4087–4089 (2010).

5. P. Dong, S. A. Reed, S. A. Yi, S. Y. Kalmykov, Z. Li, G. Shvets, M. C. Downer, N. H. Matlis, W. P. Leemans, C. McGuffey, S. S. Bulanov, V. Chvykov, G. Kalintchenko, K. Krushelnick, A. Maksimchuk, T. Matsuoka, A. G. R. Thomas and V. Yanovsky, “Holographic visualization of laser wakefields,” *New J. Phys.* **12**, 045016 (2010).
6. Zhengyan Li, Hai-En Tsai, Xi Zhang, Chih-Hao Pai, R. Zgadzaaj, X. Wang, V. Khudik, G. Shvets, M. C. Downer, “Single-shot visualization of evolving laser wakefields using an all-optical streak camera,” submitted to *Phys. Rev. Lett.*

Bibliography

- [1] Daryoush Abdollahpour, Dimitrios G. Papazoglou, and Stelios Tzortzakis. Four-dimensional visualization of single and multiple laser filaments using in-line holographic microscopy. *Phys. Rev. A*, 84:053809, Nov 2011.
- [2] D. Aumiler, T. Ban, and G. Pichler. Femtosecond laser-induced cone emission in dense cesium vapor. *Phys. Rev. A*, 71:063803, Jun 2005.
- [3] P. B ejot, E. Hertz, J. Kasparian, B. Lavorel, J. P. Wolf, and O. Faucher. Transition from plasma-driven to kerr-driven laser filamentation. *Phys. Rev. Lett.*, 106:243902, Jun 2011.
- [4] P. B ejot, J. Kasparian, S. Henin, V. Loriot, T. Vieillard, E. Hertz, O. Faucher, B. Lavorel, and J.-P. Wolf. Higher-order kerr terms allow ionization-free filamentation in gases. *Phys. Rev. Lett.*, 104:103903, Mar 2010.
- [5] S. P. Le Blanc, E. W. Gaul, N. H. Matlis, A. Rundquist, and M. C. Downer. Single-shot measurement of temporal phase shifts by frequency-domain holography. *Opt. Lett.*, 25(10):764–766, May 2000.
- [6] I. Blumenfeld, C. E. Clayton, F. J. Decker, M. J. Hogan, C. Huang, R. Ischebeck, R. Iverson, C. Joshi, T. Katsouleas, N. Kirby, W. Lu, K. A. Marsh, W. B. Mori, P. Muggli, E. Oz, R. H. Siemann, D. Walz, and

- M. Zhou. Energy doubling of 42 GeV electrons in a metre-scale plasma wakefield accelerator. *Nature*, 445(7129):741–744, February 2007.
- [7] R. W. Boyd. *Nonlinear Optics*. Academic Press, 2008.
- [8] A. Braun, G. Korn, X. Liu, D. Du, J. Squier, and G. Mourou. Self-channeling of high-peak-power femtosecond laser pulses in air. *Opt. Lett.*, 20(1):73–75, Jan 1995.
- [9] Alexander Buck, Maria Nicolai, Karl Schmid, Chris M. S. Sears, Alexander Savert, Julia M. Mikhailova, Ferenc Krausz, Malte C. Kaluza, and Laszlo Veisz. Real-time observation of laser-driven electron acceleration. *Nat Phys*, 7(7):543–548, July 2011.
- [10] Silvia Cipiccia, Mohammad R. Islam, Bernhard Ersfeld, Richard P. Shanks, Enrico Brunetti, Gregory Vieux, Xue Yang, Riju C. Issac, Samuel M. Wiggins, Gregor H. Welsh, Maria-Pia Anania, Dzmitry Maneuski, Rachel Montgomery, Gary Smith, Matthias Hoek, David J. Hamilton, Nuno R. C. Lemos, Dan Symes, Pattathil P. Rajeev, Val O. Shea, Joao M. Dias, and Dino A. Jaroszynski. Gamma-rays from harmonically resonant betatron oscillations in a plasma wake. *Nature Physics*, advance online publication, September 2011.
- [11] C. E. Clayton, C. Joshi, C. Darrow, and D. Umstadter. Relativistic plasma-wave excitation by collinear optical mixing. *Phys. Rev. Lett.*, 54:2343–2346, May 1985.

- [12] S. Corde, K. Ta Phuoc, G. Lambert, R. Fitour, V. Malka, A. Rousse, A. Beck, and E. Lefebvre. Femtosecond x rays from laser-plasma accelerators. *Rev. Mod. Phys.*, 85:1–48, Jan 2013.
- [13] A. Couairon and A. Mysyrowicz. Femtosecond filamentation in transparent media. *Physics Reports*, 441(2-4):47 – 189, 2007.
- [14] A. Couairon, L. Sudrie, M. Franco, B. Prade, and A. Mysyrowicz. Filamentation and damage in fused silica induced by tightly focused femtosecond laser pulses. *Phys. Rev. B*, 71:125435, Mar 2005.
- [15] C. A. Coverdale, C. B. Darrow, C. D. Decker, W. B. Mori, K-C. Tzeng, K. A. Marsh, C. E. Clayton, and C. Joshi. Propagation of intense subpicosecond laser pulses through underdense plasmas. *Phys. Rev. Lett.*, 74:4659–4662, Jun 1995.
- [16] AJ Devaney. Inverse-scattering theory within the rytov approximation. *Optics letters*, 6(8):374–376, 1981.
- [17] JM Dias, L Oliveira e Silva, and JT Mendonça. Photon acceleration versus frequency-domain interferometry for laser wakefield diagnostics. *Physical Review Special Topics-Accelerators and Beams*, 1(3):031301, 1998.
- [18] Peng Dong, S. A. Reed, S. A. Yi, S. Kalmykov, G. Shvets, M. C. Downer, N. H. Matlis, W. P. Leemans, C. McGuffey, S. S. Bulanov, V. Chvykov, G. Kalintchenko, K. Krushelnick, A. Maksimchuk, T. Matsuoka, A. G. R.

- Thomas, and V. Yanovsky. Formation of optical bullets in laser-driven plasma bubble accelerators. *Phys. Rev. Lett.*, 104:134801, Mar 2010.
- [19] Quan-Li Dong, Zheng-Ming Sheng, and Jie Zhang. Self-focusing and merging of two copropagating laser beams in underdense plasma. *Phys. Rev. E*, 66:027402, Aug 2002.
- [20] Katrin Ekvall, Cecilia Lundevall, and Peter van der Meulen. Studies of the fifth-order nonlinear susceptibility of ultraviolet-grade fused silica. *Opt. Lett.*, 26(12):896–898, Jun 2001.
- [21] E. Esarey, C. B. Schroeder, and W. P. Leemans. Physics of laser-driven plasma-based electron accelerators. *Rev. Mod. Phys.*, 81:1229–1285, Aug 2009.
- [22] J. Faure, Y. Glinec, A. Pukhov, S. Kiselev, S. Gordienko, E. Lefebvre, J. P. Rousseau, F. Burgy, and V. Malka. A laserplasma accelerator producing monoenergetic electron beams. *Nature*, 431(7008):541–544, September 2004.
- [23] Gadi Fibich, Yonatan Sivan, Yosi Ehrlich, Einat Louzon, Moshe Fraenkel, Shmuel Eisenmann, Yiftach Katzir, and Arie Zigler. Control of the collapse distance in atmospheric propagation. *Opt. Express*, 14(12):4946–4957, Jun 2006.
- [24] J. R. Fienup. Phase retrieval algorithms: a comparison. *Appl. Opt.*, 21(15):2758–2769, Aug 1982.

- [25] Matthias Fuchs, Raphael Weingartner, Antonia Popp, Zsuzsanna Major, Stefan Becker, Jens Osterhoff, Isabella Cortrie, Benno Zeitler, Rainer Horlein, George D. Tsakiris, Ulrich Schramm, Tom P. Rowlands-Rees, Simon M. Hooker, Dietrich Habs, Ferenc Krausz, Stefan Karsch, and Florian Grüner. Laser-driven soft-X-ray undulator source. *Nature Physics*, 5(11):826–829, September 2009.
- [26] Alexander L. Gaeta. Catastrophic collapse of ultrashort pulses. *Phys. Rev. Lett.*, 84:3582–3585, Apr 2000.
- [27] Erhard W. Gaul, Mikael Martinez, Joel Blakeney, Axel Jochmann, Martin Ringuette, Doug Hammond, Ted Borger, Ramiro Escamilla, Skylar Douglas, Watson Henderson, Gilliss Dyer, Alvin Erlandson, Rick Cross, John Caird, Christopher Ebbers, and Todd Ditmire. Demonstration of a 1.1 petawatt laser based on a hybrid optical parametric chirped pulse amplification/mixed nd:glass amplifier. *Appl. Opt.*, 49(9):1676–1681, Mar 2010.
- [28] C. G. R. Geddes, Cs Toth, J. van Tilborg, E. Esarey, C. B. Schroeder, D. Bruhwiler, C. Nieter, J. Cary, and W. P. Leemans. High-quality electron beams from a laser wakefield accelerator using plasma-channel guiding. *Nature*, 431(7008):538–541, September 2004.
- [29] J.-P. Geindre, P. Audebert, S. Rebibo, and J.-C. Gauthier. Single-shot spectral interferometry with chirped pulses. *Opt. Lett.*, 26(20):1612–1614, Oct 2001.

- [30] J. P. Geindre, A. Mysyrowicz, A. Dos Santos, P. Audebert, A. Rousse, G. Hamoniaux, A. Antonetti, F. Fallières, and J. C. Gauthier. Frequency-domain interferometer for measuring the phase and amplitude of a femtosecond pulse probing a laser-produced plasma. *Opt. Lett.*, 19(23):1997–1999, Dec 1994.
- [31] Dennis C. Ghiglia and Louis A. Romero. Robust two-dimensional weighted and unweighted phase unwrapping that uses fast transforms and iterative methods. *J. Opt. Soc. Am. A*, 11(1):107–117, Jan 1994.
- [32] Gennady G. Gladush and Igor Smurov. *Physics of laser materials processing: theory and experiment*. Springer, 2011.
- [33] Richard Gordon, Robert Bender, and Gabor T. Herman. Algebraic reconstruction techniques (art) for three-dimensional electron microscopy and x-ray photography. *Journal of Theoretical Biology*, 29(3):471 – 481, 1970.
- [34] G.T. Herman. *Fundamentals of Computerized Tomography: Image Reconstruction from Projections*. Advances in pattern recognition. Springer, 2009.
- [35] L. Hesselink, S. S. Orlov, and M. C. Bashaw. Holographic data storage systems. *Proceedings of the IEEE*, 92(8):1231–1280, 2004.
- [36] M. J. Hogan, T. O. Raubenheimer, A. Seryi, P. Muggli, T. Katsouleas, C. Huang, W. Lu, W. An, K. A. Marsh, W. B. Mori, et al. Plasma

- wakefield acceleration experiments at facet. *New Journal of Physics*, 12(5):055030, 2010.
- [37] A. C. Kak and M. Slaney. *Principles of Computerized Tomographic Imaging*. IEEE Press, New York, 1988.
- [38] S. Kalmykov, S. A. Yi, V. Khudik, and G. Shvets. Electron self-injection and trapping into an evolving plasma bubble. *Phys. Rev. Lett.*, 103:135004, Sep 2009.
- [39] L. V. Keldysh. Ionization in the field of a strong electromagnetic wave. *Soviet Physics JETP*, 20:1307–1314, May 1965.
- [40] K. Y. Kim, I. Alexeev, and H. M. Milchberg. Single-shot supercontinuum spectral interferometry. *Applied Physics Letters*, 81(22):4124+, 2002.
- [41] Y. Kitagawa, T. Matsumoto, T. Minamihata, K. Sawai, K. Matsuo, K. Mima, K. Nishihara, H. Azechi, K. A. Tanaka, H. Takabe, and S. Nakai. Beat-wave excitation of plasma wave and observation of accelerated electrons. *Phys. Rev. Lett.*, 68:48–51, Jan 1992.
- [42] S. Kneip, C. McGuffey, J. L. Martins, S. F. Martins, C. Bellei, V. Chvykov, F. Dollar, R. Fonseca, C. Huntington, G. Kalintchenko, A. Maksimchuk, S. P. D. Mangles, T. Matsuoka, S. R. Nagel, C. A. J. Palmer, J. Schreiber, K. Ta Phuoc, A. G. R. Thomas, V. Yanovsky, L. O. Silva, K. Krushelnick, and Z. Najmudin. Bright spatially coherent synchrotron X-rays from a table-top source. *Nature Physics*, 6(12):980–983, October 2010.

- [43] M. Kolesik, E. M. Wright, and J. V. Moloney. Dynamic nonlinear x waves for femtosecond pulse propagation in water. *Phys. Rev. Lett.*, 92:253901, Jun 2004.
- [44] Olga Kosareva, Jean-Francois Daigle, Nikolay Panov, Tiejun Wang, Sima Hosseini, Shuai Yuan, Gilles Roy, Vladimir Makarov, and See Leang Chin. Arrest of self-focusing collapse in femtosecond air filaments: higher order kerr or plasma defocusing? *Opt. Lett.*, 36(7):1035–1037, Apr 2011.
- [45] S. P. Le Blanc, M. C. Downer, R. Wagner, S.-Y. Chen, A. Maksimchuk, G. Mourou, and D. Umstadter. Temporal characterization of a self-modulated laser wakefield. *Phys. Rev. Lett.*, 77:5381–5384, Dec 1996.
- [46] W. P. Leemans, P. Catravas, E. Esarey, C. G. R. Geddes, C. Toth, R. Trines, C. B. Schroeder, B. A. Shadwick, J. van Tilborg, and J. Faure. Electron-yield enhancement in a laser-wakefield accelerator driven by asymmetric laser pulses. *Phys. Rev. Lett.*, 89:174802, Oct 2002.
- [47] W. P. Leemans and E. Esarey. Laser-driven plasma-wave electron accelerators. *Phys. Today*, 62, 2009.
- [48] W. P. Leemans, B. Nagler, A. J. Gonsalves, Cs Toth, K. Nakamura, C. G. R. Geddes, E. Esarey, C. B. Schroeder, and S. M. Hooker. GeV electron beams from a centimetre-scale accelerator. *Nature Physics*, 2(10):696–699, September 2006.

- [49] Z. Li, R. Zgadzaj, X. Wang, S. Reed, P. Dong, and M. C. Downer. Frequency-domain streak camera for ultrafast imaging of evolving light-velocity objects. *Opt. Lett.*, 35(24):4087–4089, Dec 2010.
- [50] Zhengyan Li, Chih-Hao Pai, Yen-Yu Chang, Rafal Zgadzaj, Xiaoming Wang, and M. C. Downer. Single-shot visualization of evolving, light-speed structures by multiobject-plane phase-contrast imaging. *Opt. Lett.*, 38(23):5157–5160, Dec 2013.
- [51] Zhengyan Li, Rafal Zgadzaj, Xiaoming Wang, Yen-Yu Chang, and Michael C. Downer. Single-shot tomographic movies of evolving light-velocity objects. *Nature Communications*, 5, 2014.
- [52] Vincent Lorient, Edouard Hertz, Olivier Faucher, and Bruno Lavorel. Measurement of high order kerr refractive index of major air components. *Opt. Express*, 17(16):13429–13434, Aug 2009.
- [53] W. Lu, M. Tzoufras, C. Joshi, F. S. Tsung, W. B. Mori, J. Vieira, R. A. Fonseca, and L. O. Silva. Generating multi-gev electron bunches using single stage laser wakefield acceleration in a 3d nonlinear regime. *Phys. Rev. ST Accel. Beams*, 10:061301, Jun 2007.
- [54] T. H. Maiman. Stimulated optical radiation in ruby. *Nature*, 187(4736):493–494, August 1960.
- [55] V. Malka, S. Fritzler, E. Lefebvre, M. M. Aleonard, F. Burgy, J. P. Chambaret, J. F. Chemin, K. Krushelnick, G. Malka, S. P. D. Mangles, Z. Naj-

- mudin, M. Pittman, J. P. Rousseau, J. N. Scheurer, B. Walton, and A. E. Dangor. Electron Acceleration by a Wake Field Forced by an Intense Ultrashort Laser Pulse. *Science*, 298(5598):1596–1600, November 2002.
- [56] S. P. D. Mangles, C. D. Murphy, Z. Najmudin, A. G. R. Thomas, J. L. Collier, A. E. Dangor, E. J. Divall, P. S. Foster, J. G. Gallacher, C. J. Hooker, D. A. Jaroszynski, A. J. Langley, W. B. Mori, P. A. Norreys, F. S. Tsung, R. Viskup, B. R. Walton, and K. Krushelnick. Monoenergetic beams of relativistic electrons from intense laserplasma interactions. *Nature*, 431(7008):535–538, September 2004.
- [57] N. H. Matlis, S. Reed, S. S. Bulanov, V. Chvykov, G. Kalintchenko, T. Matsuoka, P. Rousseau, V. Yanovsky, A. Maksimchuk, S. Kalmykov, G. Shvets, and M. C. Downer. Snapshots of laser wakefields. *Nature Physics*, 2(11):749–753, October 2006.
- [58] Nicholas Matlis. *Frequency domain holography of laser wakefields*. Ph.D. dissertation, 2006.
- [59] Barry P. Medoff, William R. Brody, Menahem Nassi, and Albert Macovski. Iterative convolution backprojection algorithms for image reconstruction from limited data. *J. Opt. Soc. Am.*, 73(11):1493–1500, Nov 1983.
- [60] W. B. Mori, C. D. Decker, D. E. Hinkel, and T. Katsouleas. Raman forward scattering of short-pulse high-intensity lasers. *Phys. Rev. Lett.*, 72:1482–1485, Mar 1994.

- [61] Gerard A. Mourou, Toshiki Tajima, and Sergei V. Bulanov. Optics in the relativistic regime. *Rev. Mod. Phys.*, 78:309–371, Apr 2006.
- [62] Kazuhisa Nakajima. Compact X-ray sources: Towards a table-top free-electron laser. *Nat Phys*, 4(2):92–93, February 2008.
- [63] A. M. Perelomov, V. S. Popov, and M. V. Terent’ev. Ionization of atoms in an alternating electric field. *Soviet Physics JETP*, 23:924–934, 1966.
- [64] Pavel Polynkin, Miroslav Kolesik, Ewan M. Wright, and Jerome V. Moloney. Experimental tests of the new paradigm for laser filamentation in gases. *Phys. Rev. Lett.*, 106:153902, Apr 2011.
- [65] A. Pukhov. Three-dimensional electromagnetic relativistic particle-in-cell code vlpl (virtual laser plasma lab). *Journal of Plasma Physics*, 61:425–433, 4 1999.
- [66] A. Pukhov and J. Meyer-ter Vehn. Laser wake field acceleration: the highly non-linear broken-wave regime. *Applied Physics B*, 74(4-5):355–361, 2002.
- [67] J. E. Ralph, K. A. Marsh, A. E. Pak, W. Lu, C. E. Clayton, F. Fang, W. B. Mori, and C. Joshi. Self-guiding of ultrashort, relativistically intense laser pulses through underdense plasmas in the blowout regime. *Phys. Rev. Lett.*, 102:175003, Apr 2009.

- [68] Jinendra K. Ranka, Robert W. Schirmer, and Alexander L. Gaeta. Observation of pulse splitting in nonlinear dispersive media. *Phys. Rev. Lett.*, 77:3783–3786, Oct 1996.
- [69] G. Rodriguez and A. J. Taylor. Measurement of cross-phase modulation in optical materials through the direct measurement of the optical phase change. *Opt. Lett.*, 23:858–860, 1998.
- [70] George Rodriguez, Anthony R. Valenzuela, Balakishore Yellampalle, Mark J. Schmitt, and Ki-Yong Kim. In-line holographic imaging and electron density extraction of ultrafast ionized air filaments. *J. Opt. Soc. Am. B*, 25(12):1988–1997, Dec 2008.
- [71] L. Romagnani, J. Fuchs, M. Borghesi, P. Antici, P. Audebert, F. Ceccherini, T. Cowan, T. Grismayer, S. Kar, A. Macchi, P. Mora, G. Pretzler, A. Schiavi, T. Toncian, and O. Willi. Dynamics of electric fields driving the laser acceleration of multi-mev protons. *Phys. Rev. Lett.*, 95:195001, Oct 2005.
- [72] Antoine Rousse, Kim Ta Phuoc, Rahul Shah, Alexander Pukhov, Eric Lefebvre, Victor Malka, Sergey Kiselev, Frédéric Burgy, Jean-Philippe Rousseau, Donald Umstadter, and Danièle Hulin. Production of a keV x-ray beam from synchrotron radiation in relativistic laser-plasma interaction. *Phys. Rev. Lett.*, 93:135005, Sep 2004.
- [73] H. P. Schlenvoigt, K. Haupt, A. Debus, F. Budde, O. Jackel, S. Pfotenhauer, H. Schwoerer, E. Rohwer, J. G. Gallacher, E. Brunetti, R. P.

- Shanks, S. M. Wiggins, and D. A. Jaroszynski. A compact synchrotron radiation source driven by a laser-plasma wakefield accelerator. *Nature Physics*, 4(2):130–133, December 2007.
- [74] M. Sheik-bahae, A. A. Said, and E. W. Van Stryland. High-sensitivity, single-beam n_2 measurements. *Opt. Lett.*, 14(17):955–957, Sep 1989.
- [75] C. W. Siders, S. P. Le Blanc, D. Fisher, T. Tajima, M. C. Downer, A. Babine, A. Stepanov, and A. Sergeev. Laser wakefield excitation and measurement by femtosecond longitudinal interferometry. *Phys. Rev. Lett.*, 76:3570–3573, May 1996.
- [76] Craig W. Siders, Jennifer L. W. Siders, Antoinette J. Taylor, Sang-Gyu Park, and Andrew M. Weiner. Efficient high-energy pulse-train generation using a 2 n-pulse michelson interferometer. *Appl. Opt.*, 37(22):5302–5305, Aug 1998.
- [77] D. R. Solli, C. Ropers, P. Koonath, and B. Jalali. Optical rogue waves. *Nature*, 450, 2007.
- [78] Donna Strickland and Gerard Mourou. Compression of amplified chirped optical pulses. *Optics Communications*, 56(3):219 – 221, 1985.
- [79] L. Sudrie, A. Couairon, M. Franco, B. Lamouroux, B. Prade, S. Tzortzakis, and A. Mysyrowicz. Femtosecond laser-induced damage and filamentary propagation in fused silica. *Phys. Rev. Lett.*, 89:186601, Oct 2002.

- [80] Quan Sun, Hongbing Jiang, Yi Liu, Zhaoxin Wu, Hong Yang, and Qihuang Gong. Measurement of the collision time of dense electronic plasma induced by a femtosecond laser in fused silica. *Opt. Lett.*, 30(3):320–322, Feb 2005.
- [81] K. Ta Phuoc, S. Corde, C. Thaury, V. Malka, A. Tafzi, J. P. Goddet, R. C. Shah, S. Sebban, and A. Rousse. All-optical Compton gamma-ray source. *Nature Photonics*, 6(5):308–311, April 2012.
- [82] T. Tajima and J. M. Dawson. Laser electron accelerator. *Phys. Rev. Lett.*, 43:267–270, Jul 1979.
- [83] E. Tokunaga, T. Kobayashi, and A. Terasaki. Frequency-domain interferometer for femtosecond time-resolved phase spectroscopy. *Opt. Lett.*, 17(16):1131–1133, Aug 1992.
- [84] E. Tokunaga, A. Terasaki, and T. Kobayashi. Femtosecond continuum interferometer for transient phase and transmission spectroscopy. *J. Opt. Soc. Am. B*, 13(3):496–513, Mar 1996.
- [85] Hai-En Tsai, Chih-Hao Pai, and M. C. Downer. Global optimization of quasi-monoenergetic electron beams from laser wakefield accelerators. *AIP Conference Proceedings*, 1507(1), 2012.
- [86] G. Tsaur, N.-H. Kang, Z.-H. Xie, S.-H. Chen, and J. Wang. Relativistic birefringence induced by a high-intensity laser field in a plasma. *Phys. Rev. A*, 83:033801, Mar 2011.

- [87] S. Tzortzakis, L. Sudrie, M. Franco, B. Prade, A. Mysyrowicz, A. Coua-iron, and L. Bergé. Self-guided propagation of ultrashort ir laser pulses in fused silica. *Phys. Rev. Lett.*, 87:213902, Nov 2001.
- [88] J. K. Wahlstrand, Y.-H. Cheng, Y.-H. Chen, and H. M. Milchberg. Optical nonlinearity in ar and n2 near the ionization threshold. *Phys. Rev. Lett.*, 107:103901, Aug 2011.
- [89] Xiaoming Wang, Rafal Zgadzaj, Neil Fazel, Zhengyan Li, S. A. Yi, Xi Zhang, Watson Henderson, Y. Y. Chang, R. Korzekwa, H. E. Tsai, C. H. Pai, H. Quevedo, G. Dyer, E. Gaul, M. Martinez, A. C. Bernstein, T. Borger, M. Spinks, M. Donovan, V. Khudik, G. Shvets, T. Ditmire, and M. C. Downer. Quasi-monoenergetic laser-plasma acceleration of electrons to 2 GeV. *Nature Communications*, 4, June 2013.
- [90] H. Weisen. The phase contrast method as an imaging diagnostic for plasma density fluctuations (invited). *Review of Scientific Instruments*, 59(8):1544–1549, Aug 1988.
- [91] S. Wilks, T. Katsouleas, J. M. Dawson, P. Chen, and J. J. Su. Beam Loading in Plasma Waves. *Plasma Science, IEEE Transactions on*, 15(2):210–217, 1987.
- [92] S. A. Yi, V. Khudik, S. Y. Kalmykov, and G. Shvets. Hamiltonian analysis of electron self-injection and acceleration into an evolving plasma bubble. *Plasma Physics and Controlled Fusion*, 53(1):014012, 2011.

- [93] F. Zernike. How I Discovered Phase Contrast. *Science*, 121:345–349,
March 1955.

Vita

Zhengyan Li was born in Changchun, Jilin Province, China in November 1985. He received the Bachelor of Science degree in Physics in July 2008 from the Peking University, Beijing, China. He was accepted and started graduate studies in the University of Texas at Austin in August, 2008.

Permanent address: 3450 Lake Austin Blvd., Apt D
Austin, Texas 78703

This dissertation was typeset with L^AT_EX[†] by the author.

[†]L^AT_EX is a document preparation system developed by Leslie Lamport as a special version of Donald Knuth's T_EX Program.